

PULSED ELECTRON DEPOSITION AND CHARACTERIZATION OF  
NANOCRYSTALLINE DIAMOND THIN FILMS

by

Omar Alshekhli

A thesis submitted in partial fulfillment

of the requirements for the degree of

Doctor of Philosophy (PhD) in Natural Resources Engineering

The School of Graduate Studies

Laurentian University

Sudbury, Ontario, Canada

© Omar Alshekhli, 2013

# THESIS DEFENCE COMMITTEE/COMITÉ DE SOUTENANCE DE THÈSE

## Laurentian Université/Université Laurentienne School of Graduate Studies/École des études supérieures

Title of Thesis  
Titre de la thèse PULSED ELECTRON DEPOSITION AND CHARACTERIZATION OF  
NANOCRYSTALLINE DIAMOND THIN FILMS

Name of Candidate  
Nom du candidat Alshekhli, Omar

Degree  
Diplôme Doctor of Philosophy

Department/Program  
Département/Programme Natural Resources Engineering

Date of Defence  
Date de la soutenance September 20, 2013

### APPROVED/APPROUVÉ

Thesis Examiners/Examineurs de thèse:

Dr. Redhouane Henda  
(Supervisor/Directeur de thèse)

Dr. Brahim Chebbi  
(Committee member/Membre du comité)

Dr. Nelson Belzile  
(Committee member/Membre du comité)

Dr. Meysar Zeinali  
(Committee member/Membre du comité)

Dr. Adrian H. Kitai  
(External Examiner/Examineur externe)

Dr. Jacques Farine  
(Internal Examiner/Examineur interne)

Approved for the School of Graduate Studies  
Approuvé pour l'École des études supérieures  
Dr. David Lesbarrères  
M. David Lesbarrères  
Director, School of Graduate Studies  
Directeur, École des études supérieures

### ACCESSIBILITY CLAUSE AND PERMISSION TO USE

I, **Omar Alshekhli**, hereby grant to Laurentian University and/or its agents the non-exclusive license to archive and make accessible my thesis, dissertation, or project report in whole or in part in all forms of media, now or for the duration of my copyright ownership. I retain all other ownership rights to the copyright of the thesis, dissertation or project report. I also reserve the right to use in future works (such as articles or books) all or part of this thesis, dissertation, or project report. I further agree that permission for copying of this thesis in any manner, in whole or in part, for scholarly purposes may be granted by the professor or professors who supervised my thesis work or, in their absence, by the Head of the Department in which my thesis work was done. It is understood that any copying or publication or use of this thesis or parts thereof for financial gain shall not be allowed without my written permission. It is also understood that this copy is being made available in this form by the authority of the copyright owner solely for the purpose of private study and research and may not be copied or reproduced except as permitted by the copyright laws without written authority from the copyright owner.

## Abstract

Diamond is widely known for its extraordinary properties, such as high hardness, thermal conductivity, electron mobility, energy bandgap and durability making it a very attractive material for many applications. Synthetic diamonds retain most of the attractive properties of natural diamond. Among the types of synthetic diamonds, nanocrystalline diamond (NCD) is being developed for electrical, tribological, optical, and biomedical applications.

In this research work, NCD films were grown by the pulsed electron beam ablation (PEBA) method at different process conditions such as accelerating voltage, pulse repetition rate, substrate material and temperature. PEBA is a relatively novel deposition technique, which has been developed to provide researchers with a new means of producing films of equal or better quality than more conventional methods such as Pulsed Laser Deposition, Sputtering, and Cathodic Vacuum Arc.

The deposition process parameters have been defined by estimating the temperature and pressure of the plasma particles upon impact with the substrates, and comparing the data with the carbon phase diagram. Film thickness was measured by visible reflectance spectroscopy technique and was in the range of 40 – 230 nm. The nature of chemical bonding, namely, the ratio ( $sp^3/sp^3+sp^2$ ) and nanocrystallinity percentage were estimated using visible Raman spectroscopy technique. The films prepared from the ablation of a highly ordered pyrolytic graphite (HOPG) target on different substrates consisted mainly of nanocrystalline diamond material in association with a diamond-like carbon phase. The micro-structural properties and surface morphology of the films were studied by atomic force microscopy (AFM) and scanning electron microscopy (SEM). The mechanical properties of the NCD films were evaluated by nano-indentation.

## Keywords

Nanocrystalline diamond, pulsed electron beam ablation, HOPG, thin film deposition, Raman analysis of carbon films,  $sp^3\%$ , diamond growth, diamond-like carbon films, nucleation.

## Acknowledgments

A Ph. D. thesis represents an important milestone in one's life, which is difficult to reach without the kind help and willing assistance of a number of individuals and groups, to whom I owe my gratitude and wish to gratefully acknowledge their contributions.

I wish to express my deepest sense of gratitude to my supervisor Prof. Redhouane Henda for his invaluable guidance, sustained interest, stimulating discussions, constant encouragement and unstinting commitment in ensuring this research project through to its completion. I am also indebted to him for a critical review of the thesis and manuscripts of technical papers and suggesting numerous valuable improvements. I am fortunate to have had the opportunity, privilege and pleasure of working under his supervision.

Raman measurements of the films were performed in Central Analytical Facility Lab. (CAF) at Willet Green Miller Centre (WGMC). It is the occasion to express my sincere thanks to Professor Andrew McDonald and Dr. William Zhe for their effort and assistance in making the above mentioned measurements, for their fruitful discussions and priceless suggestions.

I owe many thanks to Dr. Jeffrey Shepherd (Department of Chemistry) for helping me and allowing me to access AFM apparatus in his laboratory. Sincere thanks to Prof. Jamal Deen and Dr. Matiar Howlader (Dep. of Elec. and Comp. Eng., McMaster University) for their collaborating efforts on nanoindentation analysis.

Thanks are also given to the laboratory colleagues for priceless advice and moral support.

I wish to express my heartfelt thanks to my parents for raising me, supporting me, loving me and teaching me the value of education. It gives me immense pleasure to dedicate this thesis to them.

Finally, and most importantly I wish to thank my dear wife, Najwa and my son, Khattab. They made numerous sacrifices in reaching this milestone and were always around for providing a loving environment, help and assistance. The understanding and forbearance displayed by them have been exemplary.

# Table of Contents

Abstract.....	iii
Acknowledgement.....	iv
Table of Contents.....	v
List of Tables.....	vii
List of Figures.....	viii
List of Symbols.....	xvi
List of Abbreviation.....	xix
Chapter 1: Literature Review.....	1
1.1 Introduction.....	2
1.2 Deposition Techniques of Nanocrystalline Diamond.....	5
1.2.1 Plasma Enhanced Chemical Vapor Deposition (PECVD).....	5
1.2.2 Ion Beam Deposition (IBD).....	7
1.2.3 Cathodic Vacuum Arc (CVA) deposition.....	9
1.2.4 Pulsed Laser Deposition (PLD).....	12
1.3 Thesis Motivation.....	144
1.4 Research Objectives.....	155
Chapter 2: NCD Microstructure, Properties, and Applications.....	177
2.1 Carbon Material.....	188
2.1.1 Amorphous Carbon.....	19
2.1.2 Crystalline Carbon.....	21
2.2 Microstructure of Nanocrystalline Diamond.....	233
2.3 Properties and Applications of Nanocrystalline Diamond.....	255
Chapter 3: Experimental Procedure.....	31
3.1 Introduction.....	32
3.2 Pulsed Electron Deposition.....	32
3.2.1 The Physics of Pulsed Electron Ablation.....	32
3.2.2 Substrates and Equipment Preparation and Cleaning.....	37
3.2.3 Process Conditions.....	39

3.3	Heat Treatment (Pre-deposition Annealing) .....	433
3.4	Characterization Techniques .....	455
3.4.1	Visible Reflectance Spectroscopy.....	45
3.4.2	Raman Spectroscopy.....	47
3.4.2.1	Theory of Raman Spectroscopy.....	47
3.4.2.2	Raman Instrumentation Setup.....	48
3.4.2.3	Raman Characterization of NCD films.....	50
3.4.3	Scanning Electron Microscope (SEM).....	52
3.4.4	Atomic Force Microscopy (AFM).....	54
3.4.5	X-Ray Diffraction (XRD) .....	56
3.4.6	Nano-Indentation.....	59
Chapter 4: Calculation of Temperature and Pressure of Carbon Ions on Impact .....		62
4.1	Introduction .....	63
4.2	Carbon Phase Diagram.....	64
4.3	Strikovski's Model .....	655
4.4	Shock Wave Model .....	71
4.4.1	Plasma Expansion in Vacuum.....	72
4.4.2	Plasma Expansion in Ambient Gas.....	74
4.5	Phase Estimation of Deposited Films.....	755
4.6	Discussion of the Results .....	788
Chapter 5: Experimental Results and Discussion.....		799
5.1	Introduction .....	80
5.2	Results of First Series.....	80
5.2.1	Film Thickness.....	80
5.2.2	Crystal Size, $sp^3$ Content and Nanocrystallinity.....	83
5.2.3	Film Morphology.....	88
5.2.4	Film Hardness.....	91
5.3	Discussion of the Results of the First Series .....	92
5.3.1	Effect of Substrate Material.....	93
5.3.2	Effect of Substrate Temperature.....	93
5.3.3	Effect of Pulse Number.....	94
5.4	Results of Second Series .....	95
5.4.1	Film Thickness.....	95

5.4.2	Crystal Size, $sp^3$ Content and Nanocrystallinity.....	99
5.4.3	XRD Results.....	105
5.4.4	Film Morphology.....	106
5.4.5	Film Hardness .....	110
5.5	Discussion of the Results of the Second Series.....	11010
5.5.1	Effect of Accelerating Voltage.....	111
5.5.2	Effect of Pulse Repetition Rate.....	112
5.6	Results of Third Series .....	11313
5.6.1	Film Thickness.....	113
5.6.2	Crystal Size, $sp^3$ Content and Nanocrystallinity.....	116
5.6.3	Film Morphology.....	119
5.6.4	Film Hardness .....	123
5.7	Discussion of the Results of the Third Series .....	12424
Chapter 6: Conclusion and Future Work .....		1277
6.1	Conclusion.....	128
6.2	Future Work.....	130
References.....		131

## List of Tables

Table 2.1: Some properties of NCD at room temperature.....	27
Table 3.1: The specifications of substrates used in all experiments.....	41
Table 3.2: Process parameters of all series.....	42
Table 4.1: Temperature and pressure of ions on impact at different accelerating voltage.....	68
Table 4.2: Temperature and pressure of ions on impact at different accelerating voltage estimated using the shockwave model – vacuum condition and at 5 cm substrate-target distance.....	74
Table 4.3: Pressure of ions on impact estimated using the shockwave model at different accelerating voltage values – both background gas and vacuum conditions are reported for a 5 cm substrate-target distance.....	76
Table 5.1: Results of Raman spectra deconvolution of all NCD films resulting from the first series.....	84
Table 5.2: Substrate, combined, and film hardness for NCD films resulting from the first series - 14 kV, 5500 pulses, and RT.....	92
Table 5.3 A: Results of Raman spectra deconvolution of all NCD films resulting from the second series at 8 Hz.....	99
Table 5.3 B: Results of Raman spectra deconvolution of all NCD films resulting from the second series at 5 Hz.....	100
Table 5.4: Substrate, combined, and film hardness for NCD films resulting from the second series.....	110
Table 5.5: Roughness of bare substrates annealed at 900 °C and 1100 °C .....	115
Table 5.6: Results of Raman spectra deconvolution of all NCD films resulting from the third series.....	116
Table 5.7: Substrate, combined, and film hardness for NCD films on substrates annealed at 900 °C resulting from the third series.....	124
Table 5.8: Substrate, combined, and film hardness for NCD films on substrates annealed at 1100 °C resulting from the third serie.....	124

## List of Figures

Figure 1.1: Types of different structure nano-diamond films.....	4
Figure 1.2: Schematic diagram of plasma enhanced CVD setup.....	7
Figure 1.3: Schematic illustration of ion beam deposition system.....	8
Figure 1.4: Basic coating setup of cathodic arc plasma source.....	11
Figure 1.5: Schematic of typical PLD system used for the deposition of NCD films.....	13
Figure 2.1: The $sp^3$ , $sp^2$ , $sp^1$ hybridized bonding.....	19
Figure 2.2: Schematic density of states of amorphous carbon.....	20
Figure 2.3: Graphite is on the left. Diamond is on the right.....	21
Figure 2.4: Chemical structure of graphite.....	22
Figure 2.5: Chemical structure of diamond.....	23
Figure 2.6: Structure of NCD material.....	24
Figure 2.7: SEM images of MCD and NCD films.....	25
Figure 3.1: Simplified schematics of a PEBA system.....	33
Figure 3.2: Neocera PEBA system.....	34
Figure 3.3: Angular distribution of ablated material.....	37
Figure 3.4: Ultrasonic cleaning bath.....	38
Figure 3.5: Four different bare substrates.....	39
Figure 3.6: Three various substrates glued on the substrate holder.....	39
Figure 3.7: Highly Oriented Pyrolytic Graphite (HOPG) Target.....	40

Figure 3.8 Four different substrates coated with NCD films.....	43
Figure 3.9: HST Carbolite furnace.....	44
Figure 3.10: Schematic diagram of heat treatment system.....	45
Figure 3.11: Visible spectral reflectance system.....	46
Figure 3.12: The Jablonski diagram compares Raman, Rayleigh, and Fluorescence scattering...48	
Figure 3.13: Raman spectrometer instrument scheme.....	49
Figure 3.14: Raman spectrometer.....	50
Figure 3.15: Visible Raman spectrum of a typical nanodiamond sample.....	51
Figure 3.16: Scanning electron microscope scheme.....	53
Figure 3.17: Schematic of AFM instrument.....	55
Figure 3.18: Bruker multimode AFM IIID.....	56
Figure 3.19: Bragg's law and diffracted X-rays.....	58
Figure 3.20: schematic diagram of a nanoindentation system.....	59
Figure 3.21: Load P versus displacement h curve.....	60
Figure 4.1: Carbon phase diagram. Stability regions of crystalline diamond and graphite in the pressure-temperature diagram.....	66
Figure 4.2: Estimated current/voltage (I/U) as a function of the electron energy.....	68
Figure 4.3: Diagram showing the plume at the end of the pulse when the dimensions are $X_o$ , $Y_o$ , and $Z_o$ , and after a time t when the dimensions are $X(t)$ , $Y(t)$ , $Z(t)$ .....	72
Figure 4.4: Calculated results of pressure and temperature of ions on impact, as per target-substrate distance of 5 cm.....	76

Figure 4.5: Calculated results of pressure and temperature of ions on impact, as per target-substrate distance of 7 cm.....	77
Figure 5.1: Visible spectroscopic reflectance of NCD film on Si(100) resulting from the first series at 5 Hz, 14 kV, and RT.....	81
Figure 5.2: Visible spectroscopic reflectance of NCD film on Si(111) resulting from the first series at 3500 pulses, 14 kV, and RT.....	81
Figure 5.3: Visible spectroscopic reflectance of NCD film on Si(100) resulting from the first series at 3500 pulses, 14 kV, and 150 °C.....	82
Figure 5.4: Visible spectroscopic reflectance of NCD film on Si(100) resulting from the first series at 5500 pulses, 14 kV, and RT.....	82
Figure 5.5: Thickness of NCD films resulting from the first series on various substrates.....	83
Figure 5.6: Raman spectra (and their deconvolution) of NCD films on various substrates resulting from the first series at 3500 pulses, 14 kV, and RT.....	85
Figure 5.7: Raman spectra (and their deconvolution) of NCD films on various substrates resulting from the first series at 3500 pulses, 14 kV, and RT.....	85
Figure 5.8: Raman spectra (and their deconvolution) of NCD films on various substrates resulting from the first series at 3500 pulses, 14 kV, and 150 °C.....	86
Figure 5.9: Raman spectra (and their deconvolution) of NCD films on various substrates resulting from the first series at 5500 pulses, 14 kV, and RT.....	86
Figure 5.10: sp <sup>3</sup> percentage in films resulting from the first series .....	87
Figure 5.11: Nanocrystallinity percentage in films resulting from the first series.....	87
Figure 5.12: Crystal size in films resulting from the first series.....	88
Figure 5.13: AFM three-dimensional view of film morphology of NCD films resulting from the first series – 14 kV, 3500 pulses, and RT. Four different substrates are shown.....	88

Figure 5.14: AFM three-dimensional view of film morphology of NCD films resulting from the first series – 14 kV, 3500 pulses, and RT. Three different substrates are shown.....	89
Figure 5.15: AFM three-dimensional view of film morphology of NCD films resulting from the first series – 14 kV, 3500 pulses, and 150 °C. Four different substrates are shown.....	89
Figure 5.16: AFM three-dimensional view of film morphology of NCD films resulting from the first series – 14 kV, 5500 pulses, and RT. Four different substrates are shown.....	90
Figure 5.17: SEM images of films on Si(100) resulting from the first series at different operating conditions.....	91
Figure 5.18: Load and unload displacement curves obtained from nanoindentation of NCD films on Pyrex resulting from series 1 at 5500 pulses and RT.....	92
Figure 5.19: Visible spectroscopic reflectance of NCD film on Si(100) resulting from the second series - 14.5 kV and 8 Hz.....	95
Figure 5.20: Visible spectroscopic reflectance of NCD film on Si(100) resulting from the second series - 16 kV and 8 Hz. ....	96
Figure 5.21: Visible spectroscopic reflectance of NCD film on Si(100) resulting from the second series - 13 kV and 8 Hz. ....	96
Figure 5.22: Visible spectroscopic reflectance of NCD film on Si(100) resulting from the second series - 14.5 kV and 5 Hz. ....	97
Figure 5.23: Visible spectroscopic reflectance of NCD film on Si(100) resulting from the second series - 16 kV and 5 Hz. ....	97
Figure 5.24: Visible spectroscopic reflectance of NCD film on Si(100) resulting from the second series - 13 kV and 5 Hz. ....	98
Figure 5.25: Film thickness of NCD films resulting from the second series.....	98
Figure 5.26: Raman spectra (and their deconvolution) of NCD films on various substrates resulting from the second series - 14.5 kV and 8 Hz.....	100

Figure 5.27: Raman spectra (and their deconvolution) of NCD films on various substrates resulting from the second series - 16 kV and 8 Hz.....	101
Figure 5.28: Raman spectra (and their deconvolution) of NCD films on various substrates resulting from the second series - 13 kV and 8 Hz.....	101
Figure 5.29: Raman spectra (and their deconvolution) of NCD films on various substrates resulting from the second series - 14.5 kV and 5 Hz.....	102
Figure 5.30: Raman spectra (and their deconvolution) of NCD films on various substrates resulting from the second series - 16 kV and 5 Hz.....	102
Figure 5.31: Raman spectra (and their deconvolution) of NCD films on various substrates resulting from the second series - 13 kV and 5 Hz.....	103
Figure 5.32: sp <sup>3</sup> percentage in films resulting from the second series.....	103
Figure 5.33: Nanocrystallinity percentage in films resulting from the second series.....	104
Figure 5.34: Crystal size in films resulting from the second series.....	104
Figure 5.35: PXRD patterns of NCD on Pyrex resulting from the second series – 8 Hz & 14.5 kV.....	105
Figure 5.36: AFM three-dimensional view of film morphology of NCD films resulting from the second series – 8 Hz & 14.5 kV. Four different substrates are shown.....	106
Figure 5.37: AFM three-dimensional view of film morphology of NCD films resulting from the second series – 8 Hz & 16 kV. Four different substrates are shown.....	106
Figure 5.38: AFM three-dimensional view of film morphology of NCD films resulting from the second series – 8 Hz & 13 kV. Four different substrates are shown.....	107
Figure 5.39: AFM three-dimensional view of film morphology of NCD films resulting from the second series – 5 Hz & 14.5 kV. Four different substrates are shown.....	107
Figure 5.40: AFM three-dimensional view of film morphology of NCD films resulting from the second series – 5 Hz & 16 kV. Four different substrates are shown.....	108

Figure 5.41: AFM three-dimensional view of film morphology of NCD films resulting from the second series – 5 Hz & 13 kV. Four different substrates are shown.....	108
Figure 5.42: SEM images of Si(100) films resulting from the second series at 5 Hz.....	109
Figure 5.43: Visible spectroscopic reflectance of NCD film on Si(100) (annealed at 900 °C) resulting from the third series.....	114
Figure 5.44: Visible spectroscopic reflectance of NCD film on Si(100) (annealed at 1100 °C) resulting from the third series.....	114
Figure 5.45: Film thickness of NCD films resulting from the third series.....	115
Figures 5.46: Raman spectra (and their deconvolution) of NCD films on various substrates (annealed at 900 °C) resulting from third series.....	117
Figures 5.47: Raman spectra (and their deconvolution) of NCD films on various substrates (annealed at 1100 °C) resulting from third series.....	117
Figure 5.48: sp <sup>3</sup> percentage in films resulting from the third series.....	118
Figure 5.49: Nanocrystallinity percentage in films resulting from the third series.....	118
Figure 5.50: Crystal size in films resulting from the third series.....	119
Figure 5.51: AFM two-dimensional view of surface morphology of three different substrates.....	120
Figure 5.52: AFM two-dimensional view of surface morphology of three different substrates (annealed at 900 °C).....	120
Figure 5.53: AFM two-dimensional view of surface morphology of three different substrates (annealed at 1100 °C).....	121
Figure 5.54: AFM three-dimensional view of film morphology of NCD films on substrates annealed at 900 °C resulting from the third series. Three different substrates are shown.....	121

Figure 5.55: AFM three-dimensional view of film morphology of NCD films on substrates annealed at 1100 °C resulting from the third series. Three different substrates are shown.....122

Figure 5.56: SEM images of NCD films on substrates annealed at 900 °C resulting from the third series. Three different substrates are shown.....122

Figure 5.57: SEM images of NCD films on substrates annealed at 1100 °C resulting from the third series. Three different substrates are shown.....123

Figure 5.58: Roughness effect on film thickness: (a) heat treated substrate and (b) non-heat treated substrate.....125

## List of Symbols

$\alpha$	Thermodynamic property
$\beta$	Correction coefficient.
$\Gamma(z)$	Gamma-function
$\gamma$	Thermodynamic property
$\varepsilon$	Thermal energy per unit mass of ablated material (J/kg)
$\xi_0$ and $\eta_0$	Dimensionless quantities
$\lambda$	Represents the wavelength of X-ray (nm)
$\mu$	Atomic mass ratio between the target material and the gas
$\theta$	Signifies the X-ray scattering angle (degree)
$\rho$	The target density ( $\text{g/cm}^3$ )
$\nu$	Poisson's ratio
$\varphi$	The angular distribution of the relative mass flow of the ablated material (degree)
$A_c$	The contact area of the tip on the surface of the material ( $\text{m}^2$ )
$a_Y$	The ratio of the yield stress of substrate to that of the film
$a_E$	The ratio of the elastic modulus of substrate to that of the coating or film
$C$	The specific heat capacity of the target (J/g.K)
$D$	The absorption length (electron range) ( $\mu\text{m}$ )
$D_T$	The thermal diffusion length ( $\mu\text{m}$ )
$d$	Target-substrate distance (cm)
$E$	Elastic modulus (MPa)
$E^*$	The composite elastic's modulus (MPa)
$E_p$	Thermal energy of the initial plume (J)
$H$	Hardness (MPa)
$H_{\text{com}}$	Combined hardness (MPa)
$H_f$	Film hardness (MPa)
$H_s$	Substrate hardness (MPa)
$h$	Deposition rate per pulse (nm/pulse)
$h_c$	The contact depth in Nanoindentation (nm)
$I$	Total beam current (A)

$I_2(\gamma)$	Function of the adiabatic index (dimensionless)
$I_G$	Intensity of G band peak within the range 1536-1565 $\text{cm}^{-1}$
$I_{1150}$	Intensity of NCD band peak at 1150 $\text{cm}^{-1}$
$I_{1332}$	Intensity of diamond band peak at 1332 $\text{cm}^{-1}$
$k$	Boltzmann constant (J/K)
$L_o$	Plasma propagation range (cm)
$M$	Carbon atomic mass (kg)
$M_p$	Mass of the initial plume (kg)
$N_o$	Ablated material amount (atoms/ $\text{cm}^3$ )
$n_g$	Background gas concentration (atoms/ $\text{cm}^3$ )
$n_L$	Density of solid material ( $\text{g}/\text{cm}^3$ )
$P$	Pressure (Pa)
$P_g$	Pressure of background gas (Pa)
$P_{\max}$	The maximum applied load (Pa)
$P_o$	pressure of background gas in the deposition chamber (Pa)
$p_o$	Ratio of pressure of bombarding ions on impact in vacuum to the pressure of bombarding ions on impact in a background gas
$Q$	The minimal absorbed power density ( $\text{W}/\text{cm}^2$ )
$R$	Molar gas constant ( $\text{m}^2 \text{kg s}^{-2} \text{K}^{-1} \text{mol}^{-1}$ )
$S$	The beam cross section on the target surface ( $\text{cm}^2$ )
$T$	Temperature (K)
$\Delta T$	The rate of surface temperature rise (K)
$t$	Film thickness (nm)
$U$	Pulsed electron beam source (PEBS) accelerating voltage (kV)
$\Delta V$	Molar difference in volume between diamond and the activated complex ( $\text{m}^3$ )
$V$	Velocity of ions at any height (m/s)
$V_o$	Initial velocity of the atoms (m/s)
$V_T$	Characteristic thermal velocity (m/s)
$X, Y, \text{ and } Z$	Full dimensions of the expanding plasma (cm)
$x, y, \text{ and } z$	The coordinates of any ion or particle within the full range plasma (cm)

## List of Abbreviations

aC	Amorphous Carbon
AFM	Atomic force Microscopy
CVD	Chemical Vapor Deposition
DLC	Diamond Like Carbon
EELS	Electron Energy Loss Spectroscopy
FCVA	Filtered Cathodic Vacuum Arc
GAXRD	Grazing Incidence X-Ray Diffraction
HFCVD	Hot Filament Chemical Vapor Deposition
HOPG	Highly Ordered Pyrolytic Graphite
IBD	Ion Beam Deposition
MCD	Microcrystalline Diamond
MPCVD	Microwave Plasma Chemical Vapor Deposition
NCD	Nanocrystalline Diamond
PECVD	Plasma Enhanced Chemical Vapor Deposition
PLD	Pulsed Laser Deposition
PEBA	Pulsed Electron Beam Ablation
SEM	Scanning Electron Microscopy
UNCD	Ultra Nanocrystalline Diamond
XRD	X-Ray Diffraction

# **Chapter 1: Literature Review**

## 1.1 Introduction

Film deposition of technologically important materials aims at providing better functionality and eventually applications to a variety of substrates. Such property enhancements may appear in the form of longer lifetime or higher reliability. The purpose of these modifications is to introduce better properties such as wear resistance and lubrication to the surface while at the same time retaining the strength, toughness and other bulk properties of the material. It is essential that films maintain a high degree of surface adhesion. The films must be virtually nonreactive in the surrounding environment and resistant to mechanical damage owing to exposure of the bare substrate to harsh process environment. A number of thin film deposition techniques were developed in the last century, in parallel with the improvement of electronics, vacuum- and measurement-technologies. Lately, the fast development of these techniques has initiated an exponentially growing research activity focusing on deposition of thin films for a largely diversified field of technologically important applications.

Carbon has proven to be one of the most fascinating elements. Natural carbon is tetravalent as the result of four electrons revolving in exterior shell (Gopalakrishnan and Subramanyam, 2002). Carbon has numerous allotropes and comes in different forms such as diamond, graphite, fullerene, carbon nanotubes and amorphous carbon, in addition to other variations such carbon black, carbon fibers, porous carbon, glassy carbon, diamond-like carbon, and nanocrystalline diamond (NCD) (Gopalakrishnan and Subramanyam, 2002; Lifshitz, 1999).

Diamond has exceptional optical and electrical properties. Its optical transparency is significant in a very large optical spectral range extending from the UV to far infrared, and is associated with its large band gap, i.e.,  $E_g \approx 5.5$  eV (Gopalakrishnan and Subramanyam, 2002; Nazare and Neves, 2001). The specific  $sp^3$  hybridization of carbon in the diamond form implies that each carbon atom is bonded tetrahedrally to neighboring carbon atoms at an angle of  $109.50^\circ$ . Diamond is a highly dense form of carbon at room temperature-atmospheric pressure. Due to the covalent nature of C-C bonds, diamond is quite chemically inert, viz, resistant to chemicals and concentrated acids, and any strong oxidizing agents. Nano-structured diamond or thin films of diamond can be produced at relatively high temperature and high pressure using microwave chemical vapor deposition

process (MPCVD) (Nazare and Neves, 2001). Therefore, CVD methods are not recommended from an economic point of view.

The  $sp^2$  hybridization is found in graphite, whereby, each atom is bonded trigonally to each other at an angle of  $120^\circ$ . Graphite is a highly anisotropic solid (Gopalakrishnan and Subramanyam, 2002). The physical properties of graphite show that the material is stiffer along the plane (where the hexagonal rings lie), which are due to the  $\sigma$  bonds. Along the perpendicular direction to the plane, graphite is weakly bonded as the results van der Waals forces (Robertson, 2002). The type of carbon, which is the main focus of this research work is the so called NCD, an artificial diamond. Basically NCD consists of two phases: the first phase is made up of diamond crystallites (diamond grains) imbedded in a second phase, intergrain phase (Williams, 2011). NCD has both  $sp^3$  and  $sp^2$  coordinations.

The term nanocrystalline diamond was initially given to thin film of diamond of poor quality. Recently, NCD has developed into a sophisticated material with a wide variety of applications and terminology. Three different structures of nano-diamond material are shown in Fig. 1.1, viz., diamond-like carbon, ultra nano-crystalline diamond, and nanocrystalline diamond. Diamond-like carbon is described as an amorphous carbon containing a relatively high degree of  $sp^3$  bonding (Erdemir & Donnet, 2006) and is one amongst the synthetic forms of carbon, which has both  $sp^3$  and  $sp^2$  coordinations. Ultra nanocrystalline diamond (UNCD) resembles NCD in structure remarkably. However, grain size in UNCD is significantly smaller compared to grain size in NCD. NCD is very sensitive to the various environmental conditions in the coating process, which implies both difficulty and flexibility in controlling its properties (Williams, 2011).

The unique physicochemical properties of NCD include the microstructure, high hardness, high wear resistance, chemical inertness, tunable electrical resistance, and optical transparency, depending on the deposition conditions. Changes in the size of the nanocrystallites, film thickness, or phase purity, can dramatically alter NCD film properties (Gruen, 1999). Due to its enhanced mechanical and infrared optical characteristics, it is a material of choice in the mining sector (drilling machines) and micro-electronic industry such as a protective layer of computer hard drive magnetic discs (Williams et al., 2008). In addition, its bio-compatibility makes it a useful bio-coating in hip joints, heart valves, and stents (Chen et al., 2011).

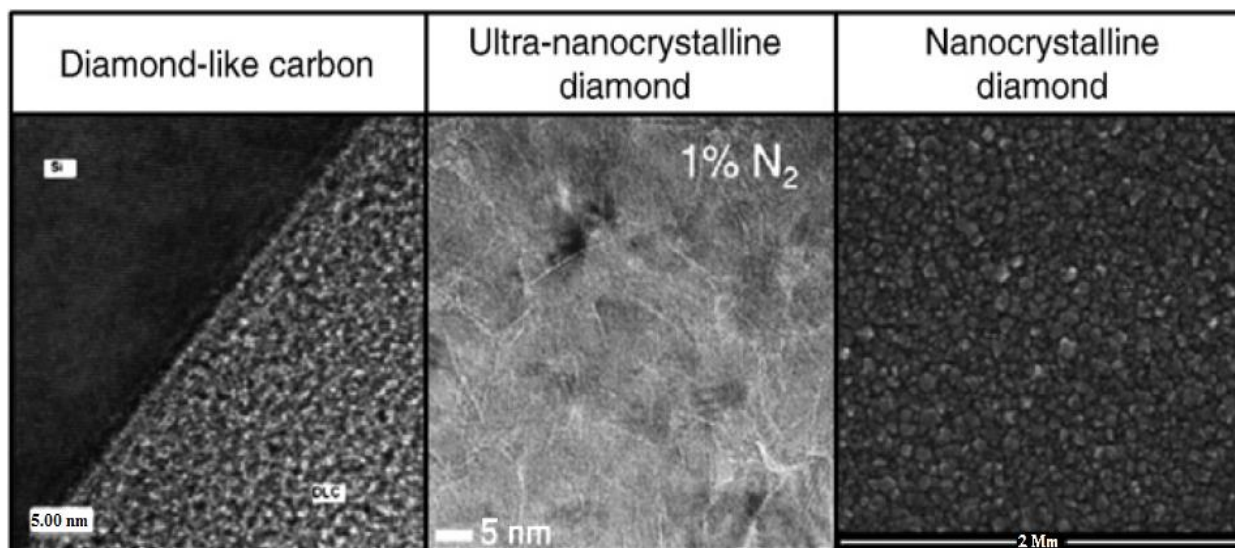


**Figure 1.1: Types of different structure nano-diamond films (Williams, 2011).**

In semiconductor applications, NCD can be doped with other elements without changing some of its attractive properties such as hardness and friction coefficient, opening up opportunities in device design using both its p- and n-type forms (Haenni et al., 2004). Such a rich combination of so many outstanding properties in one material is technologically appealing.

The cost of producing flat large single crystals of diamond is still quite high. For many applications, single crystal diamond is not needed and polycrystalline diamond is adequate. However, in some cases a polycrystalline diamond surface is too rough (because of grain size) and nano-crystalline diamond with its greater surface smoothness is preferable. The advantages of NCD are its relatively high growth rate, reasonable mechanical properties, and much lower production cost compared to diamond itself. Its disadvantages lie in its intrinsic stress and lack of complete semiconducting properties (Williams, 2008).

In the present work, the preparation of NCD thin films has been attempted using the pulsed electron beam ablation (PEBA) technique. To the best of my knowledge, no study on the successful preparation of NCD has been carried out so far using PEBA channel spark configuration, and hence the principal motivation for this work. In the next section, summaries of the various attempts made by other researchers to prepare NCD films using different techniques are given.

## 1.2 Deposition Techniques of Nanocrystalline Diamond

Nowadays, various synthesis techniques are used to grow high quality NCD thin films. Two different growth mechanisms are in existence for growing NCD. One is the equilibrium growth at high pressure and the other being the metastable growth at vacuum pressures (Gruen, 1999; May et al., 2006; Ravi et al., 1996; Hongyan et al., 2000).

NCD synthesis and deposition methods can be divided into two groups: Chemical vapor deposition (CVD) methods involving carbon bearing compounds, and physical vapor deposition (PVD) methods based on energetic evaporation, sputtering, or ablation of a carbonaceous target. The first group includes ion beam assisted CVD, plasma enhanced CVD, plasma deposition using an rf glow discharge, microwave discharge, and low pressure CVD. The second group includes Cathodic Vacuum Arc deposition, sputter deposition, ion beam deposition, pulsed laser ablation (PLD), and pulsed electron beam ablation (PEBA) (Philip et al., 2003; Lee et al., 1995; Aoki et al., 2005; Xie et al., 2008; Yoshitake et al., 2004). This section will briefly describe several techniques that have been widely employed to synthesize and deposit NCD in thin film form.

### 1.2.1 Plasma Enhanced Chemical Vapor Deposition (PECVD)

One of the most popular methods to deposit NCD is plasma enhanced chemical vapor deposition (PECVD). To deposit NCD films using PECVD mixtures of hydrocarbons, usually methane, and hydrogen are used. Using methane ( $\text{CH}_4$ ) in plasma enhanced CVD, various dissociation processes and abstracted reactions can take place, which may form  $\text{CH}_2$  or  $\text{CH}_3$  in their radical form as well as ionized forms upon electron impact in second order reactions. Typically, the interactions of the radicals at the substrate surface enable growth of NCD thin films (Williams et al., 2008; Winfrey, 2007). The gas used in PECVD has a significant effect on the resulting NCD properties.

During the PECVD process of NCD, hydrogen would perform a number of important functions. Hydrogen may etch the graphitic phase ( $\text{sp}^2$ -bonded carbon atoms) faster than the diamond-like phase ( $\text{sp}^3$ -bonded carbon atoms). Hydrogen would help in stabilising the surface, while growth takes place, by terminating the “dangling bonds” on the diamond surface. Moreover, hydrogen atoms could prevent polymers build-up due to their ability of reacting with large gas phase hydrocarbon fragments and splitting them into small pieces (May et al., 2006; Okada, 2007).

PECVD reactor essentially consists of two metal electrodes of different areas separated by a small distance, as shown in Fig. 1.2. The gas pressure in the reactor can be of the order of one atmosphere or lower. The radio frequency rf power is usually capacitively coupled to the smaller electrode on which the substrate is mounted, and the other electrode (often including the reactor walls) is earthed. The rf power produces a plasma between the electrodes. The higher mobility of electrons compared to ions in the plasma creates a sheath next to the electrodes with an excess of ions (Winfrey, 2007). The smaller electrode with smaller capacitance acquires the larger bias voltage and becomes negatively charged with respect to the larger electrode. The purpose for a negative substrate bias voltage is to let carbon ions bombard the growing film. The ions can lose energy by collisions when being accelerated across the sheath. It is desirable to deposit under low pressure to minimize these collisions and maintain a narrow ion energy distribution (Lieberman and Lichtenberg, 1994).

In 2003, Philip and coworkers reported on the deposition of nanocrystalline diamond films on silicon substrates by chemical vapor deposition in a microwave plasma reactor with purified methane and hydrogen as the reactants. The substrate pretreatment by the deposition of a thin H-terminated a-C film followed by the seeding of nanodiamond powder increased the nucleation density on the Si substrate to over  $10^{12}/\text{cm}^2$ . The density of the resulting films was close to the density of single crystal diamond or polycrystalline diamond, whereas the Young modulus varied strongly with the nucleation density between  $\sim 500$  and  $1100$  GPa (Philip et al., 2003).

Three years later, May and coworkers (2006) attempted to deposit nanocrystalline diamond via hot filament (HF) chemical vapour deposition reactor using a mixture of gases, namely, argon, methane, and hydrogen. They reported that NCD growth is confined to a limited composition window at the boundary between the microcrystalline diamond (MCD) growth region and the “no growth” region, and the NCD growth rates are very small ( $<0.1 \mu\text{m}/\text{h}$ ). They have postulated this confinement to occur due to a reduction in the concentration of H atoms along with a decrease in the  $[\text{H}]/[\text{CH}_3]$  ratio at the growing substrate surface (May et al., 2006).

NCD deposition using PECVD generally yields good deposition rates, very uniform coatings, and it could be used for large-scale production. However, a relatively high temperature ( $600^\circ\text{C}$ ) for deposition is required, which makes it an energy consuming method.

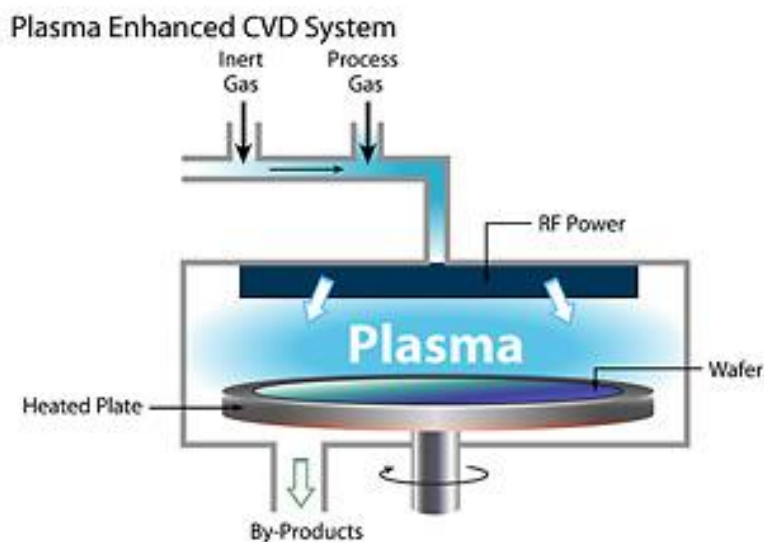


**Figure 1.2: Schematic diagram of plasma enhanced CVD setup (Dow Corning Corporation, 2012)**

Moreover, the cost of PECVD equipment is significantly high, and the deposition process would generate some toxic byproducts (Okada, 2007; Lieberman and Lichtenberg, 1994; Sharda et al., 2001).

### 1.2.2 Ion Beam Deposition (IBD)

Most commonly, ion beams for diamond or amorphous carbon deposition are generated by extracting positive ions from a hydrocarbon source (target). The ion energy of the beam is controlled by adjustment of the plasma potential with respect to ground (the “beam voltage”). The ion beam is space-charge neutralized by addition of electrons downstream of the source to eliminate any potential for charge build-up on insulating substrates. The ion beam is directed onto the substrate to form an NCD coating at a rate that is proportional to the ion-beam current density. The driving force behind the use of ion beams lies in the better control of ion beams than other plasma sources. For example, an ion beam can be produced with a narrow energy distribution and specified direction. Important parameters such as beam energy and ion current density can be controlled almost independently over a wide range of process conditions (Wei and Narayan, 2000; Aisenberg and Chabot, 1973).

Target striking ions are produced in the discharge chamber by subjecting a gas (usually argon) to an rf field. The gas is fed into a quartz or alumina chamber with an rf powered coil antenna around it. The rf field excites free electrons until they have acquired enough energy to break gas atoms into ions and electrons. The gas is thus ionized and a plasma is established. These ions will erode the hydrocarbon source (the target) by sputtering, generating carbon ions that will eventually condense on the substrate to form NCD films (Pochon & Pearson, 2009; Sun et al., 1999), as shown in Fig. 1.3.

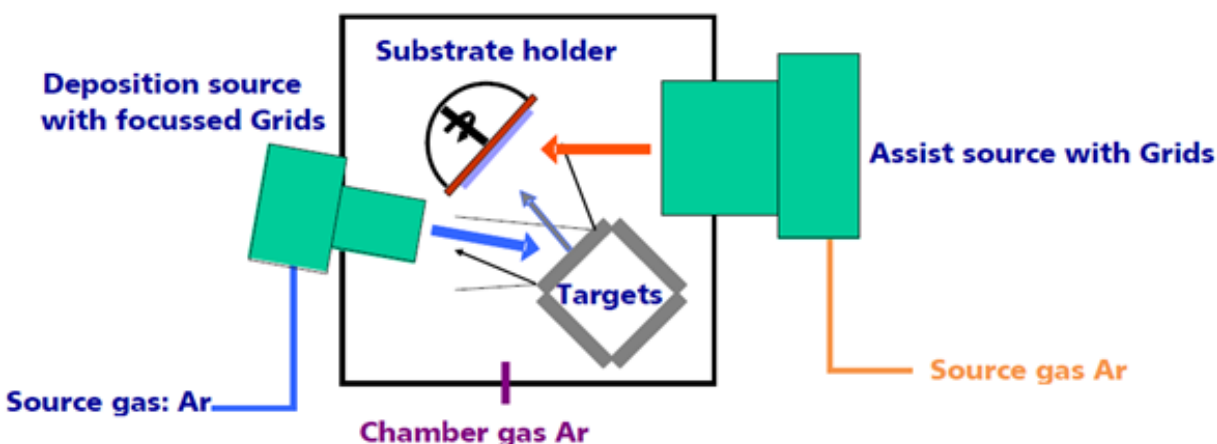


**Figure 1.3: Schematic illustration of ion beam deposition system (Pochon & Pearson, 2009)**

The impacting ions in this technique are used to supply both the deposition atoms and the energy required for improved film formation. Very smooth deposited films are usually produced this way (Wei and Narayan, 2000; Pochon & Pearson, 2009).

One of the earliest trials to deposit nanocrystalline diamond using ion beam deposition was done in 1985 by Kitabatake and Wasa. A graphite disk target is bombarded using electron-bombardment ion source. The authors have managed to grow diamond particles of 0.1-1  $\mu\text{m}$  in diameter with a well defined morphology at room temperature on non-diamond substrates (Kitabatake and Wasa, 1985).

A decade later, in 1995, Lee and coworkers managed to deposit nanodiamond coatings on nickel and copper substrates. Nanodiamond growth resulted from the continuous incorporation of the implanted high energy carbon ions and cascade collision-induced diffusion of the host atoms toward the substrate. They have reported that the structure of the grown layer is, however, of a

nanodiamond structure with a density slightly lower than that of diamond, and a very thin surface graphitization layer. A single crystal growth using the ion beam approach seems unlikely due to the huge number of defects during the deposition process (Lee et al., 1995).

In 1999, Sun and coworkers managed to grow nanocrystalline diamond on a mirror-polished Si(100) substrate by means of direct ion beam deposition. Hydrocarbon and hydrogen ions, generated in a Kaufman ion source, were used to bombard the substrates. They have reported the existence of nanocrystalline diamond particles of random orientation in a matrix of deposited films on the Si(100) substrate. The size of the nanocrystalline diamond particles varied in the range of 5–30 nm (Sun et al., 1999).

While the IBD combines both the advantages of physical vapor deposition and chemical vapor deposition techniques, the synthesis of hard films is very difficult at relatively high power/high pressures. A practical aspect of ion beam method to deposit NCD is that it occurs at low temperatures (close to room temperature). However, gas pressure inside the chamber has to be optimized to minimize the rate of generating large flux of nonionized particles, which may result in a low flux ratio of ions to neutrals. Poor ratio of ions/neutrals would cause a low deposition rate (1 micrometer/hr or less), and not produce good quality NCD films in terms of high  $sp^3/sp^2$ . The low ratio of ions/neutrals causes less chances of ion bombardment, hence less  $sp^3$  bonding is present in the deposited films (Wei and Narayan, 2000; Lee et al., 1995; Aisenberg and Chabot, 1973).

### 1.2.3 Cathodic Vacuum Arc (CVA) Deposition

Cathodic Vacuum Arc (CVA) deposition is a plasma-based technology for the fabrication of films. The process can be carried out either under high vacuum or in a low pressure gaseous environment. The method provides a versatile and powerful plasma for the synthesis of novel and technically important surfaces (Anders, 2008).

The arc evaporation process begins with the striking of a high current, low voltage arc on the surface of a cathode (known as the target), which gives rise to a small (usually a few micrometers wide), highly energetic emitting area known as a cathode spot. The localized temperature at the

cathode spot is extremely high (around 15000 °C), which results in a high velocity (10 km/s) jet of vaporized cathode material, leaving a crater behind on the cathode surface (Brown, 1998).

In the case of NCD deposition, the source material could be a piece of graphite fixed at the cathode, while the substrate is fixed at the anode, as shown in Fig. 1.4. However, in this deposition technique, target-substrate fixture geometry may be arranged in a few different ways. This process produces particles with a wide range of sizes and results in coatings that have large particulates in them. Macroparticles of carbon clusters, carbon ions and neutrals are produced by the arc. The ions, being charged atoms, form the plasma, and the particles are deposited onto a substrate (Ravi et al., 1996; Aoki et al., 2005).

Ravi and coworker were the first research group, in 1996, reporting on the growth of nanocrystalline diamond on silicon substrates using Filtered Cathodic Vacuum Arc (FCVA) method. Most of the crystals observed by transmission electron microscopy were indexed to both graphite and cubic diamond. The chemical composition of the crystals was analyzed using electron energy loss spectroscopy (EELS). The nanocrystallites of diamond may have formed either within the arc in the plasma phase or due to the kinetic processes involved in the rapid thermal quenching of the  $C^+/C^{++}$  ions. Also, since some of the crystallites found in the films are graphitic in nature, the graphitic macroparticles could be necessary for the pre seeding of the diamond nanocrystals (Ravi et al., 1996).

Almost a decade later, in 2005, Aoki and coworkers managed to grow three types of carbon films namely, graphite-like carbon, tetrahedral amorphous carbon, and NCD using a cathodic arc process. The deposition process has been carried out in ambient gases such as  $N_2$  and He, and at room temperature. The resulting films have been characterized by Raman spectroscopy and scanning electron microscopy. The diamond particles in NCD films were found to be formed at a constant total pressure of  $10^{-2}$  Pa, while graphite-like carbon was grown at a lower pressure of around  $10^{-3}$  Pa, and tetrahedral amorphous carbon was grown at a higher pressure such as  $10^{-1}$  Pa. Also, they have reported that diamond particles were randomly distributed in the films and had sizes in the range of 50–200 nm (Aoki et al., 2005).

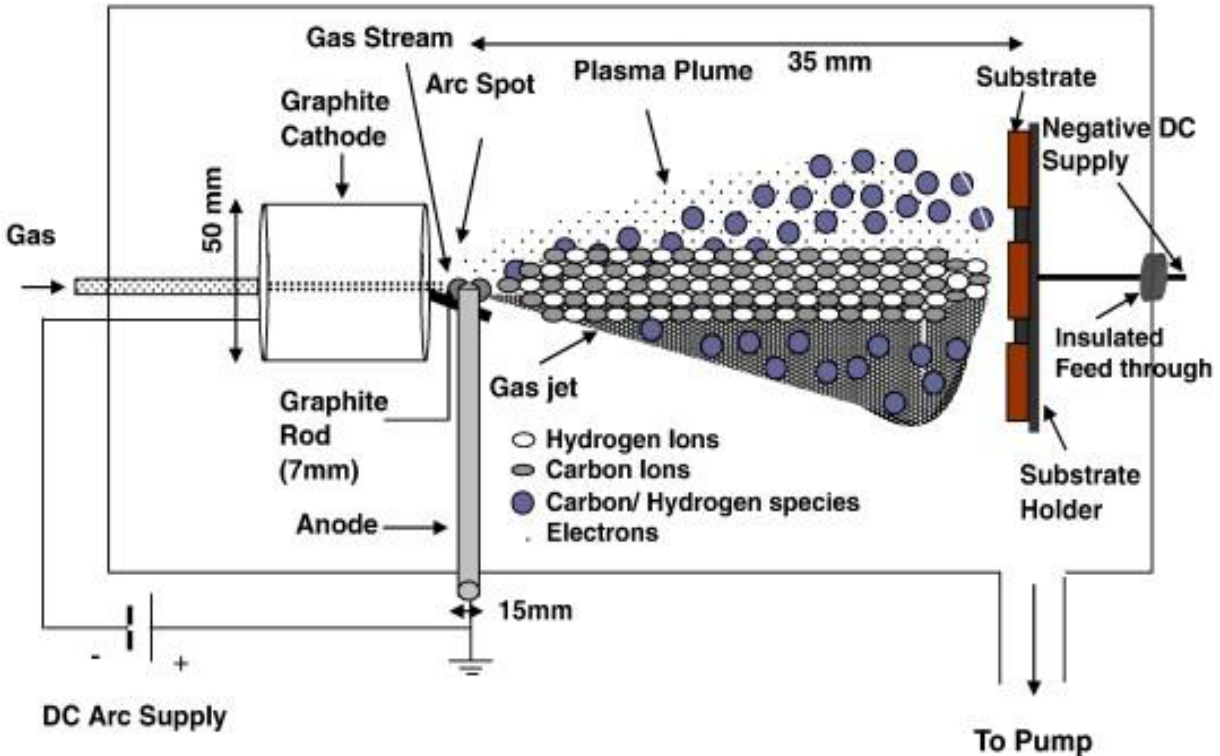


**Figure 1.4: Basic coating setup of cathodic arc plasma source (Panwar et al., 2012)**

Finally, in 2008, in the efforts towards preparing nano-diamond-DLC composite nanostructure, Xie and coworkers developed a technical procedure for the preparation of NCD-DLC composite films. The authors have deposited nanodiamond-cluster-embedded diamondlike carbon composite films on silicon wafers by electrophoresis deposition followed by magnetic filtered Cathodic Vacuum Arc plasma deposition. NCD clusters were found to be uniformly embedded into the resulting DLC films. These composite films show better field emission properties than the as-deposited DLC film and as-deposited nanodiamond clusters (Xie et al., 2008).

The advantages of using CVA to deposit NCD are many such as minimizing plasma losses, maximizing plasma throughput, and maximizing transport efficiency. However, the downsides of the process include: variable particles count and deposition rate, small area coverage, poor thickness uniformity, poor film quality, and poor repeatability and reliability for production processes (Brown, 1998; McKenzie et al., 1991; Ravi et al., 1996; Aoki et al., 2005).

### 1.2.4 Pulsed Laser Deposition (PLD)

In general, the idea of PLD is simple. A pulsed laser beam is focused onto the surface of a solid target. A pulsed laser concentrates its energy into brief bursts. An ultra-fast laser produces tremendous number of short bursts in which the intensity and power of the pulses can reach high levels. Because the pulses happen so quickly, the effects are concentrated in time. This gives ultra-fast lasers valuable properties that their slower predecessors did not have. Because of the strong absorption of the electromagnetic radiation by the target surface, pulsed laser beam can rapidly vaporize a thin section of a target material. The photons transfer their energy to electrons within the pico-second range ( $\sim 10^{-12}$  s), and the energy from the electron system is transferred to phonons within  $10^{-10}$  s (electron-phonon interaction time  $< 10^{-10}$  s). Thus, the photon energy ultimately appears as heat which can be used to produce melting and evaporation in a controlled way (Wei and Narayan, 2000). This process is known as ablation. The atoms at the target surface exhibit significant changes in their temperature, kinetic energy, and ionization state during this interaction. As a result of the interactions between the pulsed laser beam and the target surface, the target elements are rapidly heated up and form a nonequilibrium dense plasma directed perpendicularly to the target surface. This dense plasma is the primary precursor source material for film deposition (Voevodin et al., 1996; Robertson, 2002). The plasma pressure is orders of magnitude larger than any practical gas pressure in the process chamber. Thus, the plasma ejection is not affected by the presence of process gases. Under vacuum, the plasma experiences continuous acceleration due to the pressure gradient supported through recombination of atoms and electrons. During this phase, the original energy spectrum of the plasma flux is formed. In pulsed laser deposition processes, atoms from the target surface pass through several energy transformation phases before arriving at a substrate surface. Starting from their evaporation, the atoms are involved in a series of energy transfer processes controlled by different mechanisms. (Strikovski et al., 2010; Voevodin et al., 1996). If deposition takes place in a background gas, the flux of atoms collide with the gas atoms. As a result, the initial energetic spectrum of the atoms in the plasma would depend on the mean free path at a given pressure. Therefore the background gas, type and pressure, are considered to be among the main parameters that can affect thin film growth on a substrate. Other parameters are laser beam power, target-substrate distance, and substrate temperature. Figure 1.5 shows the

schematic view of a PLD system, which consists of excimer laser, focusing lenses, vacuum pump, process gas inlets, and target and substrate holders (Strikovski et al., 2010).

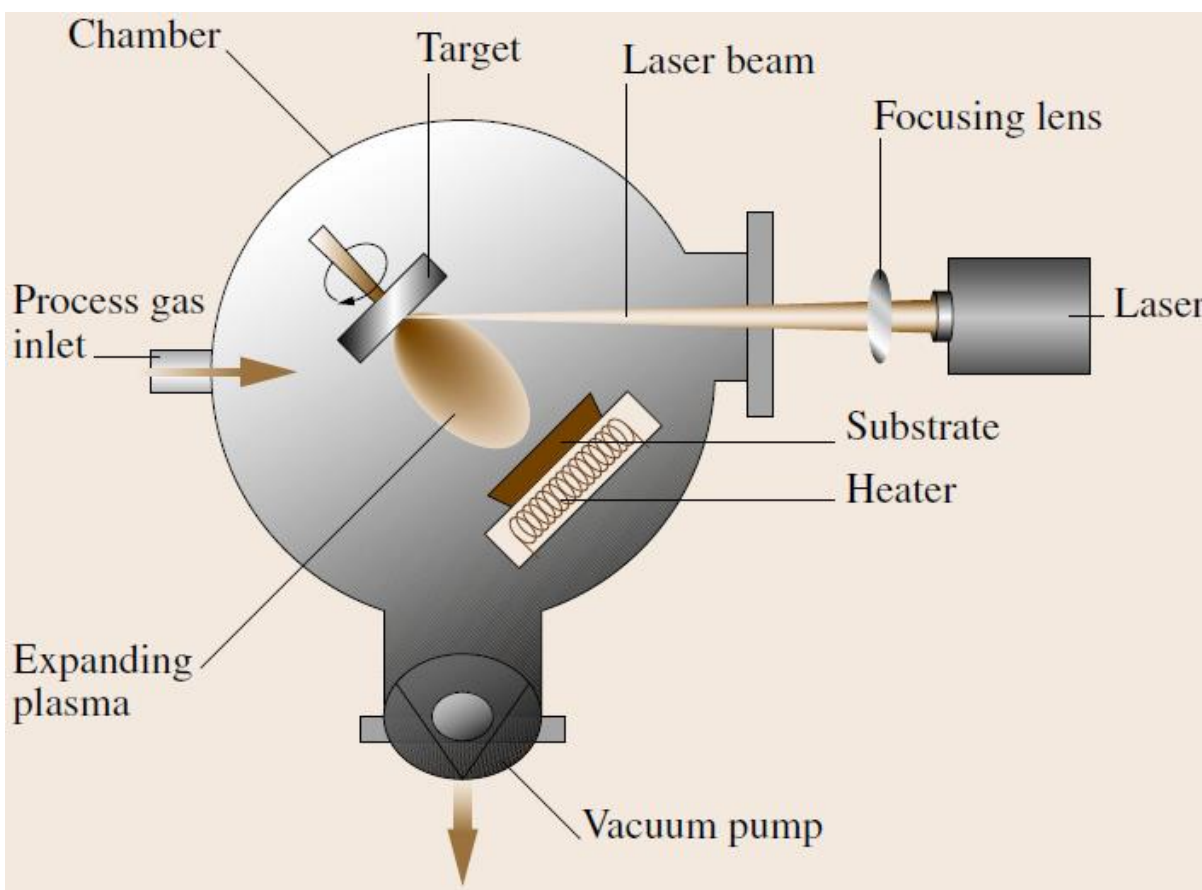


**Figure 1.5: Schematic of typical PLD system used for the deposition of NCD films (Strikovski et al., 2010).**

PLD has attracted some attention for the synthesis of nanocrystalline diamond. A special feature of PLD is that it is a non-equilibrium process and the species produced in the laser plasma possess very high kinetic energy. The photon energy is such that it might enable a 2s electron to be promoted to the 2p orbital and so leads to the formation of the  $sp^3$  hybridization that is the precursor of NCD constituents. At present, PLD competes with cathodic arc, ion beam, and other physical vapor deposition techniques for the deposition of high quality NCD films (Hongyan et al., 2000; Ou et al., 2003; Yoshitake et al., 2004).

In 2000, Hongyan and coworkers grew nanocrystalline diamond film on Si substrate using PLD operated at high laser power (500 W) and repetition rate (300 ~ 500 Hz). Their results have shown

that the deposition rate increases with the repetition rate of XeCl excimer laser. At higher repetition rate, high deposition rate is thought to be the result of the accumulative effect of the sputtering produced by the influence of the former pulses on the later pulses. Also, they have reported that more nano-particles of diamond exist in NCD films produced at higher energy fluence relatively to films produced at lower energy fluence (Hongyan et al., 2000).

In 2003, Yang -gang and coworkers deposited NCD films on mirror polished  $\alpha$ -Al<sub>2</sub>O<sub>3</sub> (0001) substrates using PLD. NCD films were prepared at a substrate temperature of 550 °C and a background gas of 6 Pa. They have reported that the surface of thin films prepared by pulsed laser deposition are uniform (Ou et al., 2003).

A year later, in 2004, Yoshitake and coworkers deposited NCD films on various substrates using reactive PLD technique at a substrate temperature of 550 °C. The deposition is considered reactive since it has been carried out under a hydrogen atmosphere at 533 Pa. NCD is grown on substrates with three different crystal orientations, namely, diamond 100, 110, and 111. The resulting NCD films exhibit smooth surfaces and crystallite diameters around 10-20 nm. Also, they have suggested that it is possible for the deposition rate to be enhanced further by using higher energy and repetition rate (Yoshitake et al., 2004).

In comparison with other deposition techniques, pulsed laser deposition (PLD) has many advantages, namely, the ability to deposit high quality films at room temperature. However, PLD apparatus is difficult to scale up to meet manufacturing requirements, it is not cost effective (both capital and maintenance) (Voevodin et al., 1996; Wei and Narayan, 2000).

### 1.3 Thesis Motivation

Pulsed laser deposition (PLD) has been the front-runner in its ability to achieve a high NCD thin films quality. An alternative method should retain the benefits of PLD, be cost effective and scalable for industrial applications. Pulsed electron beam ablation can be a potential candidate technique. PEBA and PLD are considered to be sister technologies in that both are based on pulsed forms of energy, albeit the physics is not the same.

In PLD, the mechanism of interaction with the target is governed by photons, however, in PEBA, it is governed by electrons. Thus, in PEBA, the energy transfer into the target surface is more effective than in PLD since wide band gap or highly reflective materials could be better ablated by the PEBA method.

The main differences between PEBA and PLD lie in the higher efficiency of the ablation process in the case of a pulsed electron beam, and significantly different beam-target interaction mechanisms. In PLD, the amount of ablation is very sensitive to the optical absorption coefficient of the target material (Jackson, 1997). In PEBA, ablation is independent of the optical properties of target materials. From an economic viewpoint, the capital and operating costs are likely to be significantly lower for PEBA than for PLD. This is a direct consequence of the energy conversion efficiency (electrical to electrical: ~30%) of the PEBA process relatively to PLD (conversion efficiency optical to electrical of only ~3%) (Venkatesan et al., 2005). Moreover, the cost of the electron source in PEBA is considered remarkably lower (about 10 times) than the cost of excimer laser typically used in PLD (Pattini, 1999).

Another important feature of pulsed electron beam ablation originates from the fact that it interacts less with atoms in the vapor phase (plume above target) compared to atoms in the solid state (target surface). However, in PLD, the pulsed laser beam interacts more or less equally with all atoms in both phases. Therefore, the plasma screening effect is less accentuated in PEBA compared to PLD (Harshavardhan and Strikovski, 2005; Muller et al., 1995).

## 1.4 Research Objectives

Owing to the technological importance of NCD in many applications (as discussed in Chapter 2) and due to the challenges encountered in the preparation of NCD via the numerous techniques discussed previously, there is a need to assess alternative deposition techniques in the hope of preparing good quality and cost effective NCD films. The present research attempts to address some of these shortcomings. The main objectives of my research are to:

- 1- Select and optimize process conditions and electron beam parameters for the deposition of NCD films by PEBA. Deposition conditions such as chamber gas pressure, substrate temperature, substrate material, substrate-target distance and geometry, electron beam tube tip-target distance,

and background gas. Electron beam parameters include beam cross section ( $\text{cm}^2$ ), pulse energy density ( $\text{J}/\text{cm}^2$ ), discharge voltage (kV), and pulse repetition rate (Hz).

2- Characterize the properties of the resulting NCD films using different techniques such as Raman Spectroscopy, Visible Reflectance Spectroscopy, X-Ray Diffraction (XRD), Atomic Force Microscopy (AFM), Scanning Electron Microscopy (SEM), and nanoindentation. These techniques will be used to measure different properties of NCD thin films, namely, structure, chemical composition, morphology, thickness, and hardness.

3- Correlate various film properties with process parameters.

## **Chapter 2: NCD Microstructure, Properties, and Applications**

## 2.1 Carbon Material

The element, carbon, is one of the most versatile elements on earth in terms of its abundance and the number of compounds it may form. Understanding the hybridization of its orbitals is important when discussing amorphous or crystalline carbon systems. A neutral carbon atom has six electrons, which are distributed to fill in the 1s and 2s subshells and the remaining two electrons occupy the 2p level,  $1s^2 2s^2 2p_x^1 2p_y^1$ . However, electrons distribute themselves in the way that leads to their most stable arrangement. Therefore, hybrid orbitals would rearrange themselves in carbon to form the excited configuration,  $1s^2 2s^1 2p_x^1 2p_y^1 2p_z^1$ , with four unpaired electrons. Carbon could form a variety of crystalline and disordered structures because of its ability to exist in three hybridizations,  $sp^3$ ,  $sp^2$  and  $sp$ , as shown in Fig. 2.1 (Fox and Whitesell, 2004). In the  $sp^3$  configuration, a carbon atom's four valence electrons are each assigned to a hybrid orbital. Such combination of the hybrid orbitals produces a tetrahedral assembly with the center of masses in the corners. The characteristic angle between the hybrid orbitals in  $sp^3$  configuration is  $109^\circ$ ;  $sp^3$  structures consist of  $\sigma$  bonds only. A typical example of a  $sp^3$ -hybridized crystal structure is diamond. In the  $sp^2$  configuration, three of the four valence electrons form trigonally directed  $sp^2$  orbitals. They contribute together to a planar assembly with a characteristic angle of  $120^\circ$  between hybrid orbitals forming  $\sigma$  bonds. The fourth electron of the hybrid  $sp^2$  atom lies in a p orbital, normal to the  $\sigma$  bonding plane. This p orbital forms a bond, called  $\pi$  bond, with another p orbital on a neighboring atom.  $\pi$  bonds are significantly weaker compared to  $\sigma$  bonds. In the  $sp$  configuration, two of the four valence electrons enter  $\sigma$  orbitals, each forming a  $\sigma$  bond directed along the  $\pm x$ -axis, and the other two electrons (from p orbitals) enter  $\pi$  bonds in the y and z directions (Donnet and Erdemir, 2007).

In solids, the valence band is the highest range of electron energies in which electrons are normally present at absolute zero temperature. While the conduction band is the range of electron energies higher than that of the valence band, sufficient to free an electron from binding with its individual atom and to allow it to move freely within the atomic lattice of the material.

Energetically, electrons occupying conduction band states are more loosely bound than those in the valence band.  $\sigma$ ,  $\sigma^*$ ,  $\pi$ , and  $\pi^*$  occupied and unoccupied (\*) orbitals are particularly common terms in the topic of molecular systems, but are often used for crystal or solid state structures. The

$\sigma$  bonds of all carbon sites form occupied  $\sigma$  states in the valence band and empty  $\sigma^*$  states in the conduction band, separated by a wide  $\sigma$ - $\sigma^*$  gap, see Fig. 2.2. The  $\pi$  bonds of  $sp^2$  and  $sp^1$  sites form filled  $\pi$  states and empty  $\pi^*$  states, with a much narrower  $\pi$ - $\pi^*$  gap (Robertson, 1986; Robertson, 2002).

### 2.1.1 Amorphous Carbon

Carbon may make crystalline or amorphous structure. Crystalline solids could be easily distinguished from amorphous solids. Amorphous solids do not possess a long-range periodic arrangement of building units, atoms, and their atomic structure is characterized by the absence of any long-range order. Actually, the nearest neighbor sequence of an atom in amorphous solids are well defined by virtue of chemical bonding requirements. Amorphous carbon (a-C) holds true to this nature; it lacks the crystalline order of diamond or highly ordered pyrolytic graphite (HOPG). In a sense, one could think of amorphous carbon as having a mixture of diamond ( $sp^3$ ) and graphite ( $sp^2$ ) bonding characteristics.

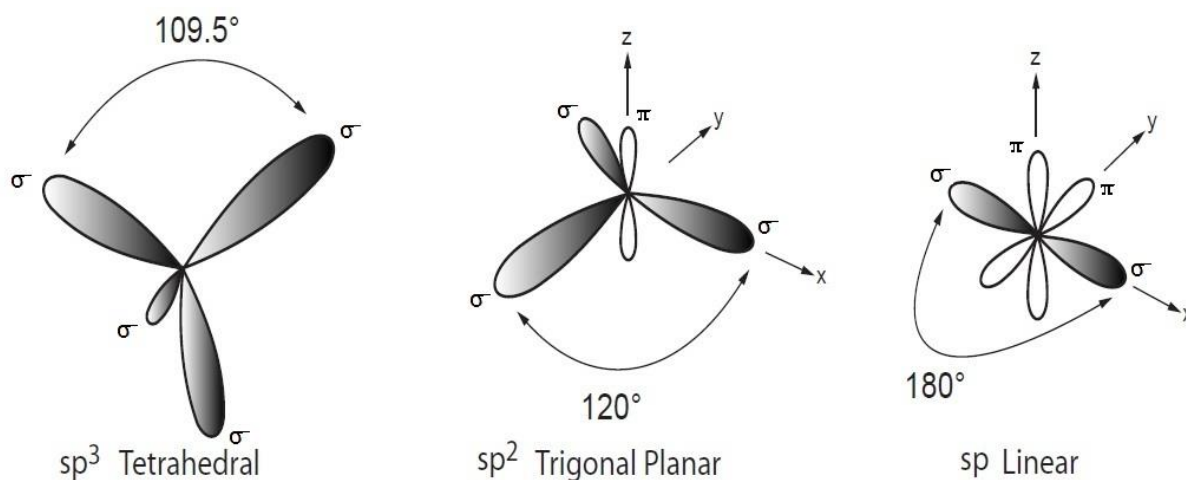


**Figure 2.1: The  $sp^3$ ,  $sp^2$ ,  $sp^1$  hybridized bonding (Matzinger 2006).**

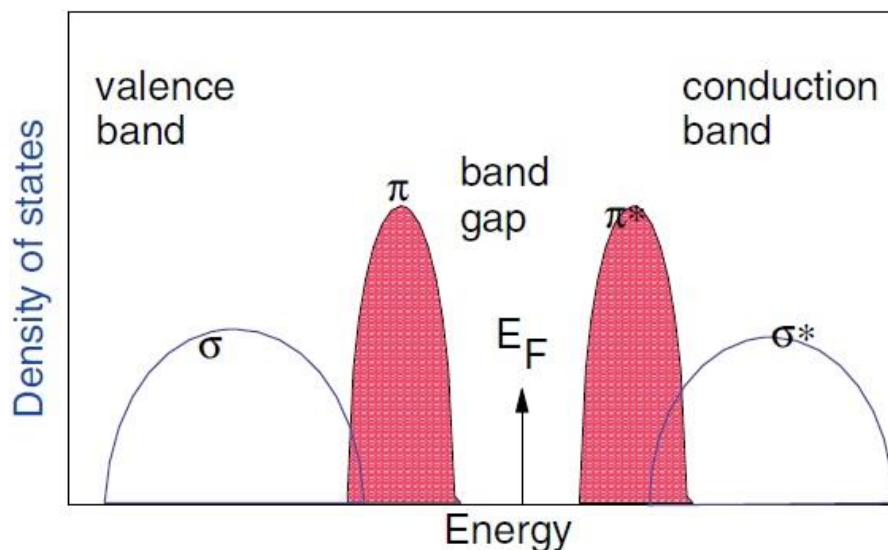


**Figure 2.2: Schematic density of states of amorphous carbon (Robertson, 2008).**

Robertson and O'Reilly (1987) have investigated the electronic structure of amorphous carbon through calculations on a number of model structures containing different configurations of  $sp^2$  and  $sp^3$  sites. They have reported that the most stable arrangement of  $sp^2$  sites is in benzene-like rings, i.e., graphitic layers. Evaporated amorphous carbon (a-C) forms such clusters of disordered graphitic layers of about 1.5 nm in diameter, bonded by  $sp^3$  sites. Also, it was argued that increasing the  $\pi$  bonding energy tends to cause  $sp^2$  sites to form  $\pi$  bonded clusters within a  $sp^3$  bonded matrix (Robertson and O'Reilly, 1987).

There is a difference in behavior of  $\sigma$  and  $\pi$  states in carbon. The  $\sigma$  states form a network of  $sp^3$  sites. However,  $\pi$  states favor a clustering of  $sp^2$  sites because of the energy gain compared to a random distribution of  $sp^2$  and  $sp^3$  sites. A network of  $\pi$  states may result in a half-filled band. Clearly, the binding energy of the occupied states is lowered if a gap is created in this band at the Fermi level,  $E_F$  (see Fig. 2.2). To increase the  $\pi$  interaction, therefore, a parallel alignment is expected for any pair of  $sp^2$  sites, as in ethylene. Molecules gain stabilization energy from the delocalization of  $\pi$ -electrons, so ethylene-like C=C units tend to group into a six-fold ring, as in benzene. Extra stability gain would occur if the six-fold benzene rings condense into graphitic sheets. The  $sp^2$  sites tend to be arranged in planar,  $\pi$  bonded clusters of certain size, embedded in an  $sp^3$  bonded matrix. The arrangement of the  $sp^2$  sites controls the electronic properties and the optical gap, because their  $\pi$  states lie closest to the Fermi level, while the  $sp^3$  matrix controls the

mechanical properties (Robertson, 1986; Robertson and O'Reilly, 1987; Robertson, 2002; Rittner and Bailey, 2005).

### 2.1.2 Crystalline Carbon

The crystalline state of matter is the state with the highest order, i.e., with very high internal correlations and at the greatest distance range. This is reflected in their properties: anisotropic and discontinuous. Crystals usually seem to form as unadulterated, homogenous and with well-defined geometric shapes when they are well-formed. However, their external morphology is not sufficient to evaluate the crystallinity of a material.

The two most common crystalline allotropes of carbon are diamond and graphite. Graphite and diamond are two of the most interesting materials. They are identical chemically since both are composed of carbon. However, they are physically very different. Graphite is opaque and exhibits a metallic look, while diamonds are brilliant, see Fig. 2.3. Another important physical difference is their hardness. Graphite is very soft compared to diamond, which is one of the hardest known natural substance. The crystal structure of graphite yields physical properties that permit the use of graphite as a lubricant or as pencil lead. The gem and industrial properties of diamond, physical properties that we cherish and exploit, are also a result of diamond's crystal structure (Miller et al., 2009).



**Figure 2.3: Graphite figure is on the left. Diamond figure is on the right (Graphite, 2013; Diamond Crystallography, 2013).**

The structure of graphite consists of flat layers. In each layer the carbon atoms are arranged in a regular hexagonal array. We can regard each layer as a large number of benzene rings fused together to form a gigantic honeycomb. All carbon-carbon bonds in this honeycomb are equivalent and intermediate in character between a single and a double bond (Mantell, 1968). While there are strong covalent bonds between the carbon atoms in a given plane, only weak London forces attract the planes together, see Fig. 2.4.

Diamond is the  $sp^3$ -bonded structure of carbon. Figure 2.5 shows a unit cell of diamond crystal, which is composed of eight corner atoms, six face-centered atoms and four internal atoms along the cube diagonals. A diamond unit cell contains eight C atoms. Each of the carbon atoms is covalently bonded to four nearest neighboring atoms to form a tetrahedral configuration. The crystal structure can be viewed as two interpenetrating FCC lattices, offsetting from one another along a body diagonal by one-quarter of its length. The (111) planes of diamond are along the bond direction with a lattice constant ( $a_0$ ) of 3.567 Å and a bond length of 1.54 Å. Due to this unique chemical bonding, and atomic density of  $1.76 \times 10^{23} \text{ cm}^{-3}$ , diamonds possess several extraordinary material properties (Asmussen and Reinhard, 2002).

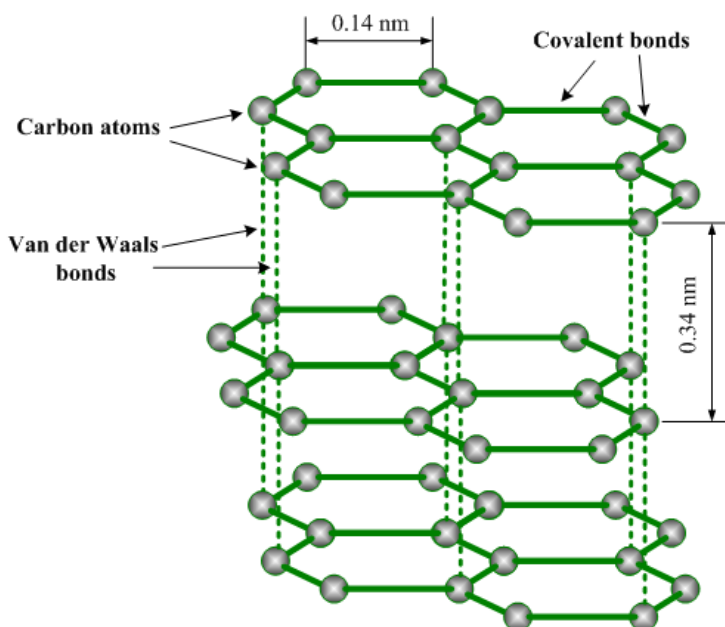


**Figure 2.4: Chemical structure of graphite (Mantell, 1968).**

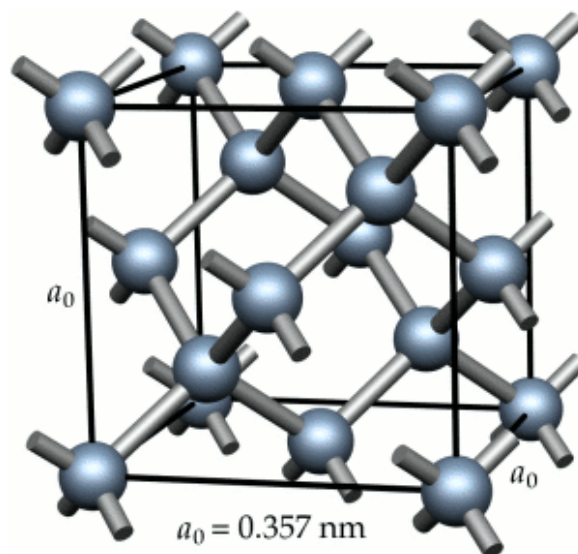


**Figure 2.5: Chemical structure of diamond (Asmussen and Reinhard, 2002).**

Graphite is only a few electron volts (per atom) more stable than diamond, but the activation barrier for converting graphite to diamond requires almost as much energy as destroying the entire lattice and rebuilding it. Diamonds consist of extremely strong and rigid lattices of carbon atoms. Therefore, once diamond is formed, it will not easily revert back to graphite because the activation barrier is too high in value of energy. Diamonds are said to be metastable, since they are kinetically rather than thermodynamically stable. Under the high pressure and temperature conditions needed to form diamond, the latter is actually more stable than graphite, and so over millions of years, carbonaceous deposits may slowly crystallize into diamond (Ferro, 2001).

## 2.2 Microstructure of Nanocrystalline Diamond

Nanocrystalline diamond is a nanocomposite material. Such materials are composed of elements like grains, crystallites, layers, e.g., of a size of ca. 100 nm. NCD is best described as two mixed phases. The first phase consists of diamond crystallites (diamond grains) imbedded in a second phase called diamond-like amorphous carbon matrix or intergrain phase. At the interface between these two phases, there is a third phase that can be distinguished and called grain boundaries, see Fig. 2.6. However, the grain boundaries and the amorphous carbon matrix could be considered as one phase due to the small volumes of the amorphous carbon regions (Sharda et al., 2001; Dischler et al., 1993).

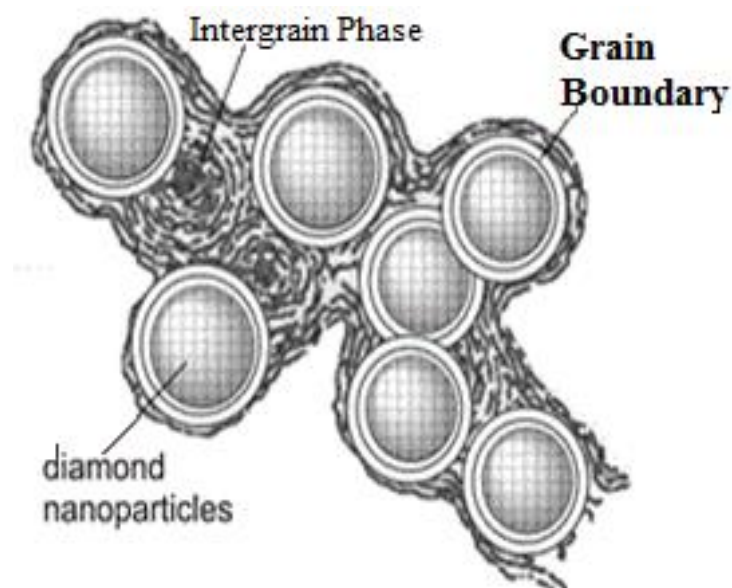


**Figure 2.6: Structure of NCD material (Krueger, 2008).**

Cote and coworkers (1998) have studied a highly symmetric three-dimensional  $sp^2$  bonded structure of carbon. Another research group, Liu and Cohen (1991) have studied the structural properties of a proposed, hypothetical,  $sp^2$  phase of carbon, using the first-principles pseudopotential total-energy method. Both research groups, in their model, have proposed an all- $sp^2$  structure that can yield a high bulk modulus and low bulk modulus as determined by the lengths of the bonds between carbon atoms. Moreover, many experimental results have confirmed the possibility of the film structure to be composed of a matrix of dispersed cross-linked  $sp^2$  sites that provide the network of carbon atoms with rigidity (Lacerda and Marques, 1998; Alexandrou et al., 1999).

The grain size of a nanocrystalline diamond film would determine film roughness and the surface to volume ratio. As diamond grains decrease in size, the surface smoothness of films increases making it a promising material for tribological applications. Second, the surface to volume ratio is the main determining factor in  $sp^2$  content. Apparently, smaller grains result in higher surface area, which in turn lead to a higher  $sp^2$  content due to the enhanced grain boundary volume. Whilst it is true that not all grain boundaries are equal, all must contain some  $sp^2$  bonding and thus less grain boundaries will generally result in a higher overall percentage of  $sp^3$  bonding (Rakha et al., 2010; Williams, 2011).

## 2.3 Properties and Applications of Nanocrystalline Diamond

Diamond has many fascinating properties such as the highest hardness, stiffness, thermal conductivity, smoothness, and chemical inertness. Diamond would undoubtedly be the material of choice for many applications, if it were inexpensive and abundant. Therefore, during the last several decades, scientists have been interested in producing cost effective materials which resemble most of diamond properties for use in various engineering applications (Brookes and Brookes, 1991).

High-quality crystalline diamond films exhibit most of the desired properties of natural diamonds. Crystalline diamond films are generally classified into two categories, with respect to their grain size, as microcrystalline diamond (MCD) and nanocrystalline diamond. They are made up of large columnar grains that are highly faceted and generally rough. MCD films generally exhibit rougher surfaces compared to NCD (Erdemir et al., 1999). The grains in MCD films may exhibit (111) or (100) crystallographic growth orientations, as shown in Fig. 2.7 (A) (Erdemir et al., 1999).

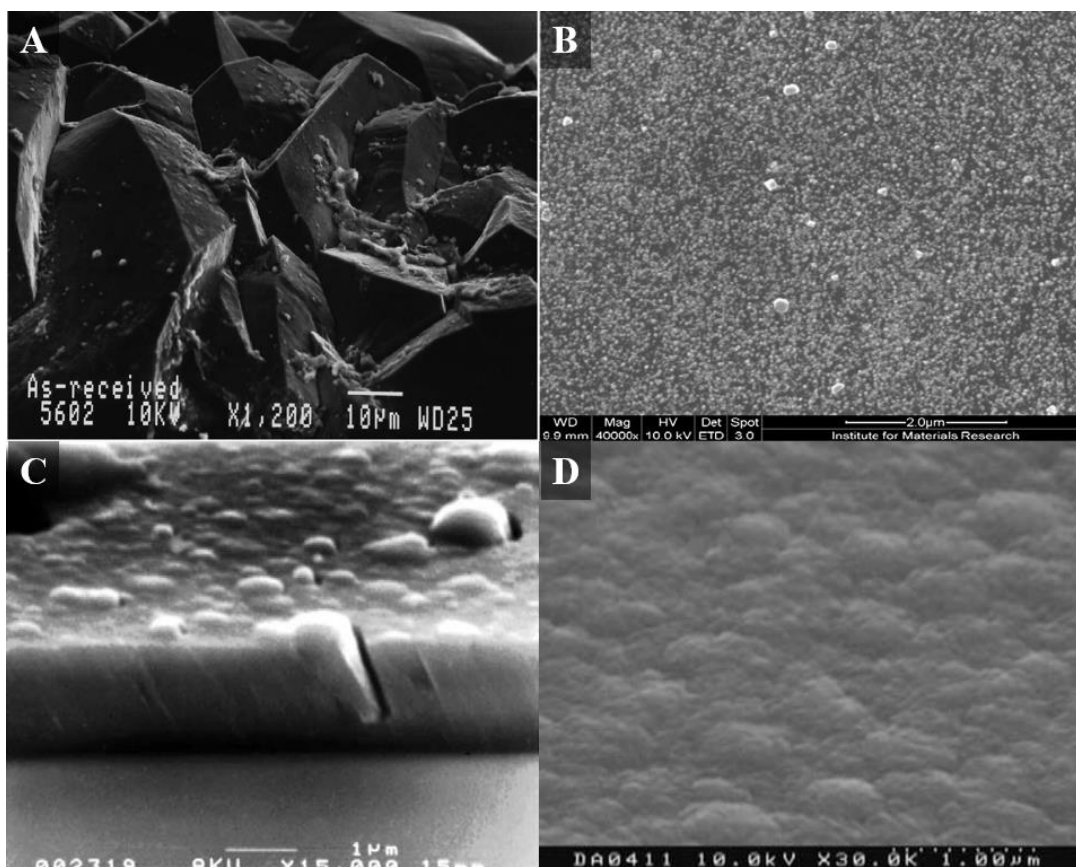


Figure 2.7: SEM images of MCD and NCD films.

NCD films can exhibit different morphologies as depicted through SEM images in Fig. 2.7 (B) (Williams, 2011), (C) (Chu and Li, 2005), and (D) (Popov et al., 2007). However, their crystallographic orientations depend mainly on the deposition method and conditions. The rough surface finish of MCD films precludes their immediate use for most machining and wear applications. However, the polishing processes are tedious, take a very long time, and, in the case of complex geometries, they are very impractical. Therefore, recently, it has been shown that NCD coatings can overcome this problem as the nanocrystalline nature of such coatings leads to very smooth surfaces while the properties of diamond still prevail. Nanocrystalline diamond has found its way to many applications such as electrical, tribological, optical, and biomedical applications (Holt et al., 2007). Its beneficial properties (as listed in Table 2.1) such as chemical inertness, interesting electronic and mechanical properties, the stability of luminescent lattice defects, and other characteristics make NCD an ideal material in many fields. Many useful applications of NCD have been developed accordingly. Depending on the size of grains in NCD, their purity and surface termination, they can be employed in composite materials, as surface coatings, as carriers for drugs, and as labels in biological systems (Krueger, 2011).

In 1999, Erdemir and coworkers conducted friction tests by sliding  $\text{Si}_3\text{N}_4$  balls against both MCD and NCD films in open air and dry  $\text{N}_2$ . They have reported that surface roughness of MCD films is remarkably higher compared to surface roughness of NCD films, which exhibit lower friction in this test. Erdemir and coworkers (1999) have attributed the higher friction of MCD films to the abrasive cutting and plowing effects of sharp asperity tips on softer counter-face pins.

In addition to surface roughness, in all diamond films, surface chemistry and surface-adhesive interactions can also play a significant role in the friction and wear performance (Gardos and Ravi, 1994). For instance, the passivation of dangling bonds at the surface of diamond films by any gaseous adsorbates (such as  $\text{H}_2$ ,  $\text{N}_2$  or  $\text{O}_2$ ) would lower their friction (Gardos, 1996).

The optical and electrical properties of nanocrystalline diamond (NCD) thin films have attracted renewed interest, mainly due to the appearance of a very high n-type conductivity which could be induced by doping with various elements such as nitrogen or boron. While the  $\text{sp}^3$  phase of diamond grains influences its mechanical properties, the  $\text{sp}^2$ -bonded carbon atoms in the grain boundaries control the films electronic and optical properties (Zapol et al., 2001; Fyta et al., 2007).

Electrical conduction may occur in the grain boundaries, most probably by hopping and impurity band conduction.

NCD, with its hardness and the possibility to modify its surfaces or tailor its properties according to the requirements of the composite formation, is a perfect candidate to produce suitable composites for many applications. In 2010, Kovalenko and coworkers proposed the use of NCD composites in the production of supercapacitors (Kovalenko et al., 2010). Another research group, Zhao and coworkers (2010), have reported the synthesis of biocompatible nano-composites with improved mechanical and thermal properties consisting of poly-(lactic acid) (PLLA) and nano-diamond.

**Table 2.1: Some properties of NCD at room temperature.**

Property	Value	Reference
Microhardness (GPa)	10 - 80	Yang et al., 2002; Narayan et al., 2006; Wiora et al., 2011; Booth et al., 2011
Young's modulus (GPa)	500 - 1000	Philip et al., 2003; Narayan et al., 2006 Wiora et al., 2011
Wear Rate Coefficient (mm <sup>3</sup> )	10 <sup>-8</sup> – 10 <sup>-6</sup>	Wiora et al., 2011; Kumar et al., 2012
Coefficient of friction	0.05 – 0.5	ElSay, 2011; Kumar et al., 2012
Roughness (nm)	10 - 30	Yang et al., 2002; Booth et al., 2011; Sharda et al., 2003
Thermal conductivity (W/mK)	20 - 1000	Bozorg-Grayeli et al., 2013; Balachandran, 2009
Electrical resistivity (Ω.cm)	~ 10 <sup>11</sup>	Ramamurti, 2006; Jackson and Ahmed, 2007
Refractive index (in the near IR)	2.33- 2.44	ElSay K., 2011; Sharda et al., 2003

Achatz and coworkers (2006) have suggested that the grain boundaries play a major role in the photocurrent levels of NCD films. Apparently in these films,  $sp^2$  and  $sp^3$  sites occur together in the highly disordered grain-boundary regions and a sufficient bond angle distortion can enhance  $\pi$ - $\sigma$  bond mixing. This distortion and band mixing would allow transitions from the  $sp^2$ -related  $\pi$  states to the antibonding distorted  $sp^3$  states or to the valence-band tail region. Moreover, band tail to band tail and band-to-band transitions can also contribute to the optical absorption at high energies of the films (Gajewski et al., 2009).

The distortion of bonds is caused by the geometrical constraints due to the surrounding carbon lattice. These distortions may occur less due to the weak restrictions and less confinement exhibited in the grain-boundary regions compared to the diamond bulk. Therefore, as a result of the flexibility status of the bonds in the grain-boundary, no bond breaking is required. In NCD films, hopping takes place between dimers, i.e., perpendicular to the plane of grains boundary making the hopping length small. However, due to lack of connectivity along the plane of the grains boundary conductivity is poor and the measured hopping distance is large. This poor connectivity opens up a finite energy gap and less conductivity can be expected (Gajewski et al., 2009; Bhattacharyya, 2004). The transport properties of the grain boundary in NCD films could be explained on the basis of the electronic structure of amorphous carbon. Amorphous carbon films can be distinguished into two categories, gapped a-C and gapless a-C, where a finite energy gap is either present or absent and they are found to manifest entirely different temperature-dependent conductivity (Nesladek et al., 1998; Gajewski et al., 2009).

The inclusion of dopants (such as nitrogen) in diamond nanoparticles is expected to be important for use in future nanodevices, such as qubits for quantum computing. In 2005, Barnard and Sternberg suggested that NCD doped with nitrogen could be the basis for a quantum computer. Quantum applications require the creation of reliable single photon sources; namely applications such as quantum key distribution rely on the emission of one and only one photon at a time. Additionally, the small size of the individual diamond crystals helps to increase the photon collection efficiency by mitigating refraction effects (Greentree et al., 2010).

NCD coatings could be used in electrochemical and catalytic applications. Due to their structure, they would exhibit different behaviour as compared to other forms of carbon. Navalon and

coworkers (2011) have suggested that various metals such as platinum, palladium, and gold could be deposited onto NCD. They can be used as highly active catalysts for the Fenton reaction. Another research group, Turova et al. (2011), have proposed that NCD films may fit as catalysts for the hydrogenation of multiple bonds. One year earlier, Zhang and coworkers (2010), reported that NCD itself exhibits catalytic activity, and managed to dehydrogenate ethylbenzene using NCD.

One of the outstanding properties of NCD films is their inertness in biological environments. NCD triggers a milder foreign body reaction compared to other materials. The foreign body reaction (FBR) is a response of biological tissue to any foreign material in the tissues. Tissue-encapsulation of an implant and inflammations are part of this reaction. FBR consists of protein adsorption, macrophages, multinucleated foreign body giant cells (macrophage fusion), fibroblasts, and angiogenesis. Moreover, FBR may induce what is called free radical toxic reactions (Anderson et al., 2004). Inside the human body, the free radical toxic reactions damage cells and tissues. NCD coatings can play a protective role by slowing down such reactions. Therefore, NCD coatings are thought to be bioinert materials with no toxic reactions, and interact positively with the living organism. Moreover, carbon as a basic component of the human tissue structure is an ideal material to construct implants for medical applications (Bakowicz and Mitura, 2002). In vitro NCD was found to inhibit lipid peroxidation in blood plasma, while in vivo (on a male rat), after a couple of weeks, the presence of NCD material showed no remarkable reaction from the rat cells and tissues. However, after 21 days, the inflammatory process appears in liver, kidneys and peritoneum but the amount of inflammatory cells was very small. These results indicate that NCD is to a good extent a biocompatible biomaterial for the human body (Bakowicz and Mitura, 2002).

In drug delivery applications, NCD could be used for the adsorption of drugs due to its small particle size and, hence, its large specific surface area. Lam and coworkers (2008) have reported the use of NCD as a non-covalently bound carrier for the delivery of antitumor agents such as doxorubicin. Li et al. (2010) have managed to use NCD as a carrier for the delivery of 10-hydroxycamptothecin (HCPT) agent. A third research group, Liu et al. (2010), have covalently grafted paclitaxel onto the surface of diamond and delivered it to A549 human lung carcinoma cells.

Another biomedical application is biolabelling in organisms and cell cultures using the inherent luminescence of lattice defects in NCD. Using NCD in such an application has many advantages: The luminescence does not bleach, blinking is not observed in most cases, and the photophysical properties of the underlying structure are well-understood. Moreover, it is possible to produce NCD containing a sufficient amount of the lattice defects in mass production (Jelezko and Wrachtrup, 2006; Chang et al., 2008).

As per separation techniques, due to mechanical stability, NCD withstands high pressures and can therefore be used as the stationary phase in high-performance chromatographic applications. Chromatography is the collective term for a set of laboratory techniques for the separation of mixtures. The process begins with mixture dissolving in a fluid, which results in a mobile phase. The mobile phase carries the mixture through a structure holding another material called the stationary phase. The various constituents of the mixture travel at different speeds, causing them to separate. The separation is based on differential partitioning between the mobile and stationary phases. Differential partitioning would result in differential retention on the stationary phase. Spitsyn and co-workers (2010) have reported on the production of surface modified NCD coatings for ion exchange in gaseous and liquid chromatography.

## **Chapter 3: Experimental Procedure**

## 3.1 Introduction

This chapter gives details of the experimental procedure followed in this research work. The procedure includes substrate preparation, film deposition, heat treatment, and films characterization. In the following, a brief overview is given of PEBA setup, high-temperature furnace, and various analytical techniques used to characterize NCD coatings.

## 3.2 Pulsed Electron Deposition

### 3.2.1 The Physics of Pulsed Electron Ablation

Pulsed electron beam ablation (PEBA) is a relatively novel deposition technique with some unique advantages, such as technical capabilities, cost effectiveness, and high energy efficiency. The discovery of the pseudospark discharge by Christiansen and Schultheiss (1979) has opened up the way for a number of studies on pulsed electron beams and their applications in many fields including thin film deposition (Christiansen and Schultheiss, 1979). In 1990, Hobel and coworkers were the first research group that used PEBA for thin film deposition. PEBA was first used in a simple design called pseudo-spark configuration where the low pressure gas discharge occurs between a planar anode and a hollow cathode specially designed for particular and unique charged particle emission characteristics (Matacotta and Ottaviani, 1995). The energy beam is formed by electrons generated in a plasma inside a hollow cavity and driven through a background gas. Afterwards, a new design of PEBA system called Channel Spark was developed. The new design uses new accelerator parts, which allow for higher conversion efficiency of electrical energy ~30% against an efficiency of only 4% for the pseudo spark discharge (Venkatesan et al., 2005).

PEBA system consists of a pulsed electron beam generator (pulsed electron beam source), a stainless steel deposition chamber, target and substrate holders, target and substrate rotating motors, substrate heater, and vacuum system (Neocera Inc., 2011). Figure 3.1 shows a simplified schematic of the main pulsed electron beam chamber components. Figure 3.2 is a snapshot of the PEBA system available in Dr. Henda's laboratory at Laurentian University. The stainless steel chamber is pumped by a combination of a turbo molecular pump and a rotary pump reaching a pre-deposition pressure in the order of  $10^{-6}$  Torr. The rotary pump is usually used first to pump the

chamber down from atmospheric pressure to about  $10^{-3}$  Torr. Later, the turbo molecular pump takes over to allow pre-deposition pressure in the chamber to reach high vacuum, typically around  $10^{-6}$  Torr.

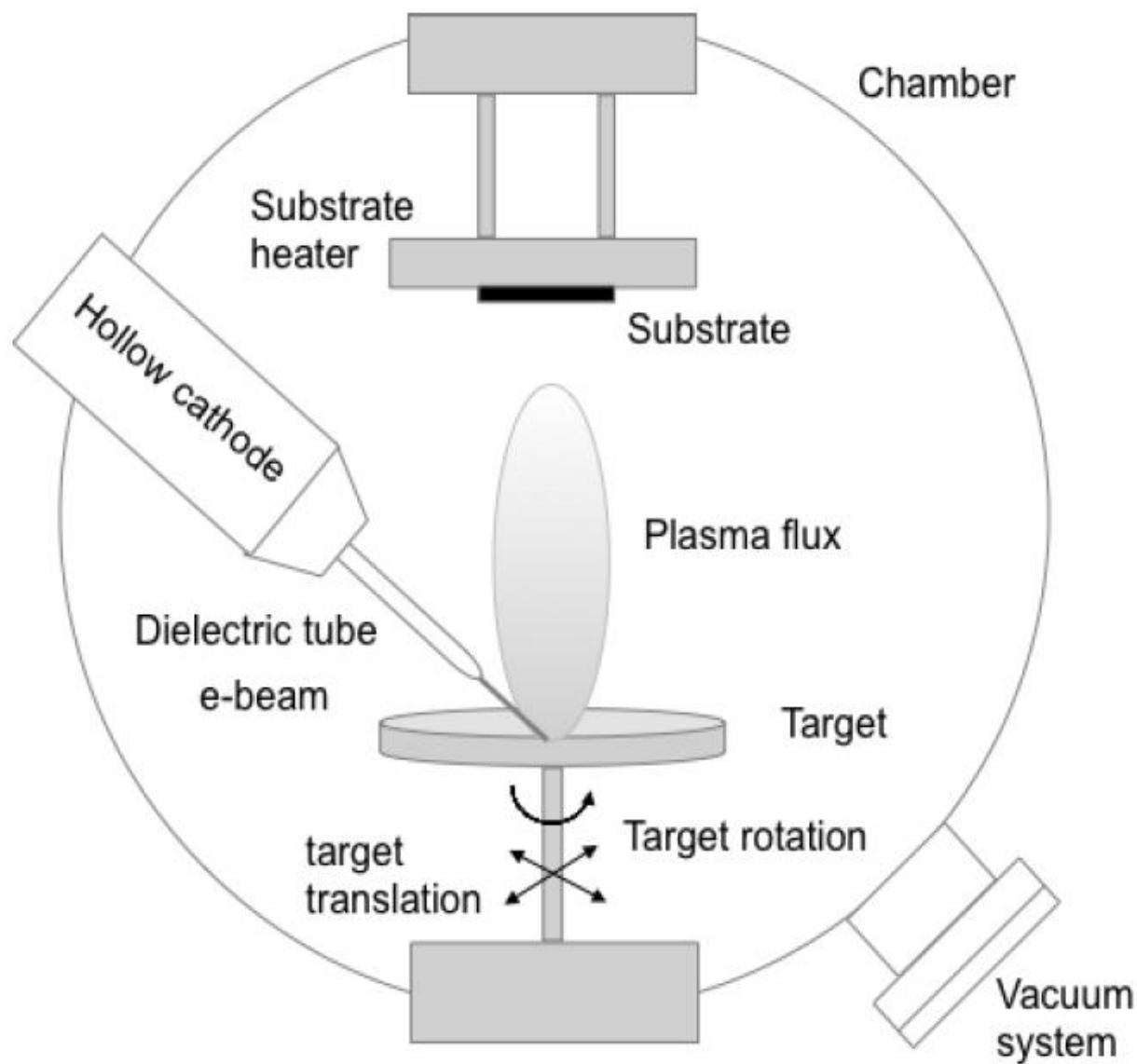


Figure 3.1: Simplified schematics of a PEBA system (Henda et al., 2012).



**Figure 3.2: Neocera PEBA system.**

The electron source for high currents is modified to operate in a pulsed mode only. Neocera PEBA system uses a pulsed electron source of channel spark configuration. The channel spark is the most efficient transient hollow cathode (THC) configuration for electron beam generation. THC is a low-pressure gas discharge electron source, which develops a well-focused electron flow with currents up to several kilo amperes and a pulse duration of  $\sim 100$  nanoseconds. The inner wall of the hollow cathode delivers electrons and is loaded with a current density up to  $1 \text{ kA/cm}^2$ , just below the value at which surface would melt (Venkatesan et al., 2005). If the generated beam is sufficiently intense and propagating in the deposition chamber, a self-pinch force develops naturally as the beam ionizes the background gas and creates a conducting plasma. The plasma fully neutralizes the beam space charge but is too resistive to fully neutralize the beam current. Therefore, a finite net current, which equals to the sum of the beam current and the plasma return current, would result. This current flows parallel to the beam. The net current pinches the beam

magnetically, restricts its radial expansion, and allows its longitudinal expansion. Plasma self-pinching is the feature that enables beam propagation, and thus target ablation, inside the deposition chamber without external guide fields (Fernsler et al., 1994; Myers et al., 1996).

The ablation process is triggered once the pulsed electron beam hits the surface of target. Due to the pulsed nature of PEBA, the energy of the beam is confined within a thin subsurface layer of a target, which is thought to be in the range 1-2  $\mu\text{m}$ . Such energy confinement would lead to effective instantaneous conversion of absorbed energy (energy of electrons) into heat. Energy absorption in such a diminutive volume of material results in a jet evaporation at the surface of the target. The vapor cloud at the surface continues absorbing the majority of the pulse energy, gets ionized, and becomes a plasma. Expansion of the dense plasma, driven by a pressure gradient, in a direction perpendicular to the surface is seen as a plasma jet (plume). The plasma plume (high energy species), generated at the surface of the target after the interaction with the energy beam, expands in the direction of the maximum pressure gradient at a velocity of about  $10^4$  m/s (Nistor et al., 2011). The plasma layer ejects itself in a perpendicular direction to the target surface as the plasma pressure is much higher than the chamber background gas pressure (Redel et al., 1992; Toftmann et al., 2003). It is worth mentioning that for the electron beam, there is no reduction in intensity due to the vapor plasma shielding effect. Throughout the entire pulse length, the electron beam continues to interact with the same number of atoms as contained within the beam absorption range in the target (Strikovski et al., 2003; Strikovski et al., 2010). Moreover, the efficiency of energy conversion from the electron beam to the target material (electrical-electrical) is  $\sim 30\%$ , which makes pulsed electron beam ablation quite energy efficient (Muller et al., 1995; Venkatesan et al., 2005; Aga et al., 2006; Strikovski et al., 2010).

Variations in pulsed electron energy, background gas chemistry and pressure, and distance between channel spark tube tip and target surface, can be used to manipulate ablation spot size and plume propagation and characteristics. Ablation spot size and plume characteristics affect other deposition conditions significantly (Strikovski and Miller, 1998; Pattini et al., 1999; Gilgenbach et al., 1999; Christen et al., 2005). The minimal absorbed power density  $Q$ , in Equation (3.1), is the ablation threshold. It is controlled by the rate of surface temperature rise  $\Delta T$  as:

$$\frac{dT}{dt} = \frac{Q}{C\rho(D+D_T)} = \frac{IU}{SC\rho(D+D_T)} \quad (3.1)$$

Where  $C$  is the specific heat capacity of the target,  $\rho$  is the target density, and  $S$  is the beam cross section on the target surface. The pulse energy is distributed in the target over depth  $(D+D_T)$  where  $D$  is the absorption length (electron range), and  $D_T$  is the thermal diffusion length. The number of electrons in the pulse is proportional to the total beam current,  $I$ . The average energy of each electron is directly related to the pulsed electron beam source (PEBS) voltage  $U$ . The  $I(U)$  relation characterizes a PEBS configuration (Strikovski et al., 2003).

In the plasma plume, the various particles experience significant changes in their kinetic energy, temperature, and ionization states. Plasma propagation range,  $L_o$  in Equation (3.2), is controlled by the ratio of ablated material amount ( $N_o$ ) to the gas pressure ( $P$ ).

$$L_o = \sqrt[3]{\frac{N_o}{P}} \quad (3.2)$$

The physical parameters in the plume, such as mass distribution, ion and atom velocity and the angular distribution of the plume species, play an important role in the production of thin films by PEBA. In particular, the thickness distribution and homogeneity in film deposition on a substrate is determined by the plume shape that has evolved during the expansion from the target surface to the substrate. Furthermore, film thickness distribution and homogeneity depend also on target-substrate distance and substrate size. The angular distribution ( $\varphi$ ) of the relative mass flow of the ablated material is shown in Fig. 3.3.  $\varphi$  denotes the angle with respect to the target normal. Film thickness distribution is proportional to  $\cos^{5.5}(\varphi)$  when a planar substrate is parallel to the target surface. To avoid the formation of pinholes/pits on the target surface and produce a better film thickness homogeneity, target rotation is recommended (Muller et al., 1995).

After the formation of a plasma plume, as a last step in the process, the ejected high-energy species impinge on the substrate surface. These energetic species sputter some of the surface atoms and a collision region is formed between the incident flow and the sputtered atoms. Consequently, a thermalized region is formed, which may cause the film to grow, because it serves as a source for condensation of particles. A thermal equilibrium condition can be reached, when the condensation rate is higher than the rate of particles removed by sputtering. Nucleation growth and thin films

quality are dependent on fundamental parameters such as the pulsed energy density, ionisation degree, the deposition rate, as well as the substrate material and temperature (Fotsa-Ngaffo, 2008).

PEBA represents an attractive cost-effective platform for large scale film deposition. Sharing the effectiveness ( $\text{cm}^3/\text{W}$ ) of converting the power of energy source into a volume of deposited film with PLD, PEBA has the advantage of lower cost ( $\$/\text{W}$ ) of the electron source (a factor of  $\sim 10$  at the same power), and much smaller size of the source (Muller et al., 1995).

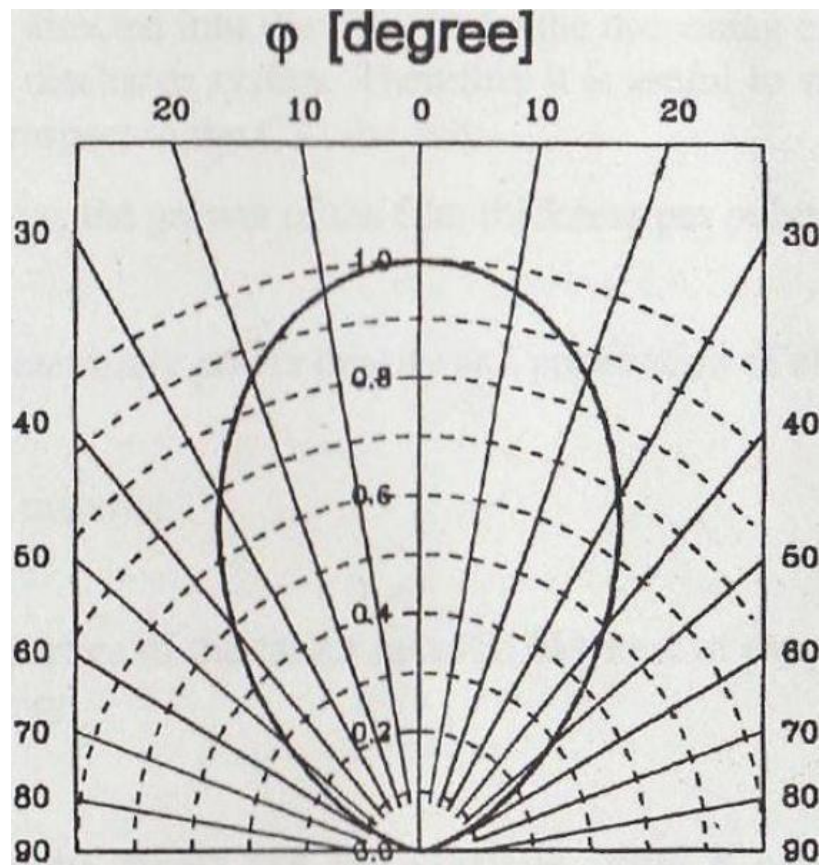


**Figure 3.3: Angular distribution of ablated material (Muller et al., 1995).**

### 3.2.2 Substrates and Equipment Preparation and Cleaning

There are two aspects of cleaning: (i) cleaning of deposition chamber, and (ii) substrates cleaning. The first is a rather obvious combination of dirt removal, degreasing, and use of solvents. The second type of cleaning is very specific to the material concerned, and to the experiment to be performed. Ideally substrates arrive from the vendor clean and free of residues and particulate

contamination. Contamination comes in the form of organic residues, and dust particles. Particulate contamination causes intimate contact problems with the resulting films and will affect potentially adhesion between the substrate surfaces and deposited films.

The substrates were first pre-cleaned sonically using Cole-Parmer 8890 ultrasonic bath, as shown in Fig. 3.4 (Dr. Henda's Lab., Laurentian University), at 50°C for one hour. However, this step, namely ultra-sonic cleaning step, has been done only on the substrates used for the first series. We did not use this step for the substrates used in the second and third series because we have noticed that the ultra-sonic cleaning would cause some turbidity for the surfaces of stainless steel substrates. Next, acetone is used as a rinsing solution for the degreasing of substrates. Finally, the substrates were rinsed in ethanol to dry. Once cleaning is finished, the substrates were immediately placed into the wafer carrier tray to minimize any surface contamination.



**Figure 3.4: Ultrasonic cleaning bath**

Before deposition, the substrates were glued (silver paint) on the substrate holder. Figure 3.5 shows four different bare substrates. Figure 3.6 shows three various substrates namely, Si(100), stainless steel, and pyrex glued on the substrate holder.

For the second and third series, before gluing the substrates to the substrate holder, they have been put in the ultrasonic bath and rinsed with acetone for 10 min followed by methanol for 10 min.

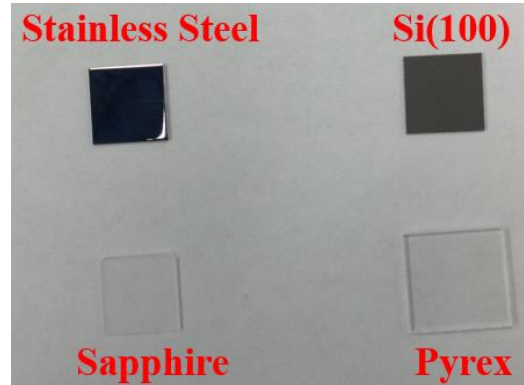


**Figure 3.5: Four different bare substrates**

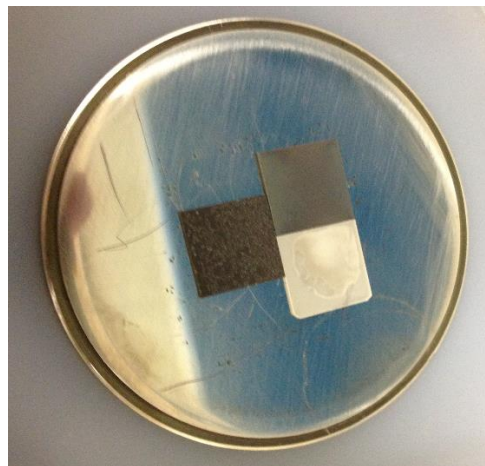


**Figure 3.6: Three various substrates glued on the substrate holder**

### 3.2.3 Process Conditions

In this work, the ablation experiments were conducted using a pulsed electron ablation system from Neocera, Inc., USA equipped with a pulsed electron beam source PEBS-20. A 25 mm diameter and 5 mm thick disk Highly Oriented Pyrolytic Graphite target (HOPG AGraphY, ZYB),

mosaic spread  $0.8^\circ \pm 0.2^\circ$ , and purity = 99.99 % (Optigraph GmbH Berlin, Germany), as shown in Fig. 3.7, was used in all series of experiments. The thin films were deposited on various substrates under different process conditions. All the specifications of the substrates that have been used in this research work are listed in Table 3.1. The details of the process conditions used in this work are listed in Table 3.2. The target has been pre-ablated by the electron beam over 3000 pulses at an angle of  $42^\circ$ , to remove potential residual oxides and other impurities on the surface.



**Figure 3.7: Highly Oriented Pyrolytic Graphite (HOPG) Target (Optigraph GmbH Berlin, Germany).**

**Table 3.1: The specifications of substrates used in all experiments**

Substrate	Specification	Source
Si(100)	Silicon Single Crystal Substrates <100> (10 x 10 x 0.5)mm, N-type, Ph doped, One side polished,  Resistivity: 1-10 Ohm-cm	Vin Karola Instruments, USA
Si(111)	Silicon Single Crystal Substrates <111>, (10 x 10 x 0.5)mm, Undoped,  One side polished  Resistivity: > 1,000 Ohm-cm	Vin Karola Instruments, USA
Pyrex	Pyrex 7740 Substrate, (12.5 x 12.5 x 1)mm, Both sides Polished	Vin Karola Instruments, USA
Corning	Corning 1737, Bare Glass Plate (12.5 x 12.5 x 0.7) mm	Vin Karola Instruments, USA
S.S.	VM-304 Stainless Steel (10 x 10 x 0.5)mm, P1S<50 ANG Valley Supplied, Polished One Side < 50 Angstroms Mirror Finish.	Valley Design Corp., USA
Sapphire	Sapphire (Al <sub>2</sub> O <sub>3</sub> ) Substrate <11-20> A-Plane, (10x 10 x 0.5)mm thick, One side Polished	Vin Karola Instruments, USA
cBN	Cubic Boron Nitride (10 x 10 x 3) mm	Henan Chinatex Company Limited, China

**Table 3.2: Process parameters of all series**

First Series					
Pulse Repetition Rate (Hz)	Number of Pulses	Background Pressure (mtorr)	Acceleration Potential (kV)	Deposition Temperature (°C)	Substrate
5	3500	4.5	14	RT	Si(100), S.S., Sapphire, Pyrex, Si(111), cBN, Corning
5	3500 and 5500	4.5	14	150 and RT	Si(100), S.S., Sapphire, Pyrex
Second Series					
8	3500	4.5	14.5, 13, 16	RT	Si(100), S.S., Sapphire, Pyrex
5	3500	4.5	14.5, 13, 16	RT	Si(100), S.S., Sapphire, Pyrex
Third Series					
8	3500	4.5	14.5	RT	Si(100), S.S., Sapphire

Target-substrate and ceramic output tube – target distances were fixed at 50 mm (see Chapter 4), and 3 mm respectively. Argon has been used as a background gas in all experiments. Target temperature has been fixed at room temperature in all experiments except in the fourth one (first series), which is 150 °C. Figure 3.8 shows four different substrates coated with NCD films.

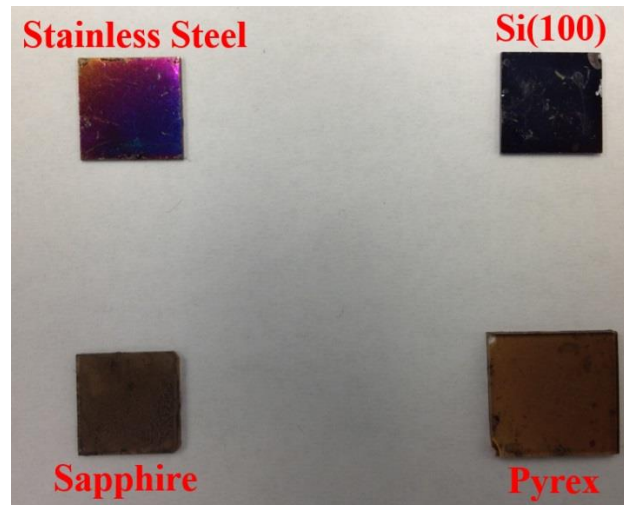


**Figure 3.8 Four different substrates coated with NCD films**

### 3.3 Heat Treatment (Pre-deposition Annealing)

Annealing is the term denoting heat treatment that consists of heating to and holding at a suitable temperature followed by cooling at an appropriate rate. Materials may be annealed to eliminate the impurities or increase the energy on the surface of substrates. Increasing the energy, in this case, is driven by stimulating the molecules on the substrate surface. Higher superficial energy is expected to improve the growth and nucleation of films (Davis, 1992).

There are three stages in the annealing process, with the first being the recovery phase, which results in softening of the material through removal of crystal defects and internal stresses they may cause. The second phase is recrystallization, where new strain-free grains nucleate and grow to replace those deformed by internal stresses. The third phase is the growth phase, where further grain growth occurs, in which the microstructure starts to coarsen. Annealing in an oxygen atmosphere would lead to the oxidation of substrate surface. Annealing under such conditions, namely, high temperature and in an oxygen atmosphere, causes solid state conversion, whereby the substrate surface is fully oxidized and surface defects are smoothed out (Wadhwa and Dhaliwal, 2008).

In this work, the heat treatment system consists of a Horizontal Split Tube (HST) furnace (Carbolite, USA) and a vacuum system as shown in Fig. 3.9. Figure 3.10 shows a simplified schematic diagram of the heat treatment system. The annealing temperature has been set to either 900 °C or 1100 °C with a ramping up/down rate of 4 °C/minute. The substrates were exposed to O<sub>2</sub> (99.999%, Praxair) for 60 min in all runs of the third series. Three substrates, viz, Si(100), S.S., and Sapphire were put on a 100 mm L x 17 mm W x 10 mm H quartz boat (MTI Corporation, USA), and laid horizontally in the center of the alumina tube (~100 mm diameter) of the furnace. The annealing process mainly consists of three steps. The first step is ramping up starting from room temperature until the set point temperature (either 900 °C or 1100 °C) followed by a dwelling step at the set point for one hour and finally ramping down from the set point until room temperature. The tube was vacuumed prior the dwelling step. Oxygen gas was fed (at a flow rate of 0.08 L/min) through the furnace tube during the dwelling step. Nitrogen gas was used for purging in order to bring the system back to atmospheric pressure.



**Figure 3.9: HST Carbolite furnace**

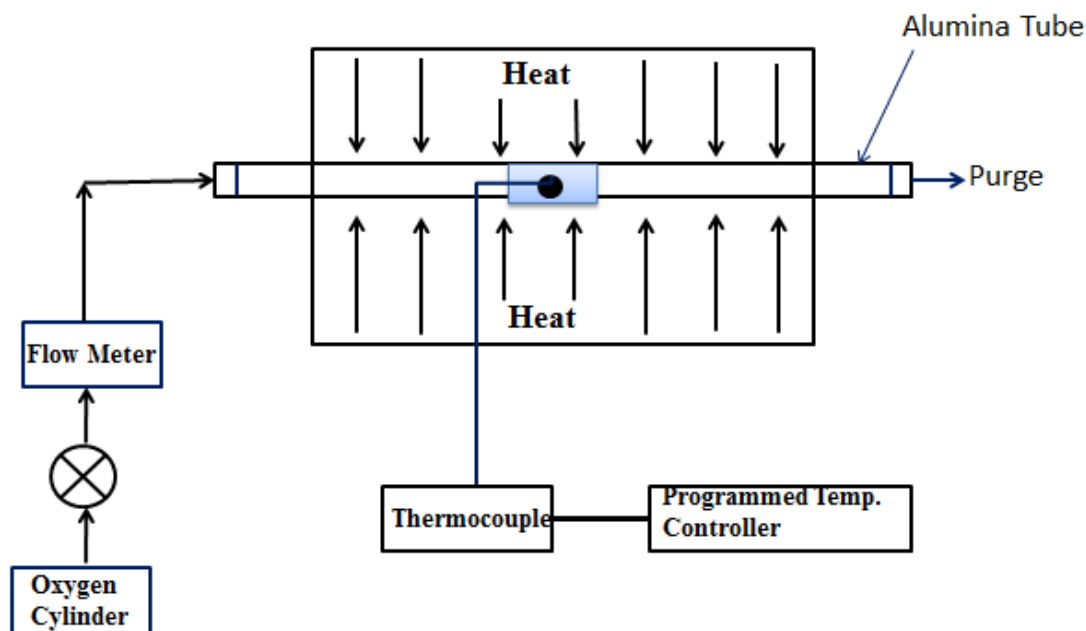


**Figure 3.10: Schematic Diagram of Heat Treatment System**

## 3.4 Characterization Techniques

The characterization of thin films is extremely important in many technologically important applications (semiconductor, micro-machining, biomedical, see Chapter 2), with parameters of interest including film thickness, refractive index, film homogeneity, hardness, composition, and smoothness of NCD coatings. In this section, the various characterization techniques used to measure these properties are briefly discussed.

### 3.4.1 Visible Reflectance Spectroscopy

Visible Reflectance Spectroscopy is a highly accurate, non-destructive, and inexpensive technique for measuring the thickness of reflecting and translucent thin films. Optical measurements are indirect because they measure the optical response of the film not the properties themselves. It could be used to measure the deposited film thickness of nanocrystalline diamond on various substrate materials such as silicon, sapphire, and glass. Figure 3.11 shows a simplified schematics of the experimental setup for measuring the thickness of a thin film. In this research work, the reflectance spectrum of NCD coatings was used to determine its thickness. Absolute reflectance spectra were acquired over the range 400–800 nm using M-Probe series reflectometer (Semiconfsoft, USA).

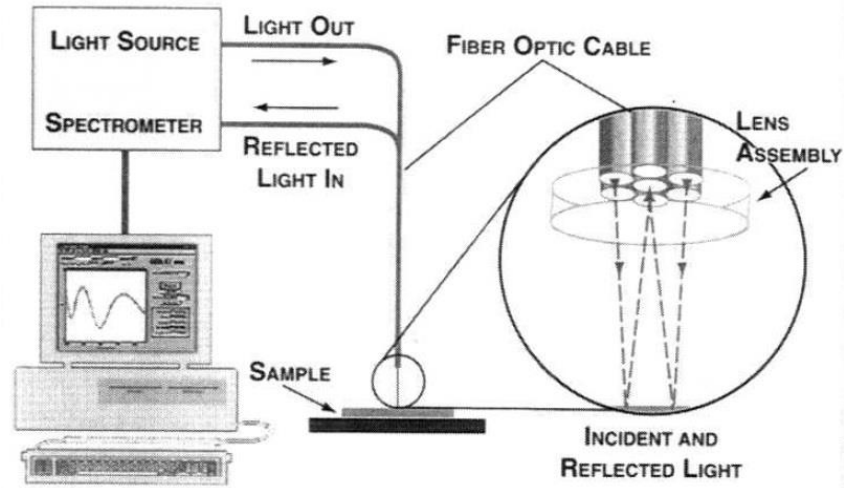


**Figure 3.11: Visible spectral reflectance system (Ohring et al., 2002).**

Interferometry is a basic optical method for determining film thickness. Incident light impinges on the film surface and a reflected portion is measured. Interferometry relies on the interference of two or more beams of light, e.g., from the air/film surface and film/substrate interfaces, where the optical path difference is related to film thickness. Light generally impinges normal to the film surface and the instrumentation differs depending on whether opaque or transparent films are involved (Peiponen et al., 2009; Ohring, 2002).

In the case of a thin film deposited on the surface of a substrate, which is made of another material, both the top and bottom surfaces of the film reflect light. The total amount of reflected light depends upon the sum of these two reflections. Moreover, these two reflections may add together constructively or destructively depending upon their phase relationship. Such phenomenon of reflection is thought to be due to the wavelike nature of light, with the phase relationship determined by the difference in optical path lengths of the two reflections. The resulting interference pattern can be used to determine the thickness of the film in question. However, the optical constants ( $n$ : refractive index and  $k$ : extinction coefficient) need to be measured first (Hind and Chomette, 2011).

To measure the thickness of a deposited thin film using the M-Probe series reflectometer (Semiconsoft, USA), reflectance data are obtained by using film-stacks. The latter is an adequate optical model of the sample of normally reflected light intensity over a broad wavelength range.

The built-in numerical scheme compares the measured and simulated data and infers the film stack parameters from the best fit. Experimental data were fitted by means of a modified Marquardt-Levenberg minimization scheme built in the accompanying software. Basically, the thickness is indirectly measured through the minimization of the difference between the measured and calculated reflectance responses of the film.

## 3.4.2 Raman Spectroscopy

### 3.4.2.1 Theory of Raman Spectroscopy

Raman spectroscopy is a powerful technique to determine the chemical and structural properties of liquids or solids by a simple non-destructive and non-contact method of measurement. It is the method of choice to characterize the structure of amorphous and crystalline carbon. It possesses several advantages over other conventional structural characterization techniques such as no sample preparation and rapid and wide measurement range ( $50 \text{ cm}^{-1}$  to  $4000 \text{ cm}^{-1}$ ). It involves illumination of the sample with monochromatic light and measurement of the light scattered by the sample. It is traditionally carried out at wavelengths in the blue-green spectral region  $\sim 488\text{--}532 \text{ nm}$  (Lewis and Edwards, 2001; Jabeen, 2009).

Raman spectroscopy is carried based on the principle of change in the polarization or electron movement in the material when a laser of a specific wavelength strikes the surface of the sample, and gains information about molecular vibrations. These vibrations can then provide information regarding the structure and symmetry of the molecule. In the case of NCD, these vibrations yield information regarding carbon bonding and hybridization namely,  $sp^3$  and  $sp^2$  hybridizations. The vibrations are inferred from the frequency of the scattered light (Lewis and Edwards, 2001). If the net exchange of energy between the photon and molecule is zero, the frequency of the scattered light is the same as the incident light, and this process is known as Rayleigh scattering, see Fig. 3.12. Conversely, light can interact with the molecule and the net exchange of energy is the energy of one molecular vibration. If the interaction causes the light photon to gain energy from the molecule, then the frequency of scattered light will be higher than that of the incident light: this process is known as Anti-Stokes Raman scattering, see Fig. 3.12.

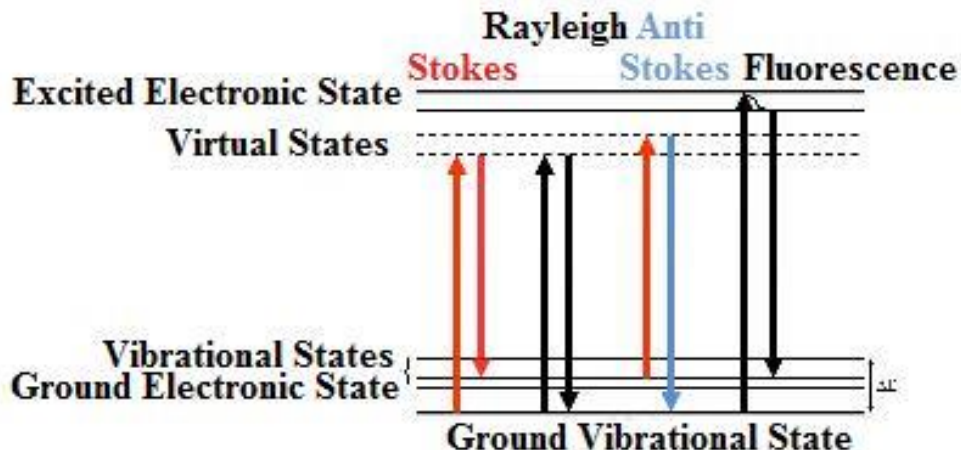


**Figure 3.12: The Jablonski diagram compares Raman, Rayleigh, and Fluorescence scattering (SERS Diagnostic Biosensor, 2012)**

On the other hand, if the interaction causes the molecule to gain energy from the photon then the frequency of the scattered light will be lower than that of the incident light, and this process is known as Stokes' Raman scattering, see Fig. 3.12. Fluorescence occurs when the atom is actually excited to another electronic state (Penney et al., 1973).

#### 3.4.2.2 Raman Instrumentation Setup

The experimental set-up used for Raman spectroscopy consists of a light source (excimer laser), the sample and the detection system for the scattered light. Lasers are intense and monochromatic light sources. They can provide a fast and easy way to record a Raman spectrum in just a few seconds (Lewis and Edwards, 2001). The typical elements of a Raman spectroscopy system for solid sample characterization are illustrated in Fig. 3.13.

The sample is illuminated by a monochromatic, highly collimated and polarized beam of light with a power of typically 1-100 mW coming from one of various types of lasers. The intensity of light has to be extremely stable as a function of time. In opaque materials, the sample surface is oriented perpendicular to the optical axis of the system. For optimal efficiency, the beam is focused to some 100  $\mu\text{m}$  diameter (at least in one direction). Even at low laser powers, of the order of 1 mW corresponding to 10  $\text{W}/\text{cm}^2$ , the spot temperature may be significantly higher than that of the sample holder (Opel and Venturini, 2002).

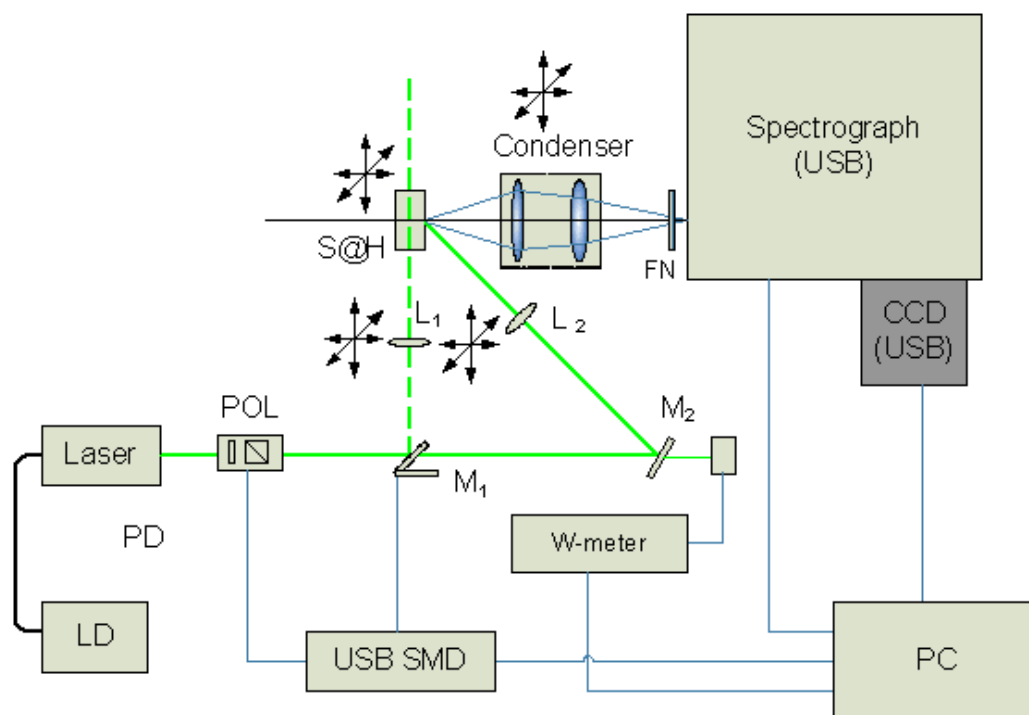


**Figure 3.13: Raman Spectrometer instrument scheme (S-RS Raman Spectrometer, 2012)**

Typical values for this laser heating effect are between 1 and 10 K/mW. The backscattered light is collected with an objective lens, as shown in Fig. 3.13, with large aperture and focused on the entrance slit of a highly dispersive and selective grating spectrometer. The selection of different polarization states of the incoming and scattered photons allows the determination of the symmetry properties of the excitations in the solid, such as the vibration pattern of phonons. After leaving the spectrometer, the photons are counted by a highly sensitive CCD camera with a quantum efficiency up to 80% in the visible range. Photon rates down to 10 per second can be measured within an exposure time of only 30 s, with an error of less than 10 % (Cazes and Ewing, 2005).

In this work, Raman data were collected in backscattered mode on a HORIBA Jobin Yvon XploRA spectrometer (Central Analytical Facility, Laurentian University) interfaced with an Olympus BX 41 microscope (100x magnification) at an estimated spot size of 2  $\mu\text{m}$ , as shown in Fig. 3.14. Raman spectra were obtained between 50  $\text{cm}^{-1}$  and 2000  $\text{cm}^{-1}$ . Raman characterization was covered only at 1200 grating and an incident laser excitation radiation wavelength of 532 nm. Calibration was carried out using the 521  $\text{cm}^{-1}$  line of a silicon wafer.

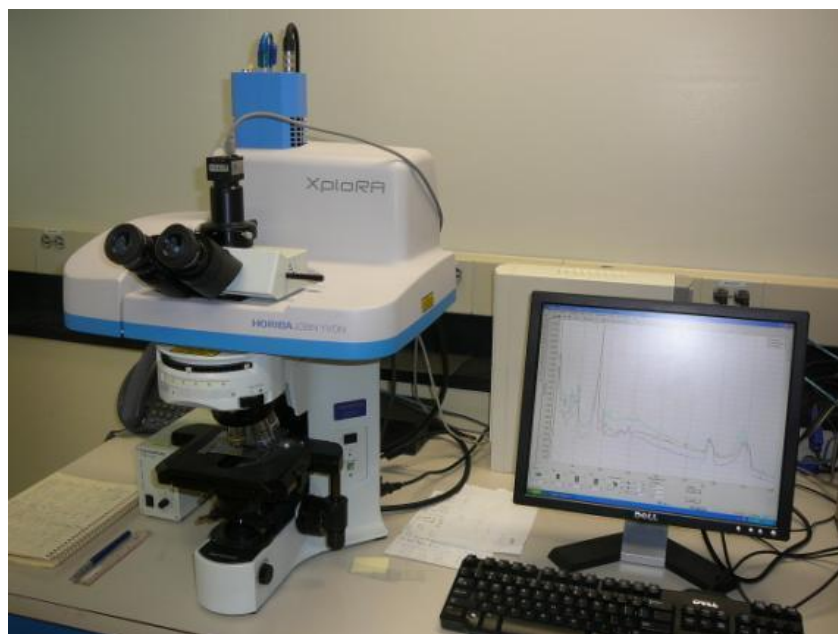


**Figure 3.14: Raman Spectrometer**

### 3.4.2.3 Raman Characterization of NCD films

Generally, all carbons show common features in their Raman spectra in the  $900\text{--}2000\text{ cm}^{-1}$  region: the G and D peaks, which lie at ca.  $1560$  and  $1360\text{ cm}^{-1}$ , respectively, are generated due to the excitation that occurs in  $sp^2$  sites. Visible Raman spectra of amorphous carbon are dominated by  $sp^2$  sites, because the excitation resonates with  $\pi$  states. The G peak is due to the bond stretching of all pairs of  $sp^2$  atoms in both rings and chains. The D peak is due to the breathing modes of  $sp^2$  atoms in rings only (Piscanec et al., 2005; Gruen, 1999; Ferrari and Robertson, 2004).

In visible Raman spectra, the cross-section of the  $sp^2$  phase is much higher (50 – 250 times) than that of the  $sp^3$  phase (Wada et al., 1980; Salis et al., 1996). Furthermore, the spectra depend directly on the configuration of the  $sp^2$  phase and only indirectly on the quantity of the  $sp^2$  phase. The  $sp^2$  configuration varies consistently with the  $sp^2$  fraction. On the other hand, the G peak full width at half maximum (FWHM) is a measure of disorder and increases continuously as the disorder increases.

Figure 3.15 shows a Raman spectrum of a typical nanocrystalline diamond. It was generated in a surface-enhanced Raman spectroscopy study by Ferrari and Robertson (2004). The spectrum has five features at  $1150$ ,  $1332$ ,  $1350$ ,  $1480$  and  $1550\text{ cm}^{-1}$ . However, these peaks are only the typical

peaks. They appear in all Raman visible spectra generated from nanocrystalline diamond. Other peaks may appear less frequently, such as the peak at  $\sim 1240\text{ cm}^{-1}$ , and two peaks within the ranges  $1550\text{-}1650$ , and  $2000\text{ - }2100\text{ cm}^{-1}$ , respectively. The peak at  $1332\text{ cm}^{-1}$  is attributed to diamond. The peak at  $1150\text{ cm}^{-1}$  has been attributed to nanocrystalline diamond (Ferrari and Robertson, 2001; Nemanich et al., 1988; Shroder et al., 1990). The peak at  $1240\text{ cm}^{-1}$  and the companion peak at  $1480\text{ cm}^{-1}$  are a signature of transpolyacetylene (Ferrari & Robertson, 2001) and have nothing to do with C–C  $\text{sp}^3$  vibrations. Transpolyacetylene,  $\text{trans}-(\text{CH})_n$ , is formed in the grain boundaries of NCD. Polyacetylene is the simplest linear conjugated polymer, i.e., a polymer with a continuous line of alternating single- and double-bonded carbon.

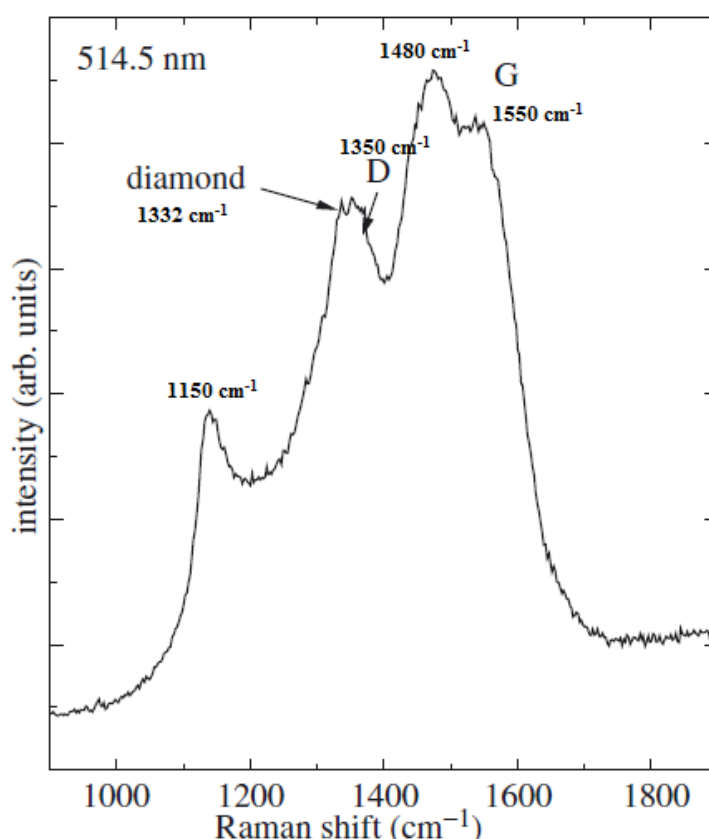


**Figure 3.15: Visible Raman spectrum of a typical nanodiamond sample (Ferrari and Robertson, 2004)**

Nanocrystalline diamond containing small-size grains is thought to show a higher intensity peak at  $1150\text{ cm}^{-1}$ . In addition to the peaks at  $1150\text{ cm}^{-1}$  and  $1480\text{ cm}^{-1}$ , NCD may show a third peak at  $1240\text{ cm}^{-1}$ . This peak is generated due to both trans-polyacetylene and the presence of the grains

of less than 1 nm in size. Sometimes the peak at  $1240\text{ cm}^{-1}$  is very hard to observe, due to its small intensity and the dominance of the D peak (Lopez-Rios et al., 1996).

There is another peak within the range  $2000 - 2100\text{ cm}^{-1}$ , which has been attributed to cumulenic chains. Such chains have a significant fraction of  $sp^1$  hybridized carbon atoms. Also, there is a saddle-shaped feature within the range  $200-900\text{ cm}^{-1}$ . It is a low-frequency feature in the spectra of a-C film samples. This feature is characteristic of the highly disordered amorphous-carbon materials. It is an important measure of the degree of disorder of a-C materials, and is related to the feature of the phonon density of the states of graphite (Wang et al., 1993; Casari et al., 2008).

In samples which consist of mixed phases of diamond and amorphous carbon, there are three types of defects:  $\pi$  pairs, strain defects, and stretched bond defects. These localized defects consist of isolated  $sp^2$  bonded pairs. Such defects interact with each other, hybridize, and have a significant spectral weight in localized states both below and above Fermi gap. The sample with a number of interacting defects rearranges itself so that some of the (occupied) defect states are pushed lower in energy and some of the (unoccupied) defect states are pushed higher in energy. The decrease in energy obtained from the lowering of the occupied eigenvalues more than compensates for any additional strain energy (Drabold et al., 1994; Praver et al., 2000). A visible Raman peak may appear within the range  $1550 - 1650\text{ cm}^{-1}$  due to these defects (Singha et al., 2006).

### 3.4.3 Scanning Electron Microscope (SEM)

Scanning Electron Microscopy (SEM) is used to study surface topology and morphology of films. SEM is an instrument that produces a largely magnified image by using electrons instead of light to form an image. A beam of electrons is produced at the top of the microscope by an electron gun. The electron beam follows a vertical path through the microscope, which is held within a vacuum, see Fig. 3.16. The beam travels through electromagnetic fields and lenses, which focus the beam down toward the sample. Once the beam hits the sample, electrons and X-rays are ejected from the sample and, various physical interactions would occur. These interactions are mainly, ionization, secondary electrons emission, backscattering electrons, X-ray emission, and cathode-luminescence phenomenon. Various detectors would collect these X-rays, backscattered electrons, and secondary electrons and convert them into a signal that is sent to a screen similar to a television display. This produces the final image. The detection of the secondary electrons would improve

significantly the final image by revealing more features and enhancing its resolution. The secondary electrons yield depends on many factors, and is generally higher for high atomic number targets, and at higher angles of incidence (Sibiya, 2007).

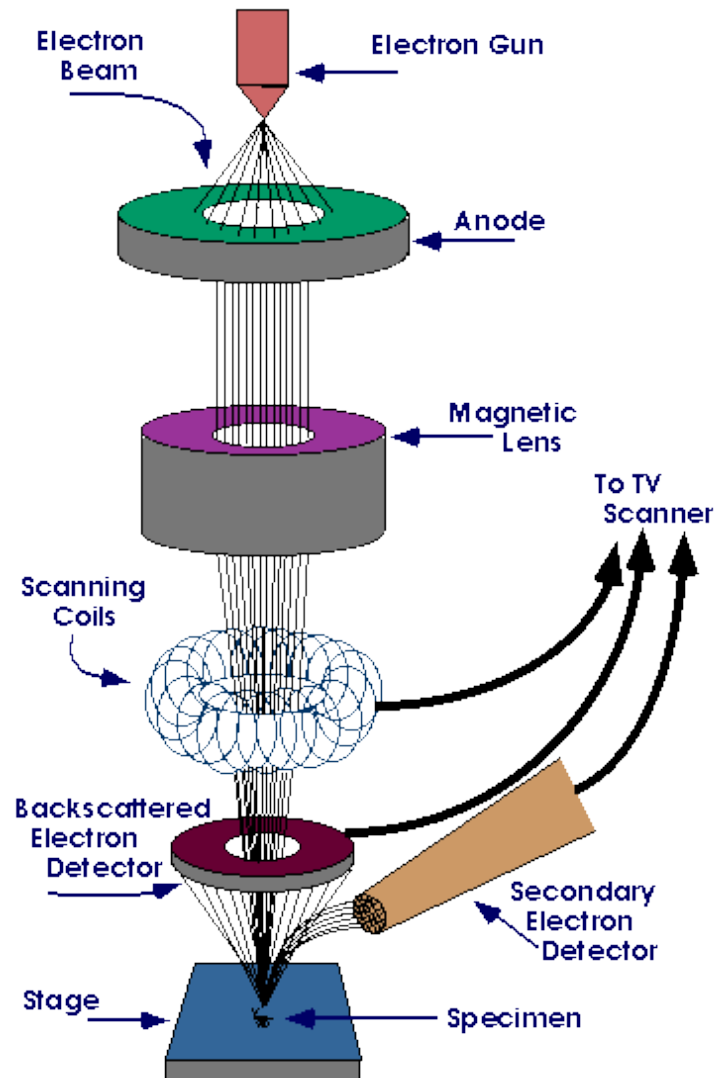


**Figure 3.16: Scanning Electron Microscope scheme** (Lyman, 1990)

Because SEM utilizes vacuum conditions and electrons to form an image, special preparations must be done to the sample. Samples have to be dehumidified properly because water would vaporize in vacuum. The conductivity of samples has to be enhanced by covering the samples with a thin layer of conductive material such as carbon. Furthermore, all samples must be vacuum compatible. The analysis takes place in a high-vacuum chamber ( $\sim 10^{-3}$  mTorr) under a range of

acceleration voltages 3 – 20 kV. Therefore, samples that are vacuum incompatible will be crushed at such pressure.

In this work, an FEI Quanta 650F (F stands for FEG or Field Emission Gun) SEM system was used to assess deposited film morphology of the samples produced from the first series (Xstrata Co., Sudbury ON). The images were taken at 20 kV and a spot size of 3.5  $\mu\text{m}$  using Everly Thornhart Secondary Electron Detector. Working distance on most images is 7 mm. However, NCD samples resulting from series 2 and 3 have been analyzed using SEM (Model Quanta 250FEG, 10 kV) at the Centre for Nanostructure Imaging/University of Toronto.

#### 3.4.4 Atomic Force Microscopy (AFM)

Atomic force microscopy (AFM) could be used to characterize films, in order to assess their topography, morphology, and surface roughness (Bao, 2000). AFM operates by measuring the force between a probe and a sample. The probe is usually a tiny and sharp tip attached to the end of a cantilever mounted on a substrate. When the probe scans over a sample, interatomic or molecular interaction forces induced between the tip and sample surface varies in accord with the surface topographical features. These forces could assume various types (such as mechanical contact force, van der Waals forces, capillary forces, chemical bonding, electrostatic forces, or magnetic forces) and may cause deflection of the cantilever, which is measured by a laser spot reflected from the top surface of the cantilever into a position-sensitive detector. The force can be determined from the deflection of the cantilever with Hook's Law. Cantilever deflections would be detected as electrical signals, which in turn can be digitized and converted to a topographical map of the tested sample surface (AFM image). The resulting lateral resolution of AFM is usually lower than the vertical resolution (Eaton and West, 2010; Tang, 2010).

In a typical AFM instrument, the AFM probe is usually installed above the piezoscanner assembly, as shown in Fig. 3.17. AFM head assembly holds the specimen and controls tip scanning, which the scanning tower design incorporates three elements: Laser, mirror assembly and photodetector. These elements maintain the same relative position throughout the scanning motion. A computer communicates between an operator and AFM through a control box. An optical microscope is used to obtain a magnified view when handling small tips. The entire AFM apparatus has to be installed on an anti-vibration table. The probe can move laterally and vertically. Its lateral movement is

generated by the x and y piezoceramics, which is positioned towards the top of the scanning tower, and its vertical movement is generated by the z-piezoceramic, which is installed on the base of the scanning tower.

AFM can work in three different modes: Contact mode, non-contact mode, and tapping mode. The most widely used mode is contact mode. It is commonly used for rigid surfaces. As per the contact mode, the probe scans at a constant force within a distance very close to the sample surface. When the probe cantilever is deflected by topographical changes, the scanner adjusts the probe position to restore the original cantilever deflection. The scanner position information is collected as data to create a topographical image. The second mode, non-contact mode, is usually used to image soft samples. In non-contact mode, the tip interacts with the surface via van der Waals force or any other long range force which extends well above the surface. The third mode, tapping mode, can produce higher lateral resolution compared to the other modes. In this mode, the probe tip is scanned at a height where it barely touches or “taps” the sample surface (Bowen and Hilal, 2009; Tang, 2010).

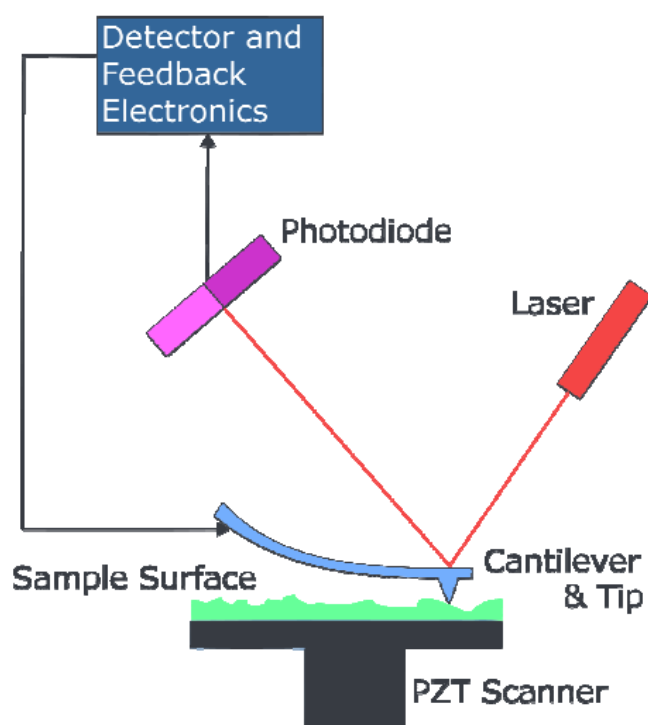


**Figure 3.17: Schematic of AFM instrument (Tang, 2010)**

In this work, the morphology and topography of the films have been characterized using AFM (Bruker Multimode, contact mode, probes: Bruker Tespa, 0.5 Hz, 25 N/m), shown in Fig. 3.18, (Dr. Shepherd's Lab., Laurentian University).



**Figure 3.18: Bruker Multimode AFM IIIA**

### 3.4.5 X-Ray Diffraction (XRD)

The crystalline nature and crystal type of films can be identified from their XRD patterns. Single-crystal X-ray Diffraction is a non-destructive analytical technique, which provides detailed information about the internal lattice of crystalline substances, including unit cell dimensions, bond-lengths, bond-angles, and details of site-ordering. X-rays are electromagnetic waves with wavelengths in the range of 0.01 to 10 nanometers and energies in the range of 100 eV to 100 keV. For diffraction applications, only X-rays of wavelength comparable to the size of atoms are able to probe the structural arrangement of atoms and molecules in a wide range of materials. The energetic X-rays can penetrate deep into the material and provide information about the bulk structure (Saravanan and Rani, 2012).

X-rays are produced mainly by X-ray tubes, which are generated when a focused electron beam accelerated across a high voltage field bombards a stationary or rotating solid target. As electrons collide with atoms in the target and slow down, a continuous spectrum of X-rays is emitted, which is termed Bremsstrahlung radiation. The high energy electrons also eject inner shell electrons in atoms through the ionisation process. When a free electron fills the shell, X-ray with energy characteristic of the target material is emitted (Nazarov and Noh, 2011). X-rays primarily interact with electrons in atoms. When X-ray photons collide with electrons, some photons from the incident beam deflect away from their original direction of travel. If the wavelength of these scattered X-rays does not change during this process, this is called elastic scattering. In this kind of scattering (elastic) only momentum is transferred in the elastic scattering process, but not energy. These are the X-rays that are measured in diffraction experiments, as the scattered X-rays carry information about electron distribution in materials. On the other hand, in the inelastic scattering process (Compton scattering), X-rays transfer some of their energy to the electrons and the scattered X-rays will have different wavelength than the incident X-rays (Moore, 2008). Incoming waves reflecting from the first crystal plane will interfere with waves reflecting from the second (and subsequent) crystal planes forming an interference pattern. This interference is termed Bragg diffraction. For constructive interference, the path length difference between the two reflected beams must differ by an integer multiple of a complete wavelength. As shown in Fig. 3.19, the wave reflecting from the second crystal plane travels an additional distance of  $2d\sin\theta$  (Moore, 2008). Thus, the relation, Equation (3.3), for constructive interference is:

$$n.\lambda = 2.d.\sin(\theta) \quad (3.3)$$

Where  $n$  is the order of diffraction

$\lambda$  represents the wavelength of X-ray

$d$  is the inter-planar spacing and

$\theta$  signifies the X-ray scattering angle

The diffracted X-rays are then detected, processed and counted. Identification of the composition can be achieved by comparison of  $d$  spacing or  $2\theta$  peaks with standard reference patterns. If the atoms are arranged in a periodic fashion, as in crystals of diamond, the diffracted waves will

consist of sharp interference peaks (maxima) with the same symmetry as in the distribution of atoms.

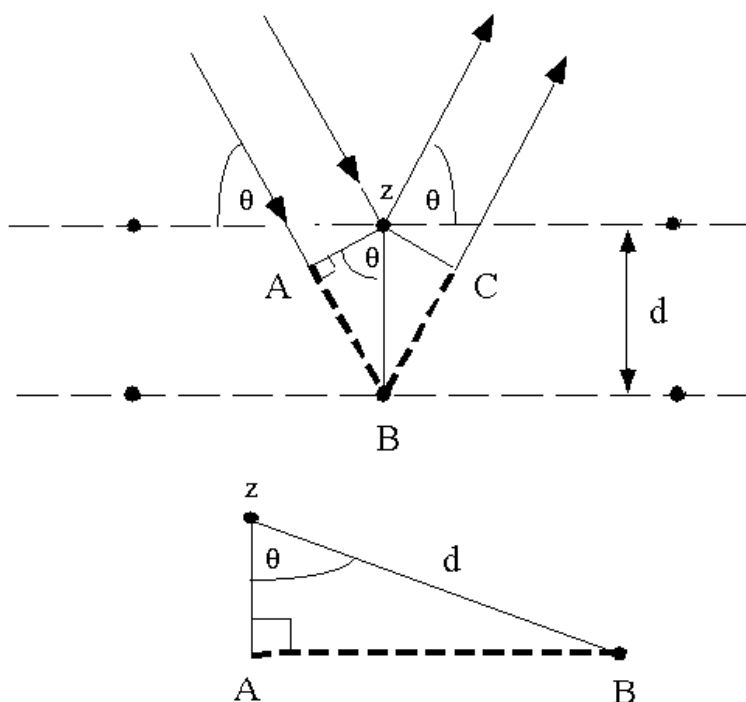


**Figure 3.19: Bragg's law and diffracted X-rays (Lyman, 1990)**

However, in amorphous carbon, the diffracted waves will not produce sharp interference peaks. Diamond could be identified based on the positions and intensities of peaks. Measuring the diffraction pattern may help in deducing the distribution of atoms in the material (Saravanan and Rani, 2012).

Grazing angle X-ray diffraction (GAXRD) has been used in this work. In GAXRD, small incident angles are used for the incoming X-ray. It is used to study surfaces and layers where wave penetration is limited. The advantage of using this geometry is increased x-ray path-length in the film and reduced substrate signal.

In this work, NCD films on Si(100) and Pyrex, resulting from series 2, at 8 Hz and 14.5 kV and 16 kV, were run on Bruker AXS D8 Discovery Microdiffraction system (available at Department of Chemistry, University of Toronto) with Cu  $\alpha$  point-focus x-ray source operating at 40 kV/40 mA. The system is equipped with curved primary graphite monochromator and 2D proportional

detector (GADDS). The experimental data were collected on two frames at 480 s exposure of each one that cover the range of  $20^\circ - 65^\circ - 80^\circ$  ( $2\theta$ ). The 2D diffraction images were then integrated with a step size of  $0.005^\circ$   $2\theta$  and converted to standard I vs.  $2\theta$  diffraction patterns. Grazing angle geometry was applied with  $\theta = 2^\circ$  on all samples.

### 3.4.6 Nano-Indentation

Nanoindentation is a common method used to measure the elastic modulus and hardness of thin films on substrates. The nanoindenter has to have a high load resolution and depth resolution, which make it possible to obtain accurate measurements on small samples (e.g., precipitates and particles in a matrix) and thin films. A schematic diagram of a nanoindentation system is shown in Fig. 3.20. A nanoindenter continuously measures the load and displacement of a three-sided pyramidal diamond indenter as it is pushed into the sample. There are different types of tips commonly used, each of which has a corresponding angle of incidence and sharpness. The different tip shapes used for nanoindentation are conical, the Berkovich, Vickers, spherical, and cube corner tips (Fischer-Cripps, 2004).

The hardness values of NCD films, prepared using CVD methods in the range of few micrometers, have been reported in the literature in the range of 10 – 100 GPa (Tse et al., 2006; Catledge et al., 2002). The hardness “H” is determined from the values given by the force/indentation depth curve during the loading of the test force, preferably after reaching the specified test force.

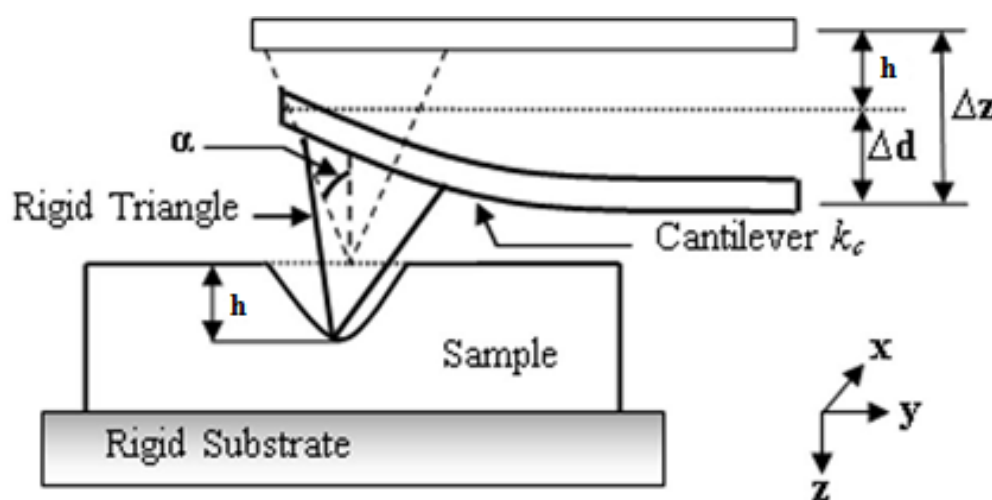


**Figure 3.20: Schematic diagram of a nanoindentation system**

During this load-unload cycle the load “P” and the displacement “h” are measured. The hardness H can be calculated using Equation (3.4) (Fischer-Cripps, 2000):

$$H = P_{\max} / A_c \quad (3.4)$$

Where  $P_{\max}$  is the maximum applied load and  $A_c$  is the contact area of the tip on the surface of the material, see Fig. 3.21.

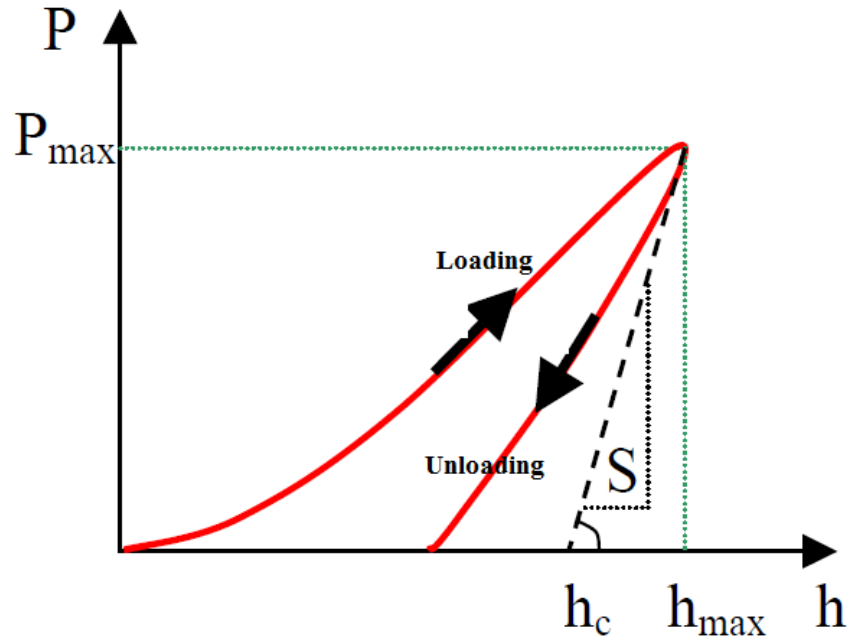


**Figure 3.21: Load P versus displacement h curve (Fischer-Cripps, 2000)**

The contact area can be calculated based on the contact depth  $h_c$  using Equation (3.5) for Vickers tip.

$$A_c = 26.43 \times h_c^2 \quad (3.5)$$

When the load is removed from the indenter, the material attempts to regain its original shape, but it is prevented from doing so because of plastic deformation. However, there is some degree of recovery due to the relaxation of elastic strains within the material. An analysis of the initial portion of this elastic unloading response gives an estimate of the elastic modulus of the indented material. Elastic modulus “E” is calculated based on the Sneddon equation (Fischer-Cripps, 2000; Frontini and Fasce, 2011), Equation (3.6), and Equation (3.7):

$$E^* = \frac{\sqrt{\pi} \cdot S}{2\beta \sqrt{A_c}} \quad (3.6)$$

Where  $E^*$  is the composite elastic's modulus depending on both the elastic modulus and Poisson's ratio of test material and of tip material,  $S$  is the contact stiffness and  $\beta$  a correction coefficient near to 1.  $\beta$  is 1.034 for Vickers tip used in this work, and  $\nu$  is Poisson's ratio (Fischer-Cripps, 2000).

Based on the results obtained for  $E^*$ , the elastic modulus of the test material "E" can be calculated, where "i" is the subscript for the properties of the indenter:

$$\frac{1}{E^*} = \frac{1-\nu^2}{E} + \frac{1-\nu_i^2}{E_i} \quad (3.7)$$

In this work, Martens hardness (HMT115) of the films has been measured using Shimadzu Ultra Micro Hardness Tester (Vickers Tip) (Dr. Jamal Deen's Lab, McMaster University). Two sets of experiments have been done: (1) load-unload test and (2) depth setting load-unload test.

## **Chapter 4: Calculation of Temperature and Pressure of Carbon Ions on Impact**

## 4.1 Introduction

Most natural diamonds are formed at high temperature and pressure at a depth of a few hundred kilometers in the Earth's mantle. Carbon-containing materials provide the carbon source, and diamond growth occurs over periods of a few billion years. Diamonds are brought close to the Earth's surface through deep volcanic eruptions by a magma.

Many attempts have been made to synthesize diamond by trying to mimic nature. One early and tangible effort is due to Hershey, in the late 1920s. He was able to create synthetic diamonds from the freezing of sugar carbon dissolved in molten iron. A few decades later, several attempts have ensued to synthesize diamond. In 1953, Baltzar von Platen and Anders Kampe (Sweden) used high-pressure and high-temperature conditions to synthesize commercial diamond (Liander, 1955). A year later, Tracy Hall and coworkers (1955) of General Electric managed to synthesize diamond using a similar method.

In the early 1960s, diamond films were produced by the pyrolysis of methane over a diamond substrate (Eversole and Angus, 1962). Low-pressure synthesis of diamond from hydrocarbon gas mixtures by Deryagin and Fedoseev, in the 1970s, can be regarded as one of the earliest attempts to produce synthetic diamond coatings. Ever since, the growth of diamond films has attracted intensive worldwide attention by the research community, as high-quality films exhibit most of the unsurpassed properties of natural diamond and are much more cost effective.

In this chapter, some aspects of the dynamics of the plasma arising from the ablation of an HOPG target using PEBA are discussed according to two models, namely, Strikovski's model (Strikoviski et al., 2010), and the shock wave model (Anisimov et al., 1996). Expansion of the pulsed electron beam induced plasma will be discussed for the two cases of vacuum and ambient gas conditions in order to estimate the temperature and pressure of carbon ions on impact on the substrate in both cases. The estimated temperature and pressure of carbon ions on impact will be compared with the carbon phase diagram in order to predict the resulting phase under specific film deposition conditions. Such conditions include accelerating voltage, background pressure, and target-substrate distance. The aim of this chapter is to shed light on critical process parameters and guide in our efforts to design a rational experimental plan.

## 4.2 Carbon Phase Diagram

The equation of graphite-to-diamond phase boundary was determined by Berman (1994) based on extensive thermodynamic data. The latter includes the heat of formation of diamond, heat capacity of graphite as a function of temperature, and the atomic volume and coefficient of thermal expansion of diamond. Berman's equation takes the following form:

$$P(\text{kbar}) = 12 + 0.0301 \times T(^{\circ}\text{C}) \quad (4.1)$$

P is the applied pressure, and T is the temperature. Although Equation (4.1) is thermodynamically feasible at relatively low pressure and temperature, the transformation of diamond to graphite faces a considerable kinetic barrier since the rate of transformation apparently decreases with increasing pressure. Experiments show that high pressures retard the rate of transformation of diamond to graphite, as per Equation (4.2). The theory of absolute reaction rates (mol/s) indicates for such a situation that (Hall, 1961):

$$\text{Log}(\text{rate}) = \text{constant} - (\Delta V \cdot P / R \cdot T) \quad (4.2)$$

$\Delta V$  is the molar difference in volume ( $\text{m}^3$ ) between diamond and the activated complex (the intermediate state or transition state), P is the applied pressure (bar), T is the temperature (K), and R is the molar gas constant ( $\text{m}^3 \text{ bar K}^{-1} \text{ mol}^{-1}$ ). This kinetic consideration supersedes the favorable thermodynamic conditions, i.e., the pressures and temperatures to which graphite has been subjected. It was found experimentally that very high pressure and temperature (>130 kbar and ~3300 K) were necessary in order for the direct graphite-diamond transformation to proceed at any observable rate. These conditions are very difficult and costly to achieve, although, it is possible to bypass this kinetic barrier by the solvent-catalyst reaction method (Pierson, 1993).

The transformation from graphite to diamond, using many CVD or PVD techniques, is considerably slow. However, this transformation can occur more rapidly when carbon atoms are exposed to extremely high temperature and pressure using more effective deposition methods such as PEBA. In PEBA, once a pulsed electron beam strikes the target surface, the pulsed electrons energy is transformed into heat as mentioned in Chapter 1 (Muller et al., 1995). The temperature of the solid material (HOPG target, in this case) will increase, leading to melting and evaporation

of the target material. The interactions between the vapor plume and the background result in gas confinement of the plume, whereas the background gas is pushed further away from the solid target. Because the temperature in the vapor plume can rise to high values (10 000 K and higher), a plasma will be formed. The vapor plume may consist of various ablated particles such as neutral carbon atoms and carbon ions, as is the case of HOPG ablation. The ablated particles bombard the substrate at high energy causing local heating on impact. The subsequent local heating of target may also produce compressive strain and lead to a shock wave expanding into the substrate. The compressed and heated material expands and cools to equilibrium within the substrate lattice towards the end of the electron beam pulse (Strikovski et al., 2010; Anisimov et al., 1996).

The energy of carbon ions on impact will determine the carbon phase of the films on the substrate surface, as shown in the carbon phase diagram in Fig. 4.1. High energy carbon ions may end up in the diamond phase upon cooling and condensation, while low energy ions may end up in the graphite phase. As an obvious condition for diamond formation, the temperature has to fall rather rapidly as compared to the pressure decay. The energy of carbon ions in the plasma is critically controlled by the power density of pulsed electron beams (as explained in section 4.3), which is dependent on other process conditions of PEBA.

### 4.3 Strikovski's Model

During the process of NCD films deposition via PEBA, carbon atoms ablated from the surface of HOPG target pass through several energy transformation phases before arriving at the substrate surface. Starting from their evaporation, the atoms are involved in a series of energy transfer processes controlled by different mechanisms. These atoms experience significant changes in their temperature, ionization state, as well as kinetic energy (Strikovski et al., 2010).

The dominant process during target ablation is the evaporation and ionization of a small amount of material. At high beam power density, the target surface is rapidly heated, attaining temperatures well above the common evaporation temperature of carbon in the target, and effectively transforms into a plasma state.

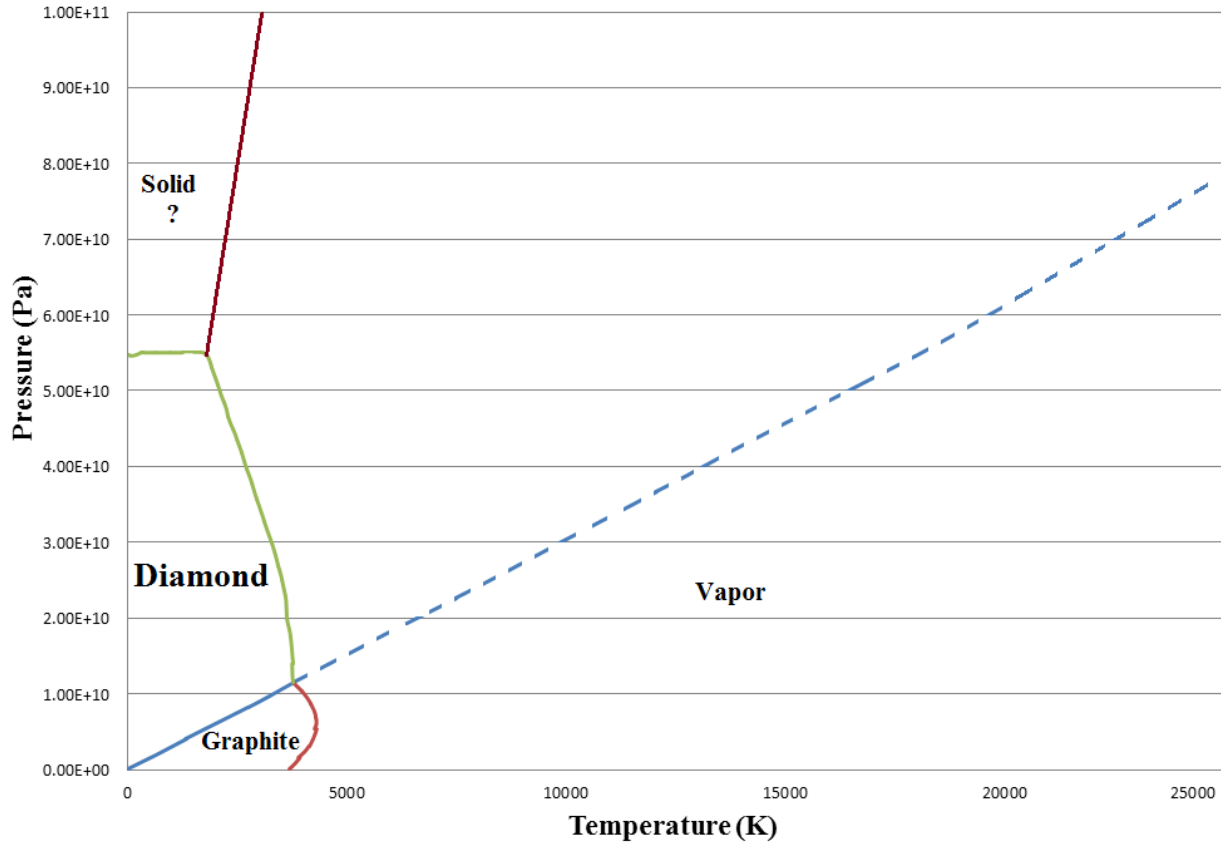


**Figure 4.1: Carbon phase diagram. Stability regions of crystalline diamond and graphite in the pressure-temperature diagram (Bundy, 1980).**

Several key parameters that control the process of ablation are pulse duration  $\tau$  (s), power density  $Q$  ( $\text{W}/\text{cm}^2$ ), accelerating voltage (kV), background gas, and background gas pressure (Pa). The fifth parameter is the energy of electron (keV) that defines the absorption depth of the beam with respect to the target material. The rate of surface temperature rise ( $dT/dt$ ) can be expressed from energy conservation considerations as:

$$\frac{dT}{dt} = \frac{Q}{C\rho S(D+D_T)}, \quad (4.3)$$

where  $C$  is the specific heat capacity of the target (HOPG),  $0.71 \text{ J/g}\cdot\text{K}$ ,  $\rho$  is the target density,  $2.27 \text{ g}/\text{cm}^3$ ,  $t$  is time, and  $S$  is the beam cross section on the target surface,  $\sim 0.05 \text{ cm}^2$ . The pulse energy

is distributed in the target over a depth ( $D + D_T$ ), where  $D$  is the absorption length (electron range) and  $D_T$  is the thermal diffusion length. Temperature can be integrated from room temperature, 298 K, to the temperature of ablation. Time is integrated to the pulse duration of 100 ns.

The penetration depth, or absorption range, of an electron in a solid depends on its energy. In PEBA, both the electron beam power  $Q$  and the electron range depend on the electron source voltage  $U$ . The number of electrons in the pulse is proportional to the total beam current density, and the average energy of each electron is directly related to the pulsed electron beam source (PEBS) voltage. Therefore, the power density carried by the beam is  $Q \approx IU$ , where the current is denoted by  $I$  and given in Ampere (A). The accelerating voltage is given in kilovolt (kV). The current is a function of the accelerating voltage, and the current-voltage relationship characterizes a PEBS design. For 10 – 100 kV electrons, the electron range changes with voltage as  $D \propto U^2$ . If  $D > D_T$ , the  $D(U)$  dependence controls the denominator in Equation (4.3), and thus strongly affects the heating rate in PEBA. The interplay between  $Q(U)$  and  $D(U)$  controls the surface heating rate in PEBA (Strikovski and Harshavardhan, 2003). Under such conditions, the beam power is not able to increase as fast as the beam penetration length at accelerating voltages higher than 14.5 kV, which leads to a maximum in the heating rate at  $\approx 14.5$  kV, as shown in Fig. 4.2. The temperature of ablated carbon particles at ablation spot are calculated using Equation (4.3) and listed in Table 4.1, as  $T_{\text{Ablation}}$  (K).

In PEBA, the background gas may affect the average energy of the particles arriving at the substrate and the general attributes of the energy spectrum. Introduction of various background gases into the deposition chamber is necessary, because, in vacuum, the pulsed electron beams can neither be produced nor transported. The main obstacle is obviously the mutual space-charge repulsion among the electrons. In a gas medium at low pressure, however, the electron space-charge can be neutralized (Ozur et al., 2006). The Plasma flux parameters change drastically with the distance  $L$  (or plume range) from the target, which is critical for film growth. At a specific distance, the flux loses its unidirectional velocity, as it undergoes scattering, thermalization, and finally deceleration. The optimum conditions for film growth exist in the vicinity of this distance.

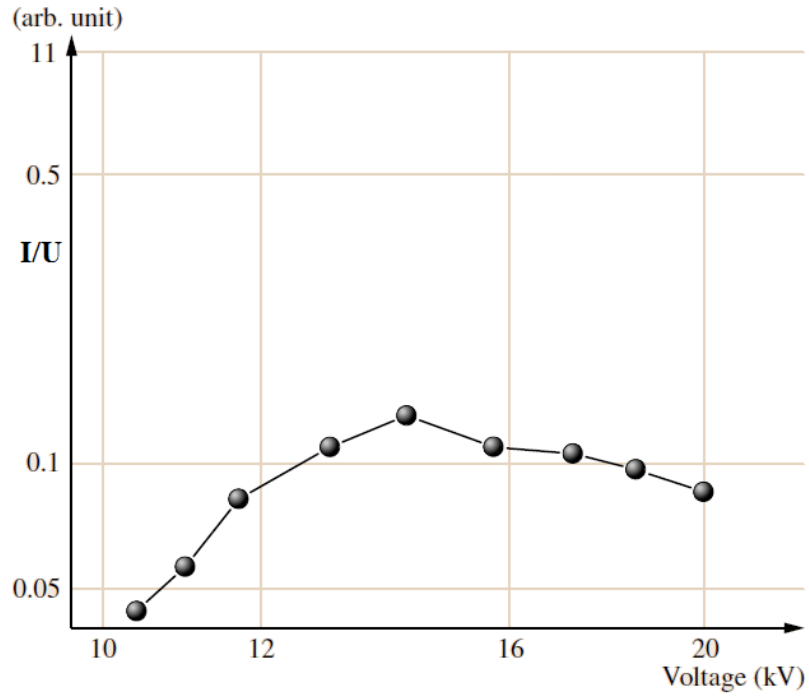


**Figure 4.2:** Estimated current/voltage ( $I/U$ ) as a function of the electron energy (Strikovski et al., 2010).

**Table 4.1:** Temperature and pressure of ions on impact at different accelerating voltage.

U(kV)	Log(I/U)	I/U (A/kV)	$T_{\text{Ablation}}$ (K)	$V_o$ (m/s)	T on Impact (K)	P on Impact (GPa)
10	0.044	1.107	92876	8170	12921	30.5
12	0.110	1.288	107948	8808	15018	35.4
14	0.130	1.349	113119	9017	15738	37.1
16	0.110	1.288	107948	8808	15018	35.4
18	0.097	1.251	104876	8682	14591	34.4
20	0.085	1.217	102067	8565	14200	33.5

Strikovski and coworkers (2010) have suggested a simple model according to macroscopic conservation of momentum and energy for an adiabatic process (Strikovski and Miller, 1998). The goal of the model is to obtain a physical definition of the plasma "range," which is an important parameter of PEBA process. The conservation equations can be written as:

$$M.N_o.V_o = (M.N_o + m.N).V \quad (4.4)$$

$$M.N_o.V_o^2 = (M.N_o + m.N)V^2 + (N_o + N).3.k.T \quad (4.5)$$

Here,  $V$  is the velocity of ions at any height,  $V_o$  is the initial velocity (Equation 4.6) of the atoms of atomic mass  $M$ , and  $N_o$  is the number of atoms within a cone whose angle is conveniently chosen such that its volume is  $L^3/3$ . The ensemble of  $N_o$  atoms is considered as a piston grabbing, incorporating and driving the gas atoms as it propagates towards the substrate. The essential processes here are energy transfer from the initial kinetic energy of  $N_o$  atoms to the gas (i.e., deceleration of the ensemble) and thermalization of the atom and gas cloud.  $N = n_g(L^3/3)$  is the number of the gas atoms (molecules) of mass  $m$  grabbed by the flux over the distance  $L$ .  $T$  is the temperature at ablation spot (K), and  $m$  is the mass of gas atom (kg).

$$V_o = \left(\frac{kT}{M}\right)^{1/2}, \quad (4.6)$$

$M$ : Mass of carbon atom =  $19.2 \times 10^{-27}$  kg

$k$ : Boltzmann constant =  $1.38 \times 10^{-27}$  J/K

Strikovski's model could be further simplified into six equations, namely, Equations (4.7) – (4.12), to describe the dynamics of plasma deceleration (Strikovski et al., 2010).

$$\frac{3kT_{impact}}{MV_o^2} = \frac{x^3}{(1+x^3)(1+\mu x^3)}, \quad (4.7)$$

$T_{impact}$ : Ions temperature on impact (K)

$x = (L/R)$  normalized distance

$L$ : plume range (cm)

Where  $\mu = M/m$  is the atomic mass ratio between the target material and the gas, and it is taken as  $(12/40) = 0.3$ , in the case of HOPG and argon.  $R$  has a clear physical meaning: after the ensemble covers the distance  $R$ , the total mass of the gas atoms becomes equal to the mass of ejected  $N_o$  atoms.  $R$  is calculated as 4.4 cm, based on:

$$R = \left( \frac{3\mu N_o}{n_g} \right)^{1/3}, \quad (4.8)$$

$$N_o = (h)(n_L)(d^2), \quad (4.9)$$

$$n_g = (P_g/kT), \quad (4.10)$$

$n_g$  = Background gas concentration (atoms/cm<sup>3</sup>)

$h$  = Deposition rate per pulse (assumed typically around 0.1 nm/pulse) (Strikoviski et al., 2010)

$n_L = 5 \times 10^{22}$  (molecule/cm<sup>3</sup>) (for most solid) (Strikoviski et al., 2010)

$d$  = Target-substrate distance (it is taken as either 5 cm or 7 cm)

$N_o$  = Propagation of an ensemble of atoms (ions) (atoms/cm<sup>3</sup>) (Strikoviski et al., 2010)

$P_g$  = Pressure of background gas (Pa). It is taken as 4 mtorr, or 0.533 Pa.

The distance  $L_o$  is the range of the plasma flux defined according to the condition  $V(L) = V_T(L)$ , where  $V$  is the velocity of the directed movement of the ensemble (kinetic energy), and  $V_T$  is the characteristic thermal velocity. Therefore, solving Equations (4.11) and (4.12) for  $x$ , would result in  $x = 1.2$ .

$$\frac{V}{V_o} = (1 + x^3)^{-1}, \quad (4.11)$$

$$\frac{V_T}{V_o} = x^{3/2} [3(1 + x^3)(1 + \mu x^3)]^{-1/2}, \quad (4.12)$$

The assessment of the pressure that exists on impact is rather difficult to perform as the aggregate state of the material is not known at this instant. In view of our rather rough procedure, we consider it sufficient to apply the ideal gas law, i.e., Equation (4.13) (Christiansen et al., 1996).

$$P = \left( \frac{N_A \rho}{m_M} \right) \left( \frac{3}{2} \right) (KT), \quad (4.13)$$

The following calculations have been conducted to estimate the temperature and pressure of ablated carbon ions at the moment when they strike the substrate surface.

In this section, the temperature at the ablation spot and temperature and pressure of ions on impact have been calculated using Equations (4.6 – 4.13), at various accelerating voltages, namely, 10 kV, 12 kV, 14 kV, 16 kV, 18 kV, and 20 kV.  $I/U$  (A/kV), of pulsed electron beam at these accelerating voltages could be obtained from Fig. 4.2. Ablation temperatures have been calculated using  $I/U$  values, as per Table 4.1.

Apparently, according to Strikovski's model, ablation of HOPG target at room temperature, argon background pressure of  $\sim 4$  mTorr, substrate-target distance of 5 cm, 100 nm pulse width, and aforementioned accelerating voltage values may result in producing and depositing a phase of metastable diamond, as discussed in section 4.5.

## 4.4 Shock Wave Model

### 4.4.1 Plasma Expansion in Vacuum

If the plume expansion takes place in vacuum, in the absence of atomic collision effects, the shape and velocity distribution in the plume will reach asymptotically constant values. The electron beam energy is rapidly converted into kinetic energy with plasma attaining extremely high expansion velocities (Kumar et al., 2010).

Physically, the pressure gradient within the plasma drives its expansion. The plasma, as it absorbs the pulse electron energy, can be simulated as a high temperature-high pressure gas, which is initially confined in small dimensions and is suddenly allowed to expand in vacuum. Because of the large pressure gradients initially present near the outer edge of the ablation spot, very high expansion velocities are induced at the edges of initial plume.

The model of Anisimov et al. (1996) is adopted here in order to model plasmas generated by pulsed electron beams in vacuum. This model is applicable for the expansion, the isentropic, adiabatic, and ionized plumes in vacuum. It was first applied to pulsed laser plasmas. The model is being used here to estimate the temperature and pressure of ions on impact during pulsed electron beam ablation. The model treats the adiabatic expansion of a one-component vapor cloud into vacuum using a particular solution of the gas-dynamic equations. The model applies to flows that are self-similar. It is assumed that the formation time of the vapor cloud is much less than its expansion time and that the focal spot of the pulsed electron beam has an elliptical shape with semi-axes  $X_0$  and  $Y_0$ , as shown in Fig. 4.3. The expansion is modeled as a triaxial gaseous semiellipsoid whose semi-axes are initially equal to  $X_0$ ,  $Y_0$ , and  $Z_0 \approx c_s \cdot \tau_p$ , where  $\tau_p$  is the duration of the pulse electron and  $c_s$  is the speed of sound in the vaporized material and given by  $c_s = [\gamma(\gamma-1)\epsilon]^{1/2}$ . According to this model, the temperature and pressure of ions on impact on the substrate under vacuum conditions can be calculated using Equations (4.14 - 4.16) (Anisimov et al., 1996).

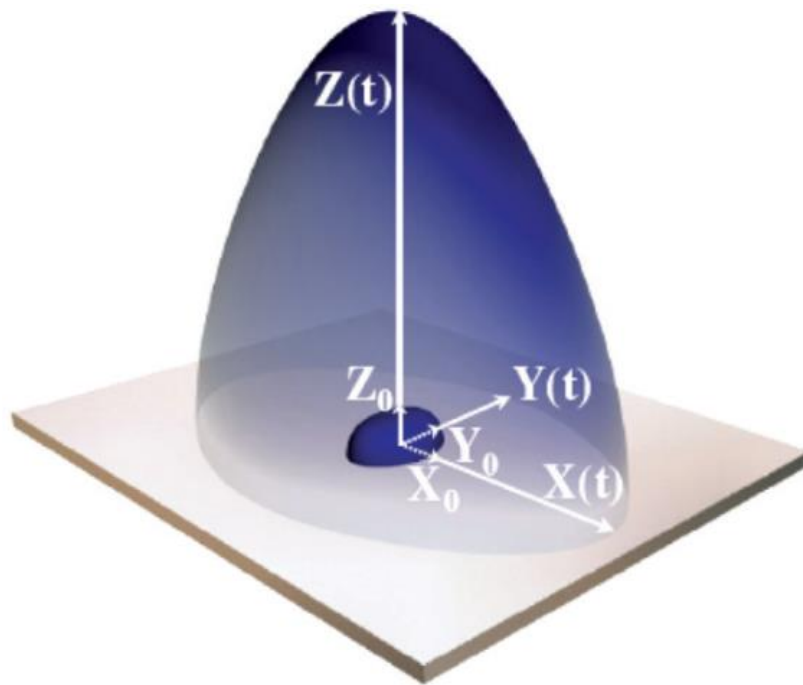


**Figure 4.3:** Diagram showing the plume at the end of the pulse when the dimensions are  $X_0$ ,  $Y_0$ , and  $Z_0$ , and after a time  $t$  when the dimensions are  $X(t)$ ,  $Y(t)$ ,  $Z(t)$  (Doggett and Lunny, 2011).

$$T = \left( \frac{\varepsilon(5\gamma-3)(\gamma-1)}{2\gamma} \right) \left( \frac{X_o Y_o Z_o}{XYZ} \right)^{\gamma-1} \left[ 1 - \left( \frac{z}{Z} \right)^2 \right], \quad (4.14)$$

$$P = \left( \frac{E_p}{I_2(\gamma)XYZ} \right) \left( \frac{X_o Y_o Z_o}{XYZ} \right)^{\gamma-1} \left[ 1 - \left( \frac{x}{X} \right)^2 - \left( \frac{y}{Y} \right)^2 - \left( \frac{z}{Z} \right)^2 \right]^{\frac{\gamma}{\gamma-1}}, \quad (4.15)$$

$$I_2(\gamma) = \left( \frac{\pi^{\frac{3}{2}}}{2(\gamma-1)} \right) \left( \frac{\Gamma(\alpha+2)}{\Gamma(\alpha+\frac{7}{2})} \right), \quad (4.16)$$

$\gamma$  is a thermodynamic property, whereby for a monatomic ideal gas  $\gamma = 5/3$ . For low temperature plasmas the value is lower. In this work, a value of 1.25 is used.

$\varepsilon$  is the thermal energy per unit mass of ablated material  $\varepsilon = E_p/M_p$  (J/kg). It is calculated using Strikovski's model (Strikovski et al., 2010).  $E_p$  is the thermal energy of the initial plume and  $M_p$  is its mass, in J and kg, respectively.

$X_o$ ,  $Y_o$ , and  $Z_o$  are taken as 0.76 mm, 0.7 mm, and 0.1 mm, respectively (Strikovski et al., 2010).  $X$ ,  $Y$ , and  $Z$  (uppercase) are the full dimensions of the expanding plasma. They are taken as 1.1 cm, 2.5 cm, and 5 cm (or 7 cm), respectively.  $x$ ,  $y$ , and  $z$  (lowercase) are the coordinates of any ion or particle within the full range plasma, in cm.

$I_2(\gamma)$  is a function of the adiabatic index and is dimensionless. It is calculated using Equation (4.16) as 120.

$\Gamma(z)$  is the Gamma-function, and  $\alpha = 1/(\gamma-1)$  is a thermodynamic property

The calculated pressures and temperatures of ions on impact in vacuum (at 5 cm substrate-target distance) are listed in Table 4.2. Apparently, for all values of accelerating voltage, in the range of 10 kV to 20 kV, ablation would produce extremely high energy bombarding ions that are energetic enough to end up lying inside the diamond region in the carbon phase diagram upon condensation, as discussed in section 4.5.

**Table 4.2: Temperature and pressure of ions on impact at different accelerating voltage estimated using the shockwave model – vacuum condition and at 5 cm substrate-target distance.**

Voltage (kV)	T(ablation) (K)	E (GJ)	T (on impact)(K)	P (on impact) (GPa)
10	92 876	0.0961	11 062	74.7
12	107 948	0.111	12 858	86.9
14	113 119	0.117	13 474	91.0
16	107 948	0.112	12 858	86.9
18	104 876	0.109	12 492	84.4
20	102 066	0.106	12 157	82.1

#### 4.4.2 Plasma Expansion in Ambient Gas

In this work, ablation is carried out in a background gas, namely Argon at  $\sim 0.53$  Pa. Therefore, the pressure and temperature of bombarding carbon ions on impact must be corrected using ambient gas conditions, as explained next.

With a background gas present, the plume species will undergo not only collisions within the plasma but also with the ambient gas. These collisions between the plasma and the gas particles, where a transfer of internal and kinetic energy will occur, result in a reduced expansion velocity of the plasma particles. The slowing and attenuation dynamics of pulsed electron ablation plasmas in low-pressure background gases are of significant interest for film growth by PEBA. The magnitude and kinetic energy of the species arriving at the substrate are key processing parameters in the case of diamond deposition as explained earlier.

Compared to plume expansion in vacuum, the interaction of the plume with the background gas is a far more complex dynamical process due to the presence of many physical processes such as deceleration, attenuation, thermalization of the ablated species, diffusion, recombination, formation of shock waves, reactive scattering and clustering. Apparently, the background gas acts as a regulator of ablated plume energetics and strongly determines the composition and dynamical behavior of the plume material ablated.

In this section, the expression of the plasma pressure in an ambient gas, i.e., Equation (4.17), is used to further modify the results of pressure on impact obtained in vacuum in the previous section.

$$p_o = \frac{P_o X_o^3 (\eta_o \xi_o)^{1-\gamma}}{E}, \quad \text{Eqn (4.17)} \quad (\text{Anisimov et al., 1996})$$

$\xi_o$  and  $\eta_o$  are dimensionless quantities, where  $\xi_o = Z_o/X_o = 0.132$  and  $\eta_o = Y_o/X_o = 0.921$ .

$p_o$  (lowercase) is the ratio of pressure of bombarding ions on impact in vacuum to the pressure of bombarding ions on impact in a background gas, i.e.,  $P_{\text{vacuum}}/P_{\text{background}}$ . The calculated value of  $p_o$  is 1.36.  $P_{\text{vacuum}}$  is the pressure of bombarding ions on impact in vacuum (Pa). It is calculated using the aforementioned vacuum model, viz., Equation (4.15).

$P_o$  (uppercase) is the pressure of background gas in the deposition chamber (Pa), viz., 0.53 pa.

Equation (4.17) has been used to estimate the pressure of ions on impact on the substrate in the presence of an ambient gas in the PEBA chamber. My estimated pressure data of ions on impact (at 5 cm substrate-target distance) are listed in Table 4.3, and shown on the carbon phase diagram in Fig. 4.4. As can be appreciated, for all values of the accelerating voltage in the range 10 kV to 20 kV, ablation would result in ions energetic enough to be lying in the diamond region upon condensation.

## 4.5 Phase Estimation of Deposited Films

Figure 4.4 shows the stability regions of crystalline diamond and graphite in the pressure-temperature diagram. The roughly estimated deposition conditions (at substrate-target distance of 5 cm) of PEBA are indicated in the diagram according to the two aforementioned models, namely, Strikovski's and shock wave. Figure 4.5 illustrates my roughly estimated deposition conditions at a substrate-target distance of 7 cm, according to the same models.

**Table 4.3: Pressure of ions on impact estimated using the shockwave model (Anisimov et al., 1996) at different accelerating voltage values – both background gas and vacuum conditions are reported for a 5 cm substrate-target distance.**

Accelerating Voltage (kV)	P on impact – Background (GPa)	P on impact - Vacuum (GPa)
10	55.0	74.7
12	63.9	86.9
14	66.9	91.0
16	63.9	86.9
18	62.1	84.4
20	60.4	82.1

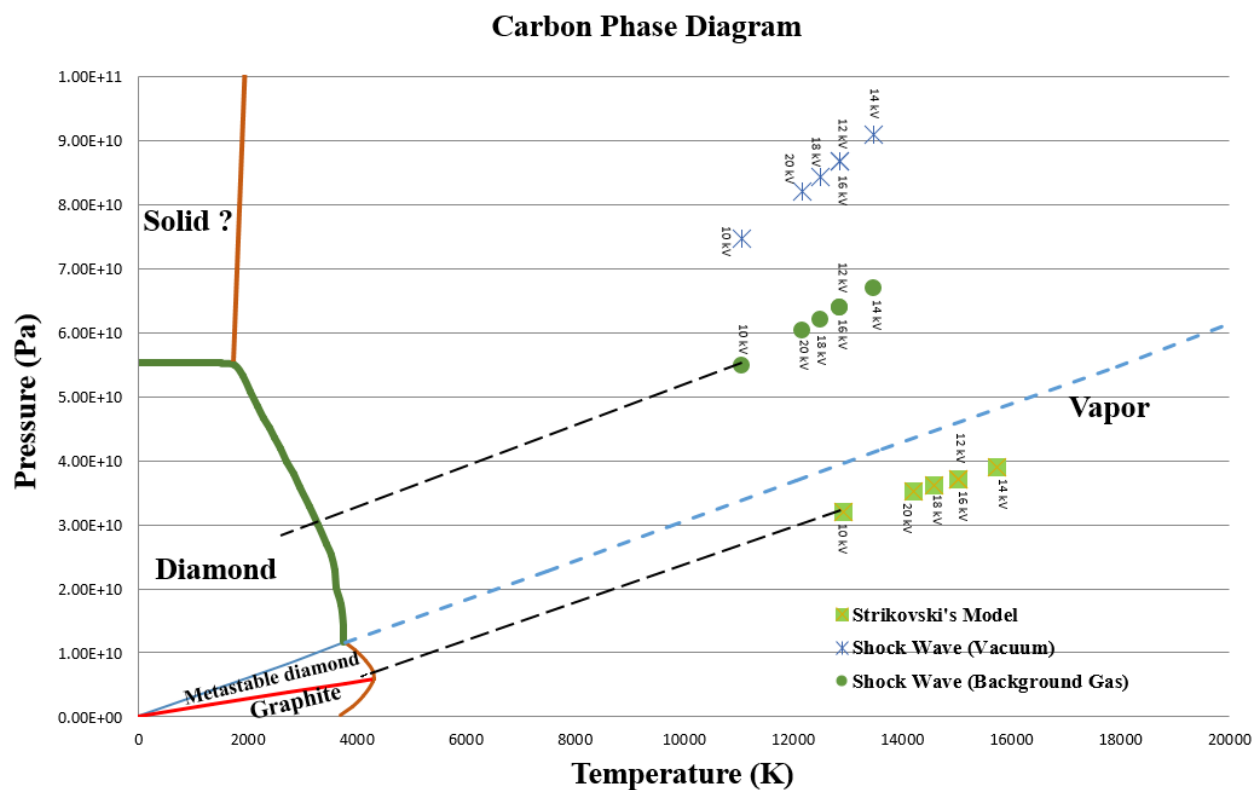


**Figure 4.4: Calculated results of pressure and temperature of ions on impact, as per target-substrate distance of 5 cm, obtained from various models, are shown in different annotations.**

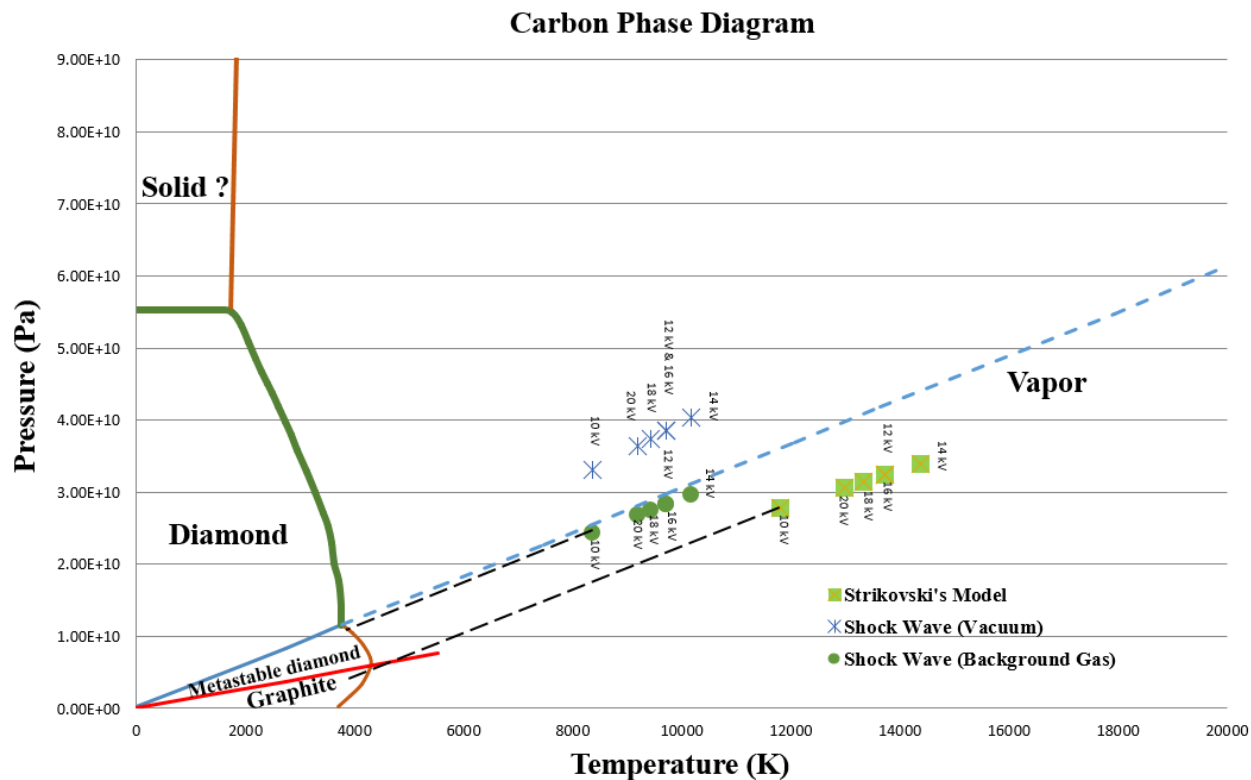


**Figure 4.5:** Calculated results of pressure and temperature of ions on impact, as per target-substrate distance of 7 cm, obtained from various models, are shown in different annotations.

According to Strikovski's model, at a substrate-target separation distance of 5 cm, our observations show that the cooling path to ambient conditions passes close to the line separating the regions of diamond and graphite into the diamond metastable phase region. The region of diamond metastable phase has been established experimentally by Zazula (1997). The calculated P-T-state at a substrate-target separation distance of 5 cm according to the shock wave model, lies well above the line separating the regions of diamond and graphite in the carbon phase diagram, as shown Fig. 4.4. Hence, it is showing that the state of the system after impact will likely pass through the diamond region of the phase diagram upon condensation. However, the calculated P-T-state, according to the shock wave model, at a 7 cm substrate-target distance, lies on the line separating the regions of diamond and graphite in the carbon phase diagram, see Fig. 4.5. That is, the state of the system, upon condensation on the substrate will likely pass through the graphite region of the phase diagram upon condensation.

## 4.6 Discussion of the Results

The calculated pressure and temperature of carbon ions upon impact on the substrate, under a background gas and according to the shock wave model, lie well above the graphite-to-diamond transformation line of the phase diagram. As an obvious condition for diamond formation, the temperature has to fall rather rapidly as compared to pressure decay. My operation conditions behave obviously in this sense and will likely yield films consisting of diamond. However, under vacuum, ablation would result in carbon ions with very high pressure and temperature upon impact, which may lead to the formation of either diamond or even an unknown solid carbon material upon condensation. According to Strikovski's model, the calculated pressure and temperature of carbon ions on impact lie just below the graphite-to-diamond transformation line of the phase diagram in Fig. 4.4. However, it will end up passing through the diamond metastable region upon condensation of carbon ions on the substrates.

The calculation results obtained from the shock wave model under a background gas are closest to PEBA conditions due to many reasons. First, PEBA cannot operate under deep vacuum. Most of the runs have been carried at  $\sim 0.5$  Pa, which is remarkably considered as a low-vacuum condition, but not deep vacuum. The main obstacle is the mutual space-charge repulsion among the electrons. Second, a target bombardment by a pulsed electron beam results in a shock wave propagation through the gas (Redel et al., 1992). Therefore, the shockwave model is in a better position to reflect PEBA conditions relatively to the macroscopic Strikovski's model.

The shock wave model under a background gas has indicated that a shorter target-substrate distance is conducive to diamond formation, i.e., 5 cm in our case. At a higher substrate-target distance, the pressure and temperature of ions on impact will tend to lie in the graphite phase region upon condensation. Moreover, under an accelerating voltage of 14.5 kV, the highest values of pressure and temperature of ions on impact are obtained. For comparison purposes, in this work, accelerating voltages of 13 kV and 16 kV will also be attempted in some experimental runs.

## **Chapter 5: Experimental Results and Discussion**

## 5.1 Introduction

NCD thin films have been deposited from an HOPG target onto various substrates by pulsed electron beam ablation. Details of the experimental procedure are given in Chapter 3, section 3.2.2. The films were characterized using visible Raman spectroscopy, visible spectroscopic reflectance, XRD, SEM, and AFM techniques, in order to evaluate their chemical composition, structure, thickness, and morphology. The effects of accelerating voltage, pulse repetition rate, heat treatment, and substrate material and temperature have been investigated, accordingly. The hardness of the films was evaluated by nano-indentation. The corresponding main results of the analyses are given and discussed in the following sections.

## 5.2 Results of First Series

In the first series of deposition experiments, we have changed a few operation conditions to study their effects on the growth of NCD films. These are the number of electron beam pulses (3500 and 5500), substrate temperature (RT and 150 °C), and substrate material. Other operation conditions such as accelerating voltage, frequency, substrate-target distance, and beam-target distance were fixed at 14 kV, 5 Hz, 5 cm, and 4 mm, respectively, see Chapter 3, section 3.2.2. The corresponding results are given next.

### 5.2.1 Film Thickness

Figures 5.1-4 show the reflectance response, obtained from visible spectroscopy of deposited NCD films on Si(100) and Si(111). The blue curve is the calculated reflectance response of the film, while the red curve is the measured one. The fit between the two curves is very good (maximum relative error of 5%) except for the films deposited at 150 °C, where the maximum relative error is of 30%. The resulting film thicknesses from all runs are shown in Fig. 5.5.

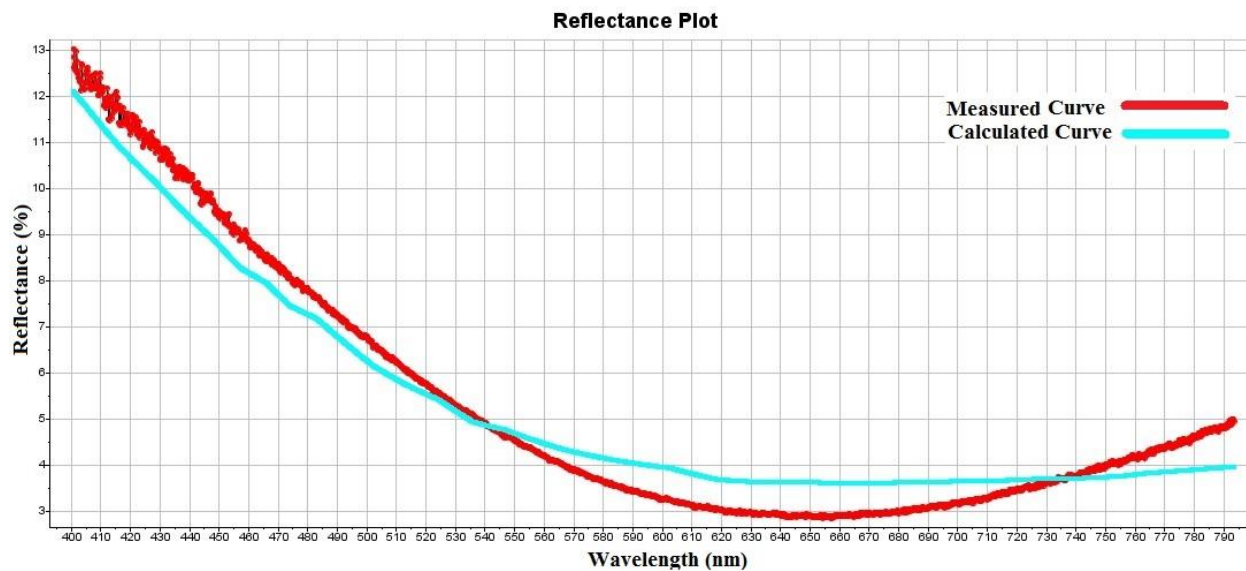


**Figure 5.1:** Visible spectroscopic reflectance of NCD film on Si(100) resulting from the first series at 5 Hz, 14 kV, and RT.

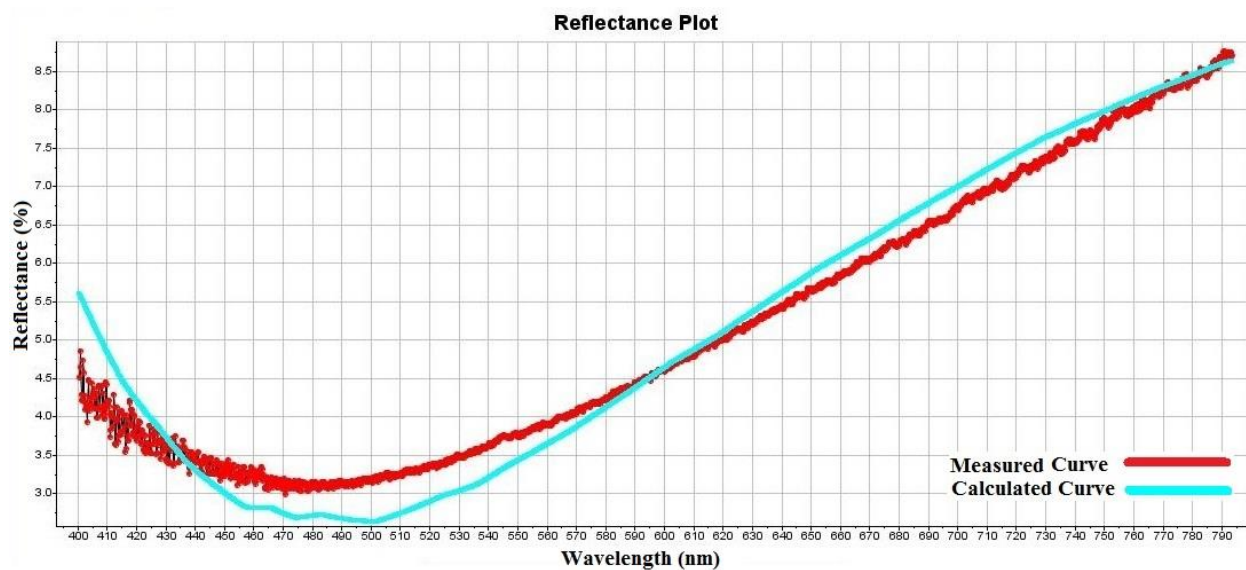


**Figure 5.2:** Visible spectroscopic reflectance of NCD film on Si(111) resulting from the first series at 3500 pulses, 14 kV, and RT.

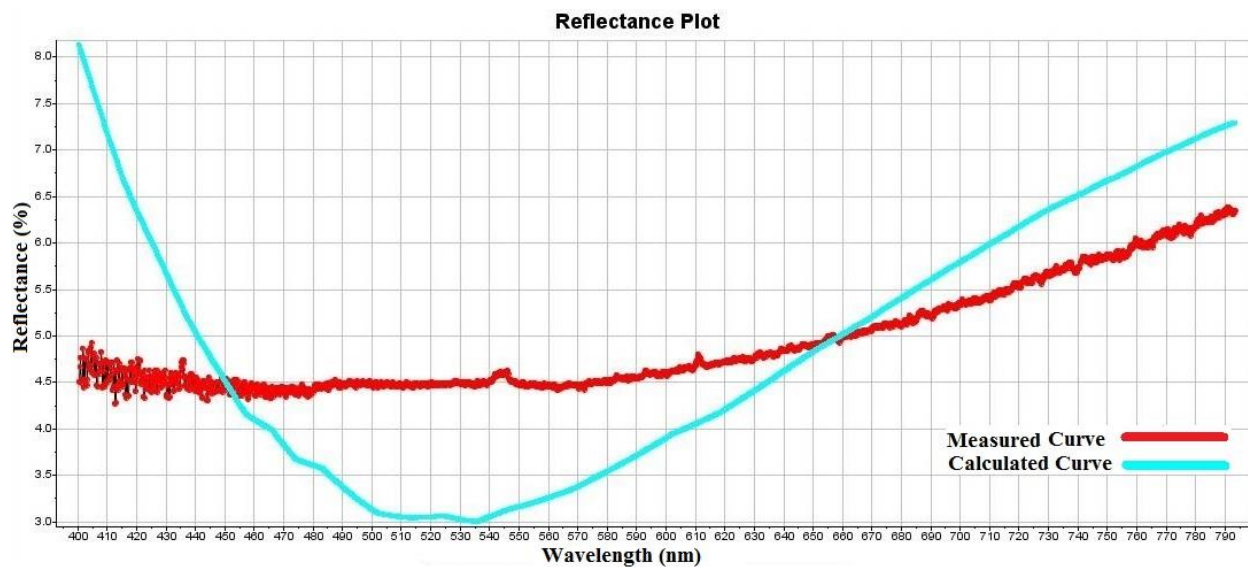


**Figure 5.3:** Visible spectroscopic reflectance of NCD film on Si(100) resulting from the first series at 3500 pulses, 14 kV, and 150 °C.

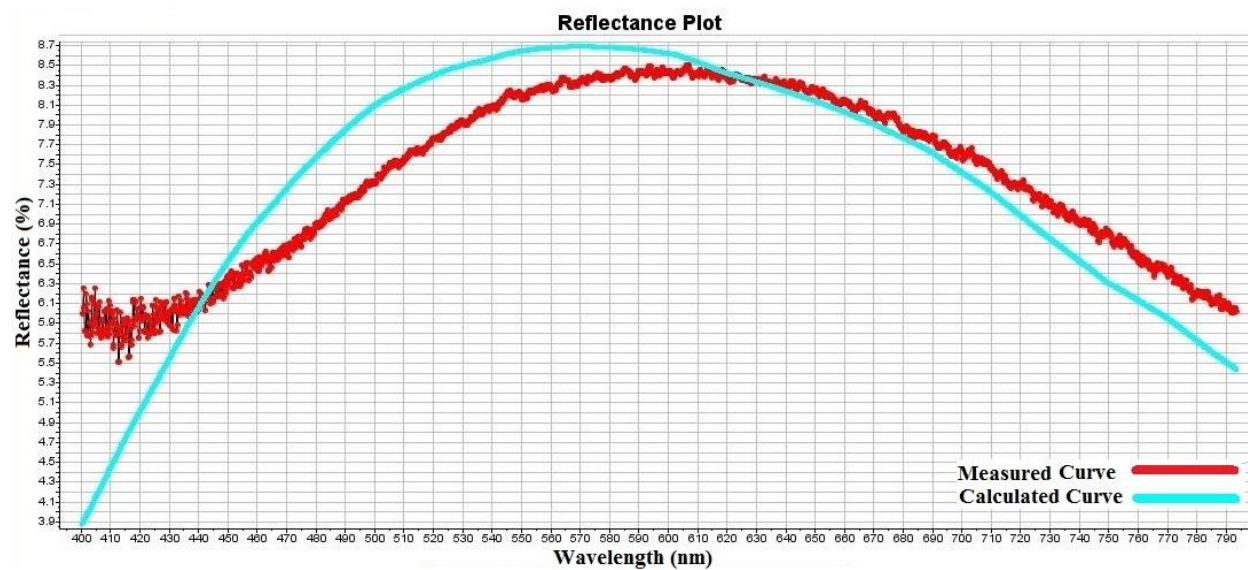


**Figure 5.4:** Visible spectroscopic reflectance of NCD film on Si(100) resulting from the first series at 5500 pulses, 14 kV, and RT.

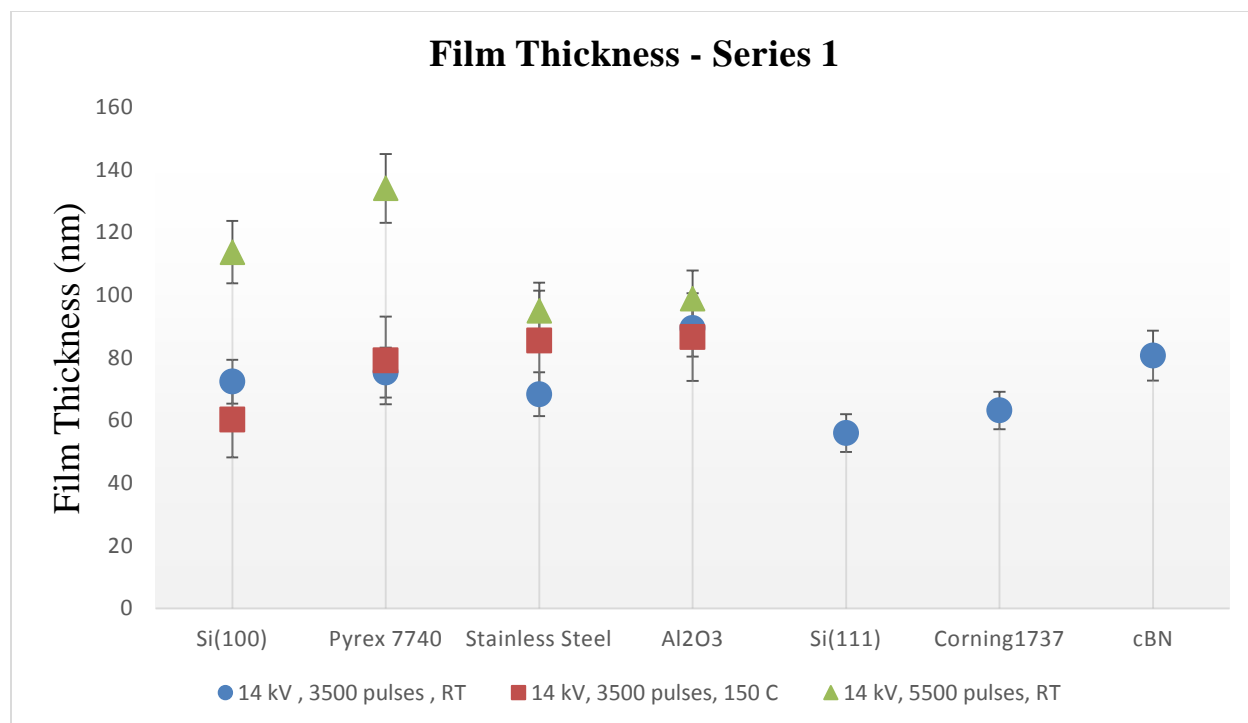


**Figure 5.5: Thickness of NCD films resulting from the first series on various substrates**

### 5.2.2 Crystal Size, $sp^3$ Content and Nanocrystallinity

Raman spectra have been collected in backscattered mode, at a grating of 1200, and an incident laser radiation wavelength of  $532\text{ cm}^{-1}$ . The spectra (average of 10 s spectra) have been obtained within the range  $1000\text{--}2000\text{ cm}^{-1}$ .

The recorded Raman spectra of deposited films, as listed in Table 5.1, are composed of the typical features of NCD. These features can be clearly distinguished after the deconvolution (using a mixed Gaussian-Lorentzian function, in this case) of the entire band and extraction of the baseline, as shown in Fig. 5.6 – 5.9 for all NCD films resulting from series 1. The resulting fitted curve is essentially indistinguishable from the overall measured signal. The deconvoluted spectrum consists of many signals, which include the diamond peak at  $1332\text{ cm}^{-1}$ , diamond nanocrystallites peak at  $1150\text{ cm}^{-1}$ , the so-called G ( $1536\text{--}1565\text{ cm}^{-1}$ ) and D ( $1343\text{--}1378\text{ cm}^{-1}$ ) bands arising from disordered and/or amorphous carbon, and the t-PA (trans-polyacetylene) band ( $1450\text{--}1463\text{ cm}^{-1}$ ) (Ferrari and Robertson 2001). The fraction of  $sp^3$  carbon bonded atoms in the nanocomposite is calculated using Equation (5.1) (Ballutaud et al. 2008). It is to be mentioned that visible Raman is

a weak scatter of  $sp^3$  sites relatively to  $sp^2$  sites by a factor of 50 – 230 (Ferrari and Robertson 2001). In the calculation of the  $sp^3$  percentage, a conservative value of 75 (see Equation 5.1) has been used.

$$\frac{sp^3}{sp^3+sp^2} \% = \left[ 1 - \frac{I_G}{75 \times (I_{1332} + I_{1150}) + I_G} \right] \times 100 \quad (5.1)$$

$I_G$ : Intensity of G band peak within the range 1536-1565  $cm^{-1}$

$I_{1150}$ : Intensity of NCD band peak at 1150  $cm^{-1}$

$I_{1332}$ : Intensity of diamond band peak at 1332  $cm^{-1}$

**Table 5.1: Results of Raman spectra deconvolution of all NCD films resulting from the first series**

Deposition Conditions	Sample	$I_G$	$I_{G'}$	$I_{1332}$	$I_D$	$I_{1150}$	$I_{1250}$	$I_{1480}$
14 kV, RT, 3500 pulses	Pyrex	4623	3421	1549	3237	1003	1769	6280
	S.S.	16013	NA	4070	6942	2237	5065	20110
	Si(100)	7052	NA	2692	3222	1332	2625	10272
	Sapphire	8808	NA	2790	3737	1450	2290	10441
	Corning	4988	NA	1232	2318	850	1504	5502
	Si(111)	1310	5724	2061	3407	1253	2182	4623
	cBN	2944	NA	1554	2155	929	1784	6041
14 kV, 150 °C, 3500 pulses	Pyrex	1336	3111	453	1289	352	645	581
	S.S.	2105	2617	594	1290	489	1042	2170
	Si(100)	1109	1546	420	777	327	733	1456
	Sapphire	1695	1241	421	895	363	603	818
14 kV, RT, 5500 pulses	Pyrex	5970	NA	2258	2681	1249	2431	5852
	S.S.	6562	NA	2050	2900	1070	2032	4200
	Si(100)	4814	NA	2595	1690	1190	1702	7370
	Sapphire	6004	NA	2540	2900	1145	1700	3700

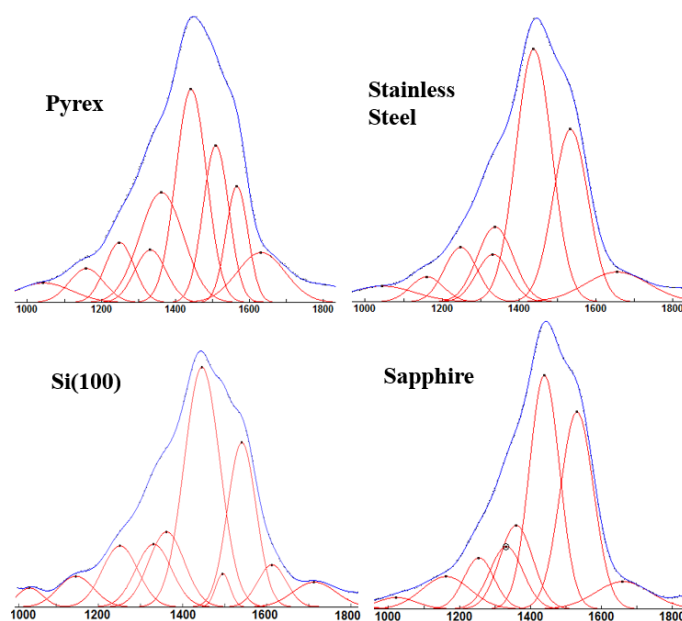


**Figure 5.6: Raman spectra (and their deconvolution) of NCD films on various substrates resulting from the first series at 3500 pulses, 14 kV, and RT.**

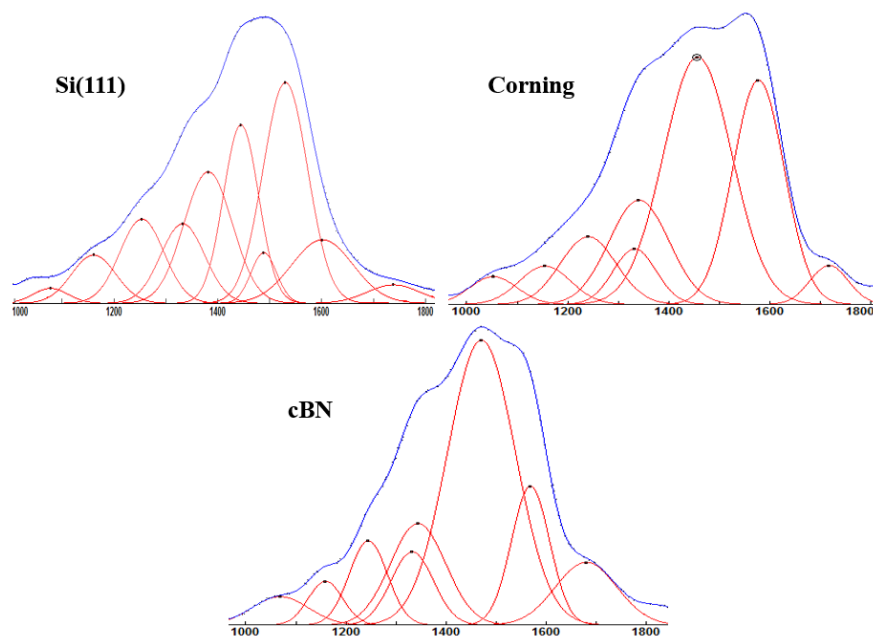


**Figure 5.7: Raman spectra (and their deconvolution) of NCD films on various substrates resulting from the first series at 3500 pulses, 14 kV, and RT.**

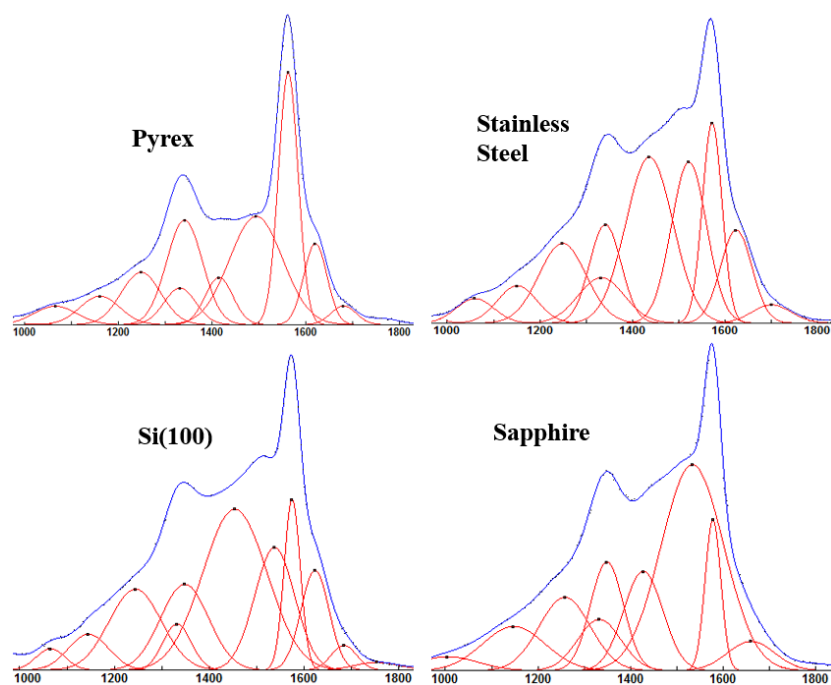


**Figure 5.8: Raman spectra (and their deconvolution) of NCD films on various substrates resulting from the first series at 3500 pulses, 14 kV, and 150 °C.**

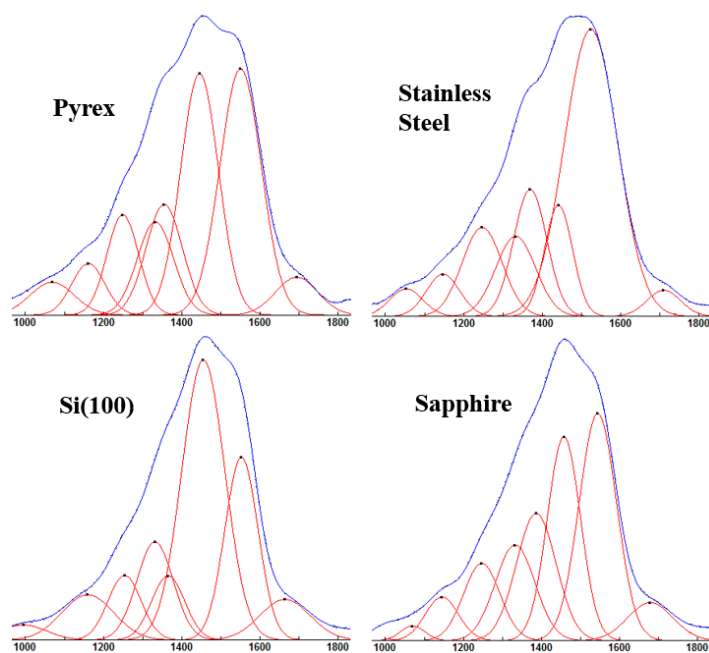


**Figure 5.9: Raman spectra (and their deconvolution) of NCD films on various substrates resulting from the first series at 5500 pulses, 14 kV, and RT.**

The nanocrystalline percentage in the films has been inferred by calculating the ratio  $((I_{1332} + I_{1150})/\Sigma(I))$  (Popov et al., 2007), where the sum is over the entire spectrum. The crystal size could be estimated as  $I_{1332}/I_{1150}$  (Klauser et al., 2010). The calculated values of the  $sp^3\%$  are shown in Fig. 5.10, and the calculated values of nanocrystalline percentage and crystal size are shown in Fig. 5.11, and Fig. 5.12, respectively.

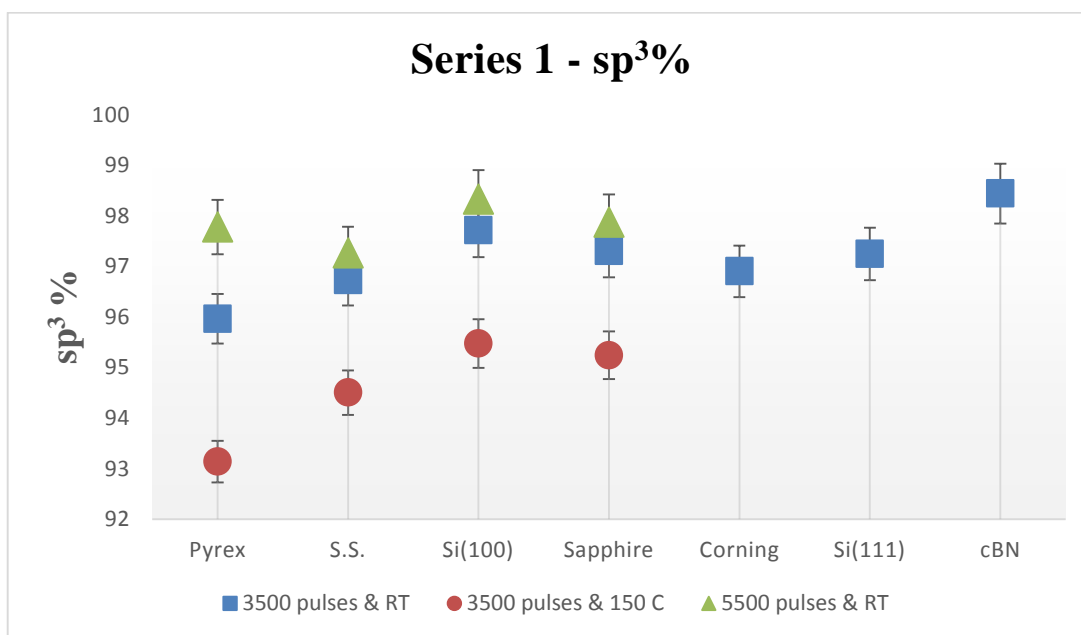


**Figure 5.10:  $sp^3$  percentage in films resulting from the first series.**

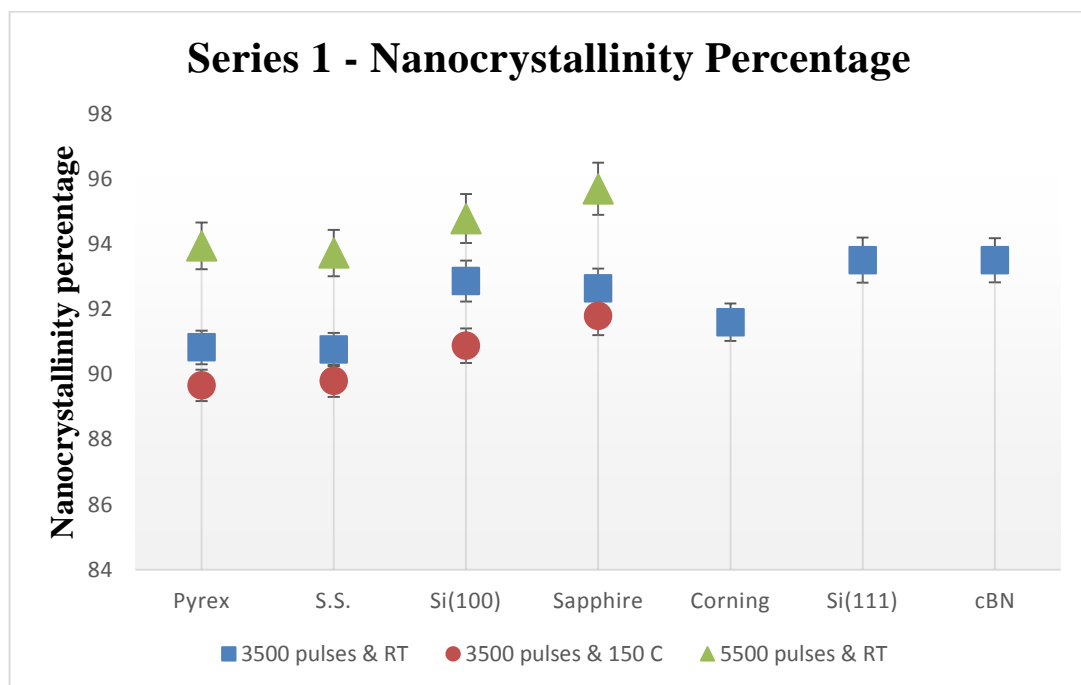


**Figure 5.11: Nanocrystallinity percentage in films resulting from the first series.**



**Figure 5.12: Crystal size in films resulting from the first series.**

### 5.2.3 Film Morphology

The morphology of NCD films resulting from series 1 as revealed by AFM analysis, and depicted in Fig. 5.13 - 5.16, consists of clusters of crystallites with size in the range of ~50 nm to ~150 nm.

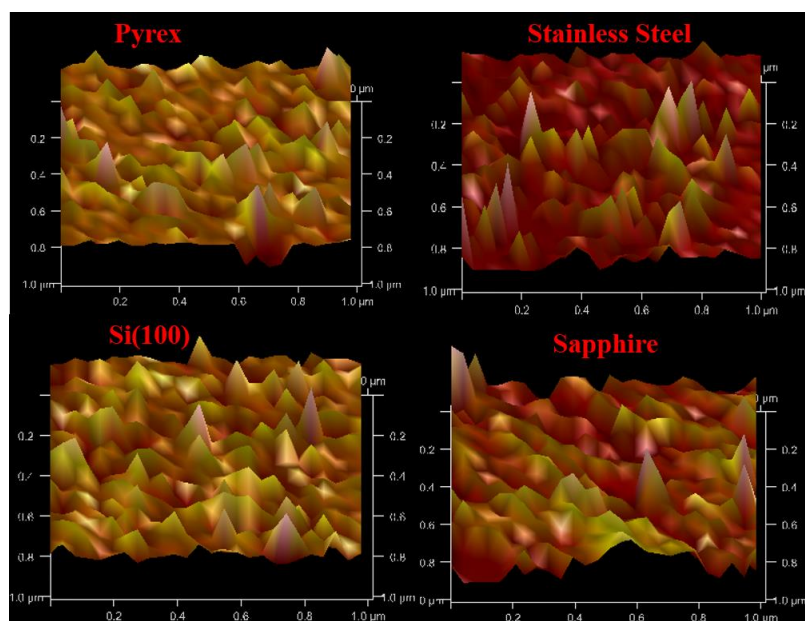


**Figure 5.13: AFM three-dimensional view of film morphology of NCD films resulting from the first series – 14 kV, 3500 pulses, and RT. Four different substrates are shown.**

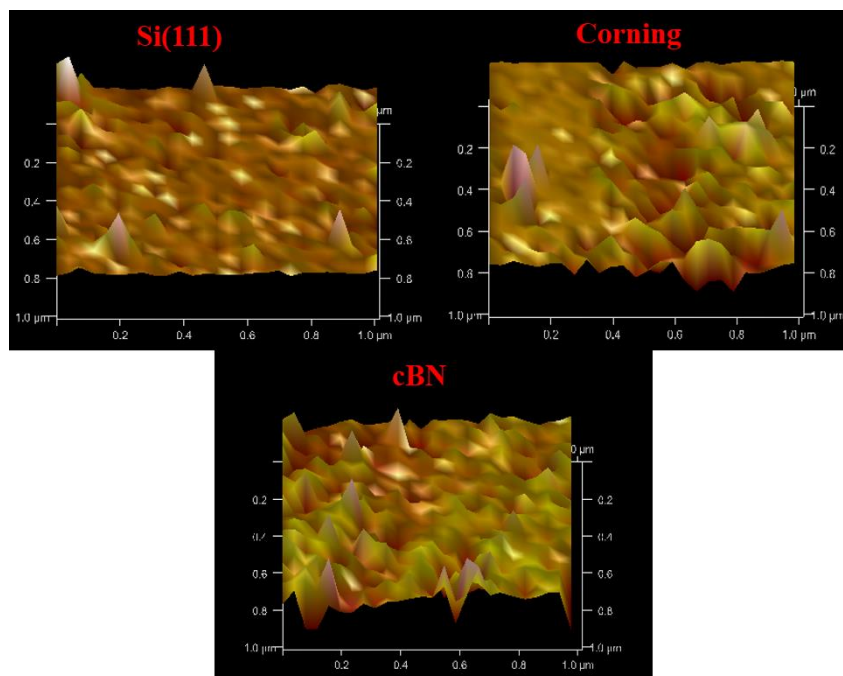


**Figure 5.14: AFM three-dimensional view of film morphology of NCD films resulting from the first series – 14 kV, 3500 pulses, and RT. Three different substrates are shown.**

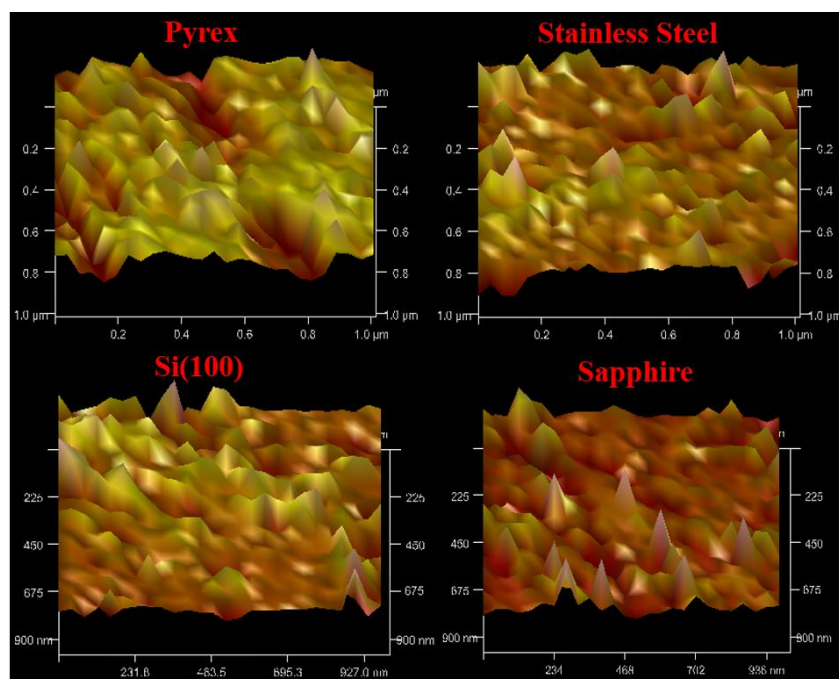


**Figure 5.15: AFM three-dimensional view of film morphology of NCD films resulting from the first series – 14 kV, 3500 pulses, and 150 °C. Four different substrates are shown.**

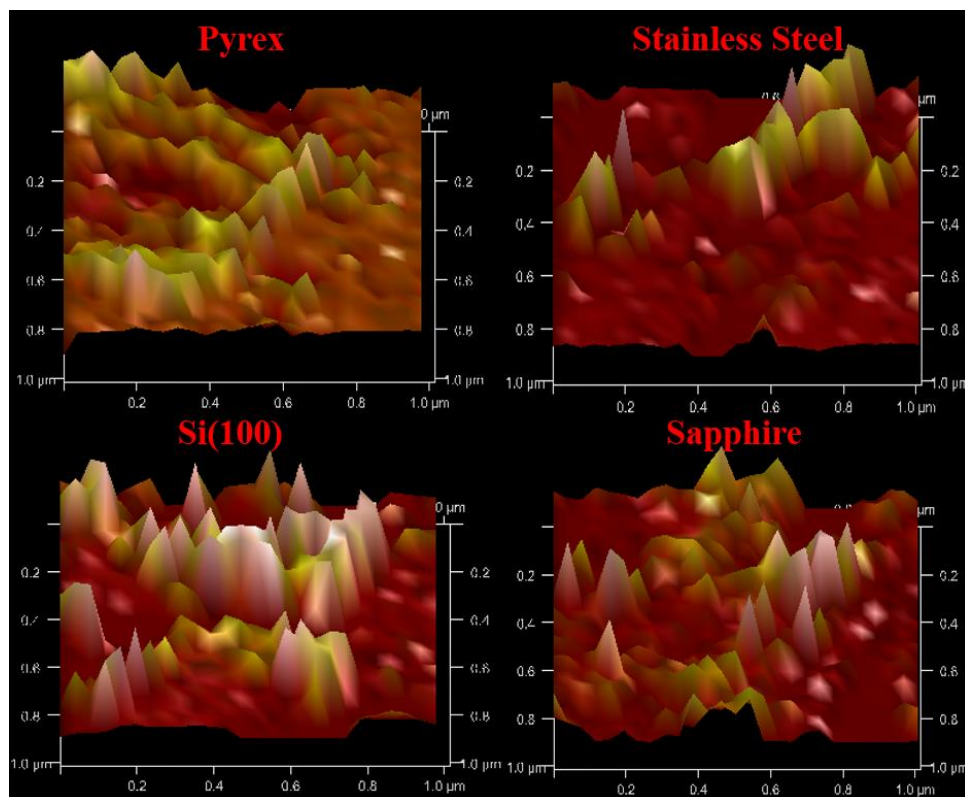


**Figure 5.16: AFM three-dimensional view of film morphology of NCD films resulting from the first series – 14 kV, 5500 pulses, and RT. Four different substrates are shown.**

The clusters appear to grow along a preferential direction for films grown at RT. With respect to crystal size criterion, films deposited at 14 kV, 3500 pulses, and RT are consistent with the crystal size expected for NCD, i.e., a maximum of 150 nm.

AFM images show a larger cluster size as the number of electron beam pulses is increased from 3,000 pulses to 5,000 pulses, i.e., as the film thickness increases. Accordingly, for samples prepared at 5500 pulses, the crystal size is in the few hundreds of nm. In samples resulting from series 1, the cluster size does not appear to be uniformly distributed over the surface. Typical SEM images (Fig. 5.17) of NCD films on Si(100) reveal variations in the morphology of films deposited in series 1.

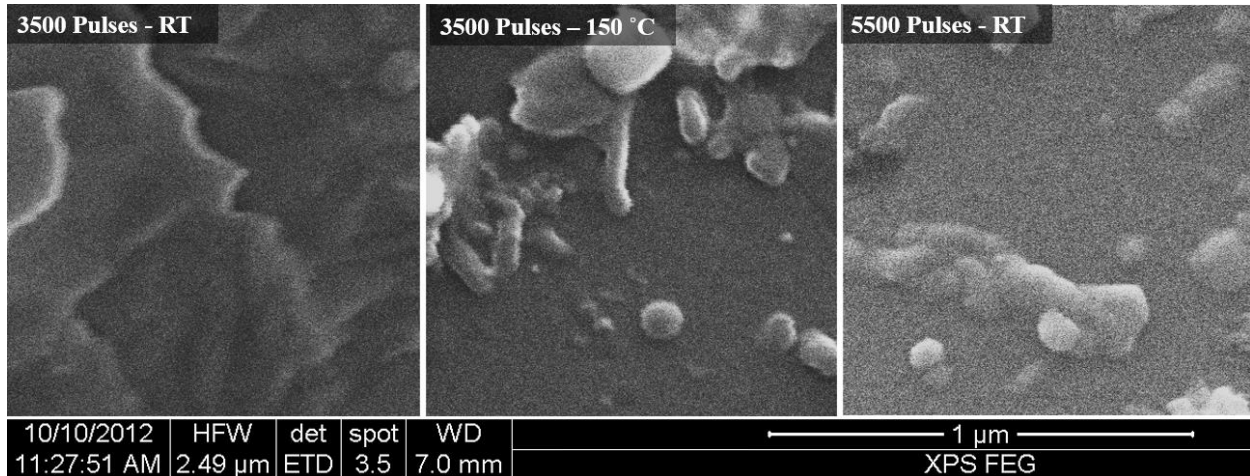


**Figure 5.17: SEM images of films on Si(100) resulting from the first series at different operating conditions.**

#### 5.2.4 Film hardness

The load-displacement curves obtained on indentation of the films on pyrex to various maximum loads up to  $\sim 2.5$  mN are shown in Fig. 5.18. Other curves obtained for all other samples produced in this work have a similar trend to the one in Fig. 5.18. Results of film hardness of NCD films, on various substrates (at 14 kV, 5500 pulses, and RT), are summarized in Table 5.2. Hardness results of the aforementioned samples have been calculated for penetration depths corresponding to their film thickness. These results consist of combined hardness of the whole assembly, i.e., NCD film on substrate. Values of hardness of the bare substrates, namely, Si(100), pyrex, stainless steel, and sapphire are also listed in Table 5.2. Equation (5.2) could be useful in order to eliminate the substrate effect and account only for NCD film hardness (Xu, 2004).

$$\frac{H_{com}}{H_f} = \frac{H_s}{H_f} + \left[ 1 - \frac{H_s}{H_f} \right] \exp \left[ - a_Y a_E \left( \frac{h}{t} \right)^2 \right] \quad (5.2)$$

$H_{com}$  : Combined hardness (MPa)

$H_f$  : Film hardness (MPa)

$H_s$  : Substrate hardness (MPa)

$a_Y$  : The ratio of the yield stress of substrate to that of the film

$a_E$  : The ratio of the elastic modulus of substrate to that of the coating or film

$h$  : Penetration depth (nm)

$t$  : Film thickness (nm)

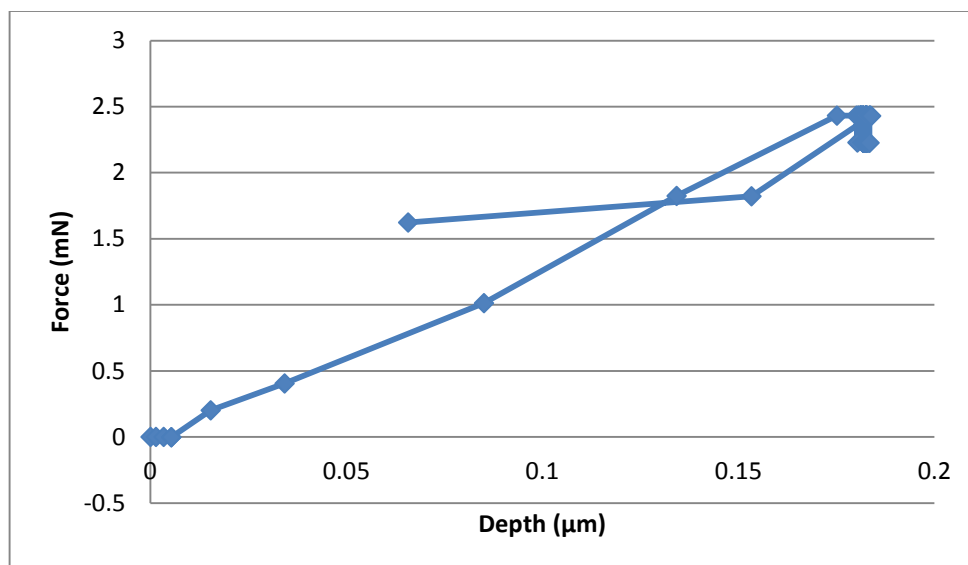


**Figure 5.18: Load and unload displacement curves obtained from nanoindentation of NCD films on Pyrex resulting from series 1 at 5500 pulses and RT.**

**Table 5.2: Substrate, combined, and film hardness for NCD films resulting from the first series - 14 kV, 5500 pulses, and RT.**

Sample	Film Hardness (MPa)	Combined Hardness (MPa)	Thickness (nm)	Substrate Hardness (Mpa)
Pyrex	19182	19146	134	3500
S.S.	18834	18413	95	2500
Si(100)	18511	18373	113	8000
Sapphire	19494	19154	98	18000

### 5.3 Discussion of the Results of the First Series

The deposited films have a thickness in the range of 60 nm – 135 nm, as shown in Fig. 5.5. The recorded Raman spectra of the resulting films from series 1 are composed of the typical features of NCD, as discussed in section 3.4.2, Chapter 3. The films exhibit  $sp^3$  in the range of 93.1% -

98.5%, as shown in Fig. 5.10;  $sp^3\%$  is lowest for films deposited at 150 °C. This is due to a diffusion activated mechanism of  $sp^3$ - $sp^2$  phase transformation, which occurs as a subsequent stage of carbon subplantation into films deposited at substrate temperature at and above 150 °C (Lifshitz et al., 1995). This conclusion has also been confirmed by Voevodin and Donley (1996), who have reported that the microstructure of the deposits becomes graphite-like instead of diamond-like for deposition temperatures  $\geq 150$  °C.

Films nanocrystallinity percentage ranges between 90% and 95%, as shown in Fig. 5.11, and the crystal size is in the range of 0.95 – 1.35, as shown in Fig. 5.12. The morphology of the films as revealed by AFM (Fig. 5.13 - 5.16) and SEM (Fig. 5.17) consists of clusters of crystals (grains) with size in the range of ~50 nm to ~150 nm. The hardness of the films is within the range of 18.5 GPa – 19.5 GPa, as listed in Table 5.2, which is consistent with the microhardness of NCD films reported in the open literature, see Table 2.1, Chapter 2.

### 5.3.1 Effect of Substrate Material

Films resulting from series 1 at 14 kV, 3500 pulses, and RT have been deposited on seven different substrates, namely, Si(100), Si(111), stainless steel, sapphire, cBN, corning, and pyrex. The thickness of the films deposited on Si(100), pyrex, stainless steel, sapphire, and cBN is within the range of 60 nm – 80 nm, as shown in Fig. 5.5. However, a thinner film of ~ 56 nm is deposited on Si(111) compared to the other samples. The reason for this is not clear yet. According to the data in Fig. 5.5, film thickness does not seem to be dramatically affected by the type of substrate material.

All films resulting from series 1 at 14 kV, 3500 pulses, and RT have  $sp^3\%$  in the range of 96% - 98% (Fig. 5.10), nanocrystallinity percentage in the range of ~ 91.0% - 93.5% (Fig. 5.11), and crystals size in the range of ~ 1.5 – 2.0 (Fig. 5.12). Therefore, the substrate material does not seem to substantially affect  $sp^3\%$ , nanocrystallinity percentage, and crystal size in the films. Raman data in terms of crystal size are consistent with AFM and SEM results.

### 5.3.2 Effect of Substrate Temperature

In series 1, for films deposited at 150 °C, the thickness is not noticeably different from the thickness of the films deposited at RT, as shown in Fig. 5.5. Films deposited at 150 °C exhibit less  $sp^3\%$  (Fig. 5.10) compared to films deposited at room temperature and under the same other conditions.

$sp^3\%$  is maximum for samples deposited at 150 °C on Si(100) and sapphire, and is minimum for samples on pyrex. The growth of carbon clusters of  $sp^2$  structure seem to be favored at high temperature, which is in agreement with many literature reports (Lifshitz et al., 1995; Voevodin and Donley, 1996; Balon et al., 2005).

Nanocrystallinity percentage in all NCD films resulting from series 1 at 150 °C is in the range of ~90% - 92%, which is lower than that of films obtained at room temperature, as shown in Fig. 5.11. High substrate temperature during NCD growth would promote graphitization, which means the distortion from  $sp^3$  carbon bond to  $sp^2$  carbon bond combined group. It will affect diamond film growth and nucleation, and increase the content of amorphous carbon in the resulting films (Wang et al., 2010; Williams, 2011). Moreover, the crystal size in films deposited at 150 °C is smaller ( $I_{1332}/I_{1150} = 1.2$ ) compared to films deposited at room temperature, as shown in Fig. 5.12. At high substrate temperature, AFM (Fig. 5.15) and SEM (Fig. 5.17) images do not show well developed clusters relatively to films obtained at room temperature. This is consistent with the results obtained from Raman analysis.

### 5.3.3 Effect of Pulse Number

In series 1, the deposition of NCD films using 5500 pulses has been attempted. The films obtained at 5500 pulses exhibit a remarkably higher thickness relatively to films resulting from series 1 at 3500 pulses and same other conditions, as shown in Fig. 5.5. The maximum difference of 59 nm is observed for films on pyrex. A higher number of pulses would result in a larger amount of ablated material, and larger amount of deposits, which is expected. Exception can be observed for films on sapphire, where the difference in thickness is of only 10 nm relatively to films produced at 3500 pulses.

All films deposited at 5500 pulses exhibit slightly more  $sp^3\%$  (in the range of 0.5% - 1.5%) compared to the ones produced at 3500 pulses, as shown in Fig. 5.10. Nanocrystallinity percentage in all films resulting at 3500 pulses is within the range ~ 90.8% - 93.5%, as shown in Fig. 5.11. However, nanocrystallinity percentage in all films produced at 5500 pulses is within the range 93.7% - 95.7%. Apparently, films deposited at 3500 pulses have a slightly smaller nanocrystallinity percentage.

Finally, films deposited at 5500 pulses seem to exhibit larger crystals ( $I_{1332}/I_{1150}$  within 1.81 – 2.22) relatively to films obtained at 3500 pulses, as shown in Fig. 5.12. These results are in good agreement with AFM (Fig. 5.13 – 5.16) and SEM (Fig. 5.17) data.

## 5.4 Results of Second Series

In the second series of deposition experiments, I have changed a few operation conditions to study their effects on the growth of the films. The conditions in question are the pulse repetition rate (5 Hz and 8 Hz), accelerating voltage (13 kV, 14.5 kV, and 16 kV), and substrate material. Other operation conditions such as substrate temperature, substrate-target distance, and beam-target distance were fixed at RT, 5 cm, and 4 mm, respectively, see Chapter 3, section 3.2.2. The corresponding results are given next.

### 5.4.1 Film Thickness

Figures 5.19 - 24 show the reflectance response which has been obtained from visible spectroscopy of deposited NCD films on Si(100). The blue curve is the calculated reflectance response of the film, while the red curve is the measured one. The fit between the two curves is very good (maximum relative error of 5%). The resulting film thickness data from all runs are shown in Fig. 5.25.

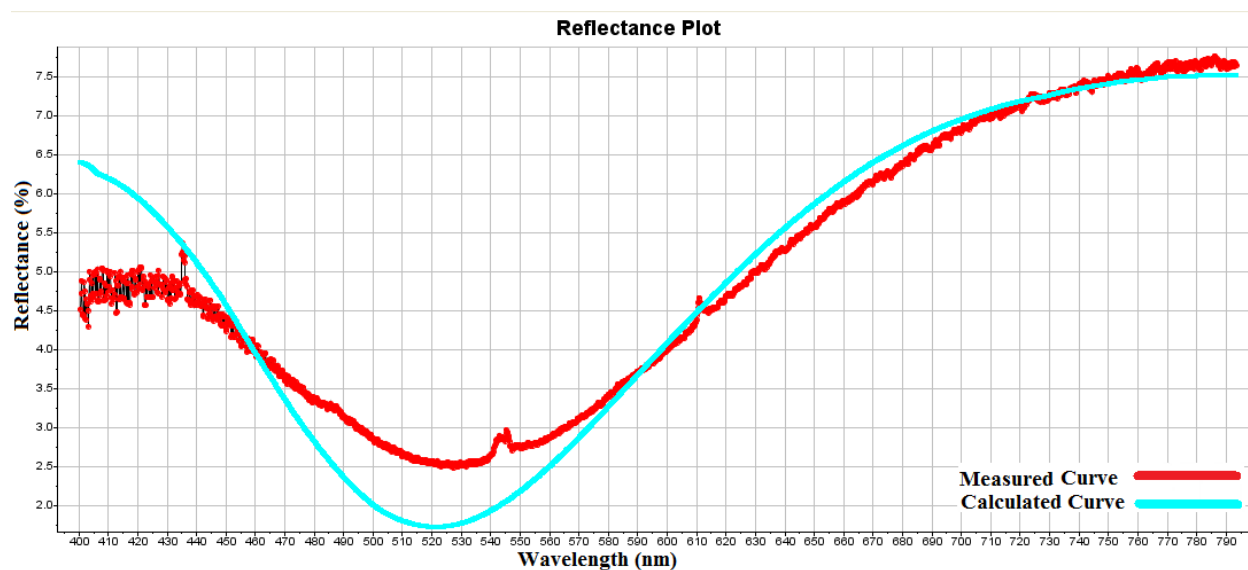


**Figure 5.19: Visible spectroscopic reflectance of NCD film on Si(100) resulting from the second series - 14.5 kV and 8 Hz.**

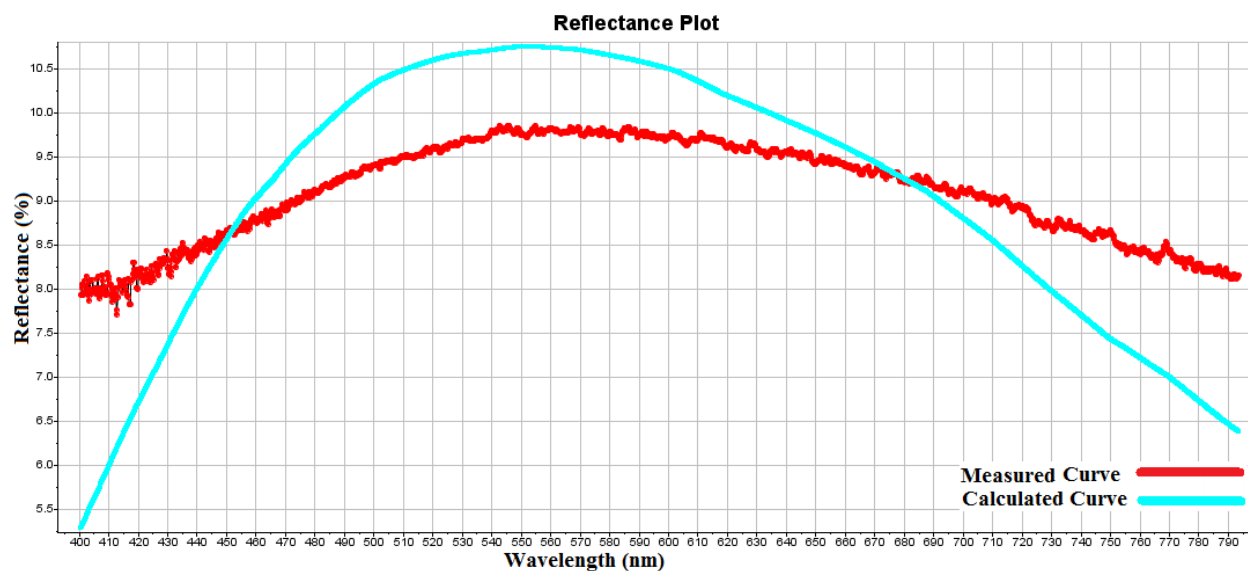


**Figure 5.20:** Visible spectroscopic reflectance of NCD film on Si(100) resulting from the second series - 16 kV and 8 Hz.

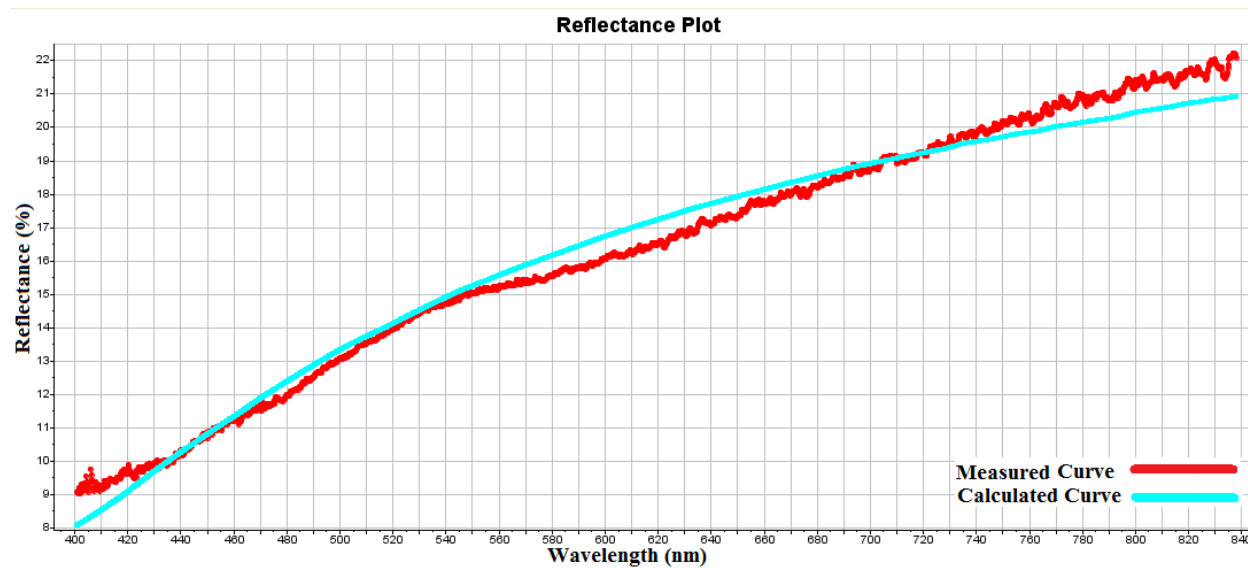


**Figure 5.21:** Visible spectroscopic reflectance of NCD film on Si(100) resulting from the second series - 13 kV and 8 Hz.

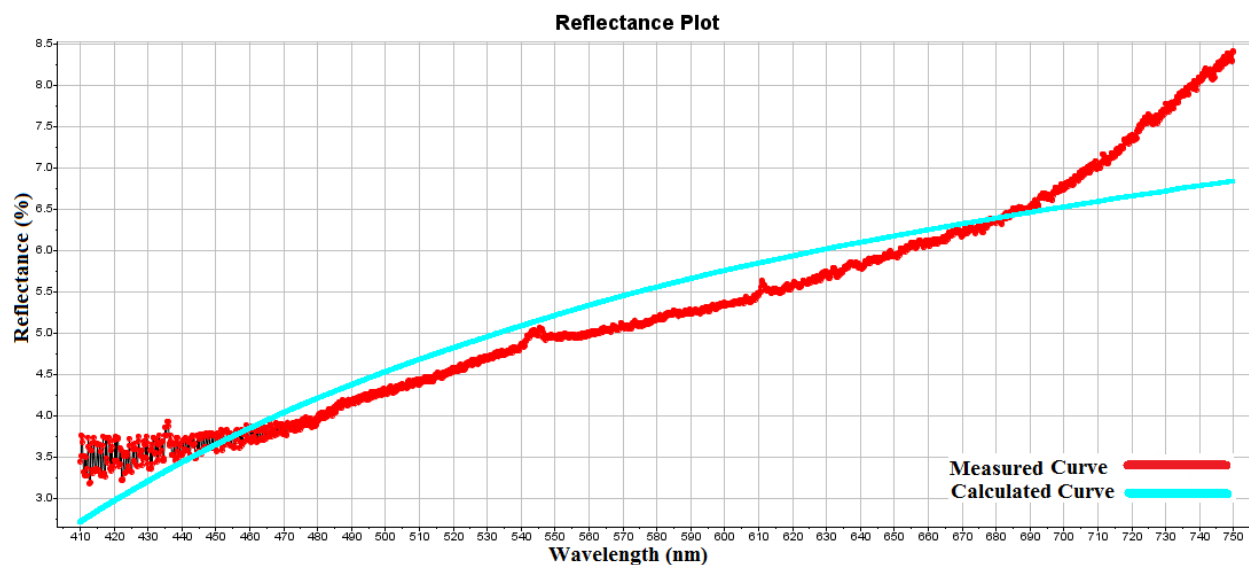


**Figure 5.22: Visible spectroscopic reflectance of NCD film on Si(100) resulting from the second series - 14.5 kV and 5 Hz.**

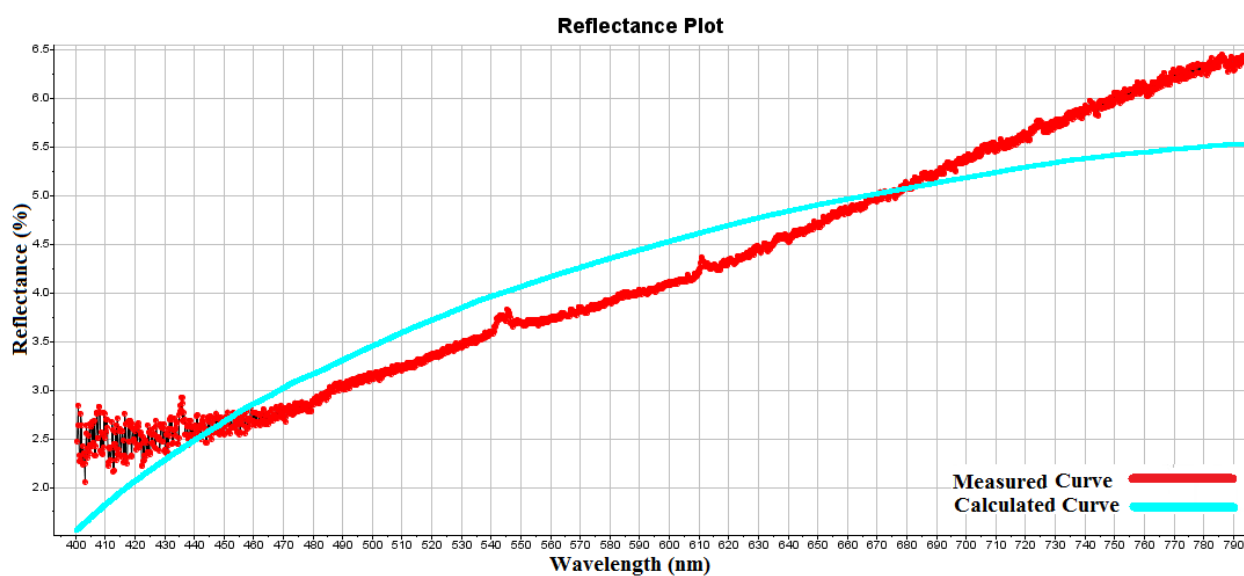


**Figure 5.23: Visible spectroscopic reflectance of NCD film on Si(100) resulting from the second series - 16 kV and 5 Hz.**

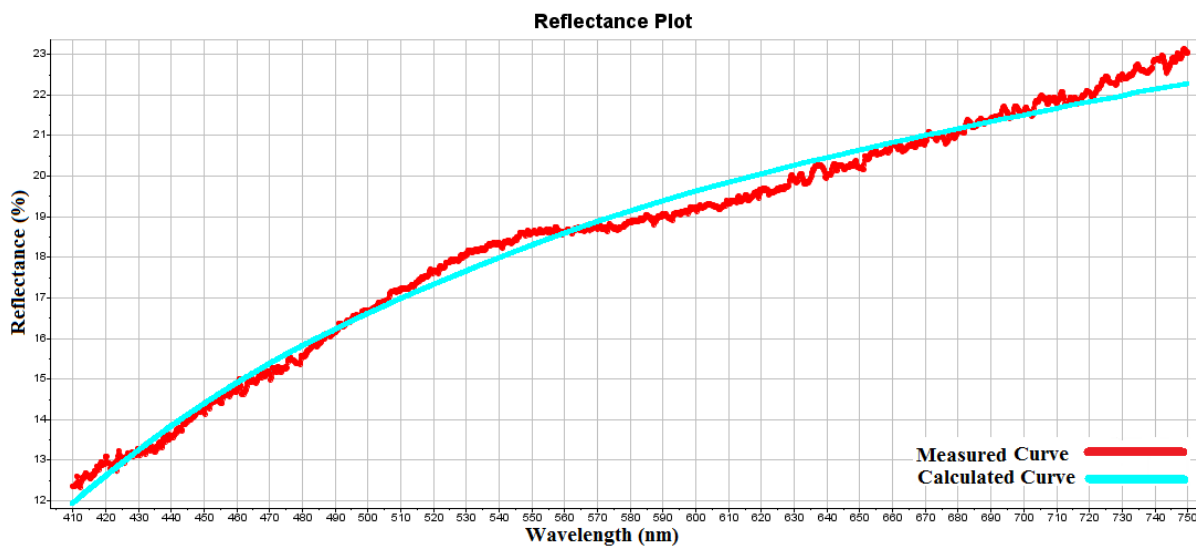


Figure 5.24: Visible spectroscopic reflectance of NCD film on Si(100) resulting from the second series - 13 kV and 5 Hz.

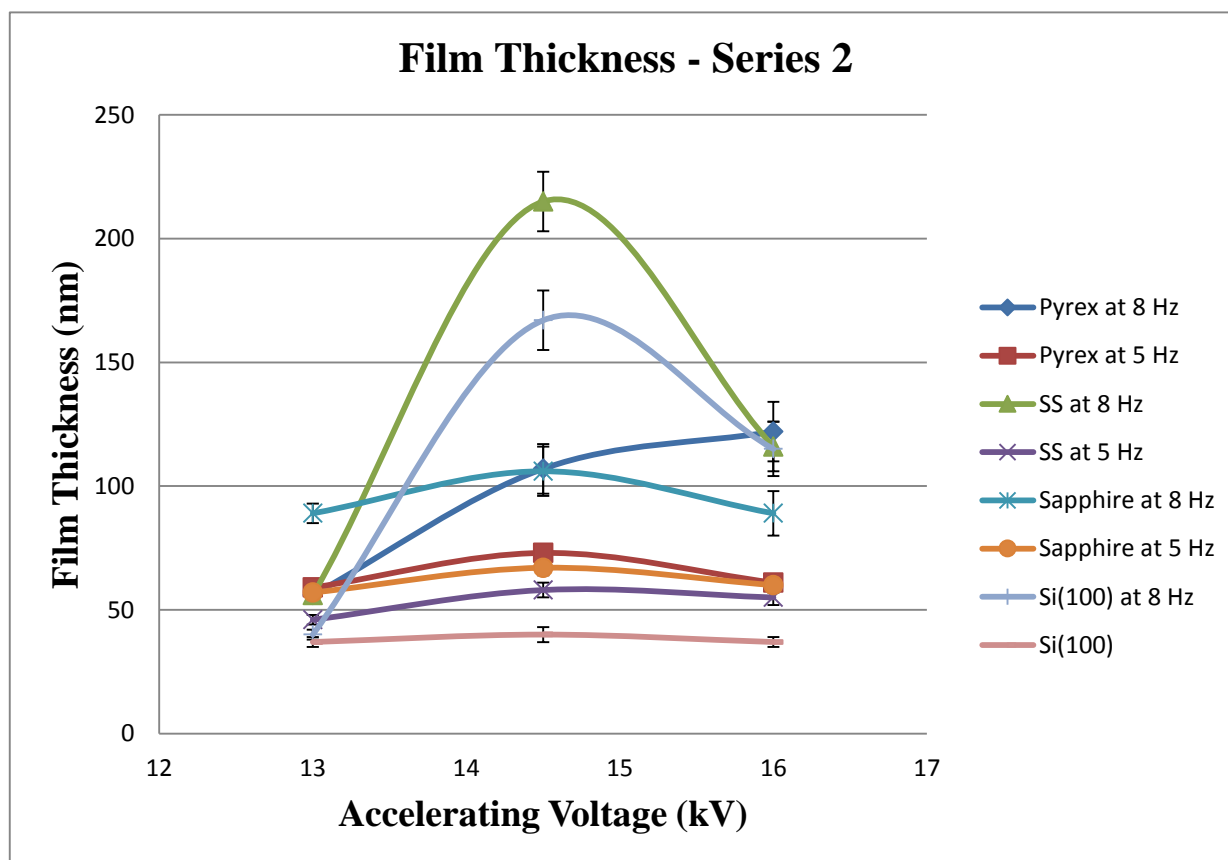


Figure 5.25: Film thickness of NCD films resulting from the second series. The solid lines are guides for the eye.

#### 5.4.2 Crystal Size, $sp^3$ Content and Nanocrystallinity

Raman spectra have been collected within the range  $1000\text{--}2000\text{ cm}^{-1}$ , for all samples. The recorded Raman spectra of deposited films, as listed in Tables 5.3A and 5.3B, are composed of the typical features of NCD. These features can be clearly distinguished after the deconvolution (using a mixed Gaussian-Lorentzian function, in this case) of the entire band and extraction of the baseline, as shown in Fig. 5.26 – 5.31 for all NCD films resulting from series 2. The deconvoluted spectrum consists of many signals, which have been mentioned in section 5.2.2. The fraction of  $sp^3$  carbon bonded atoms in the nanocomposite is calculated using Equation (5.1) (Ballutaud et al., 2008) as before. The nanocrystalline percentage in the films has been inferred by calculating the ratio  $((I_{1332} + I_{1150})/\Sigma(I))$  (Popov et al., 2007), where the sum is over the entire spectrum. The crystal size could be estimated as  $I_{1332}/I_{1150}$  (Klauser et al., 2010). The calculated values of the  $sp^3\%$ , nanocrystalline percentage and crystal size are shown in Fig. 5.32, Fig. 5.33, and Fig. 5.34, respectively.

**Table 5.3 A: Results of Raman spectra deconvolution of all NCD films resulting from the second series at 8 Hz.**

Process Conditions	Sample	$I_G$	$I_{G'}$	$I_{1332}$	$I_D$	$I_{1150}$	$I_{1250}$	$I_{1480}$
8 Hz & 14.5 kV	Pyrex	1441	1895	1096	1688	324	600	2260
	S.S.	815	890	910	403	204	455	2188
	Si(100)	390	198	310	150	80	185	829
	Sapphire	648	NA	242	268	72	155	759
8 Hz & 16 kV	Pyrex	938	1539	613	680	309	663	1563
	S.S.	1233	121	450	437	202	374	478
	Si(100)	599	1460	786	379	353	563	1807
	Sapphire	708	1628	655	670	355	560	2300
8 Hz & 13 kV	Pyex	1188	NA	277	490	154	410	454
	S.S.	9069	NA	2445	5314	1159	3320	1173
	Si(100)	3413	NA	925	1010	465	1300	893
	Sapphire	4223	NA	1100	1820	588	1336	2720

**Table 5.3 B: Results of Raman spectra deconvolution of all NCD films resulting from the second series at 5 Hz.**

Process Conditions	Sample	I <sub>G</sub>	I <sub>G'</sub>	I <sub>1332</sub>	I <sub>D</sub>	I <sub>1150</sub>	I <sub>1250</sub>	I <sub>1480</sub>
5 Hz & 14.5 kV	Pyrex	1618	1827	651	1032	384	806	839
	S.S.	662	1993	663	355	390	701	1340
	Si(100)	558	1152	447	434	262	602	1233
	Sapphire	1758	NA	508	1036	308	650	1450
5 Hz & 16 kV	Pyrex	728	3031	416	1037	270	658	1026
	S.S.	1253	540	432	527	264	734	1678
	Si(100)	1681	NA	345	987	210	690	1145
	Sapphire	716	1549	556	749	335	606	1590
5 Hz & 13 kV	Pyrex	2052	1415	440	1219	360	520	450
	S.S.	7569	NA	1443	4591	1152	3083	6185
	Si(100)	1268	2573	651	1271	478	1200	1860
	Sapphire	1880	NA	414	1072	288	862	650

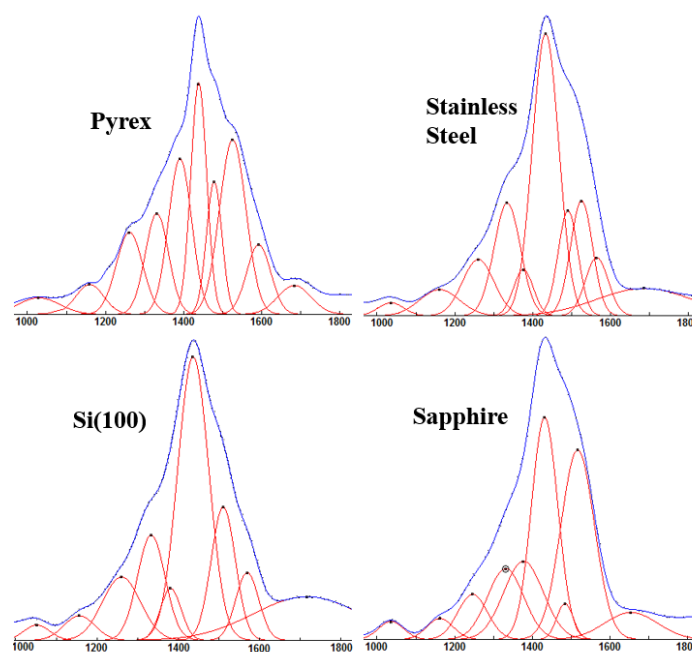


**Figure 5.26: Raman spectra (and their deconvolution) of NCD films on various substrates resulting from the second series - 14.5 kV and 8 Hz.**

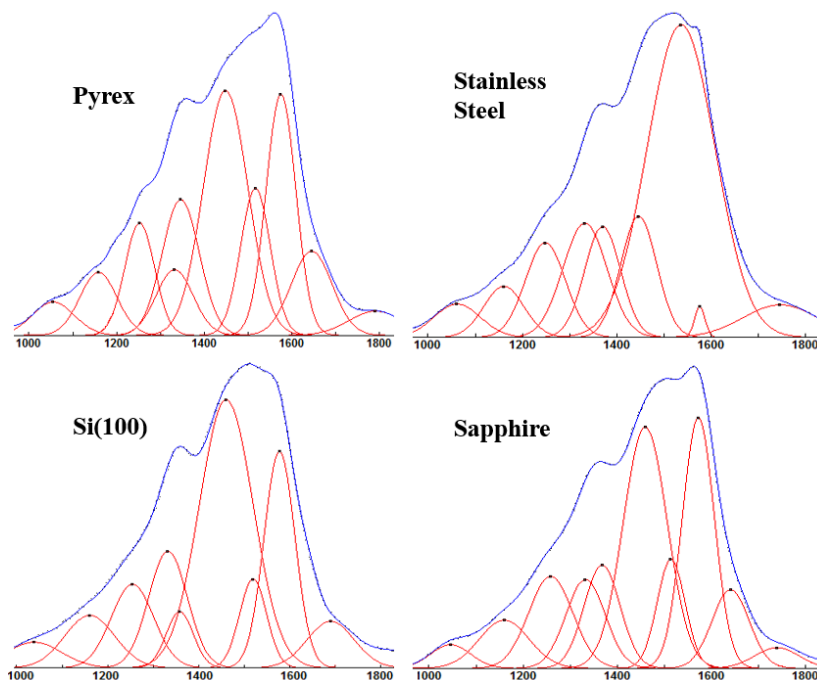


**Figure 5.27: Raman spectra (and their deconvolution) of NCD films on various substrates resulting from the second series – 16 kV and 8 Hz.**

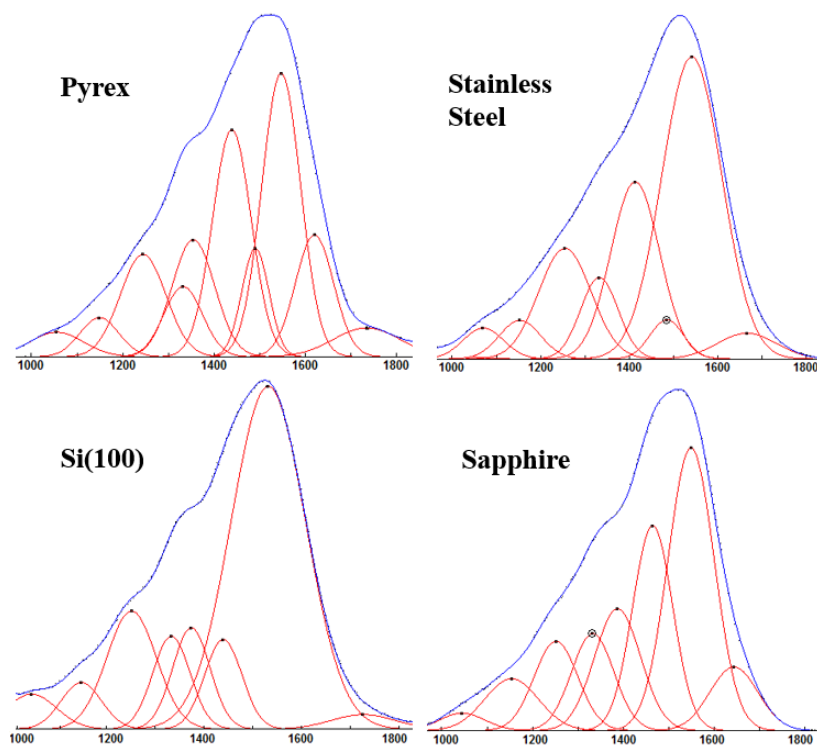


**Figure 5.28: Raman spectra (and their deconvolution) of NCD films on various substrates resulting from the second series - 13 kV and 8 Hz.**

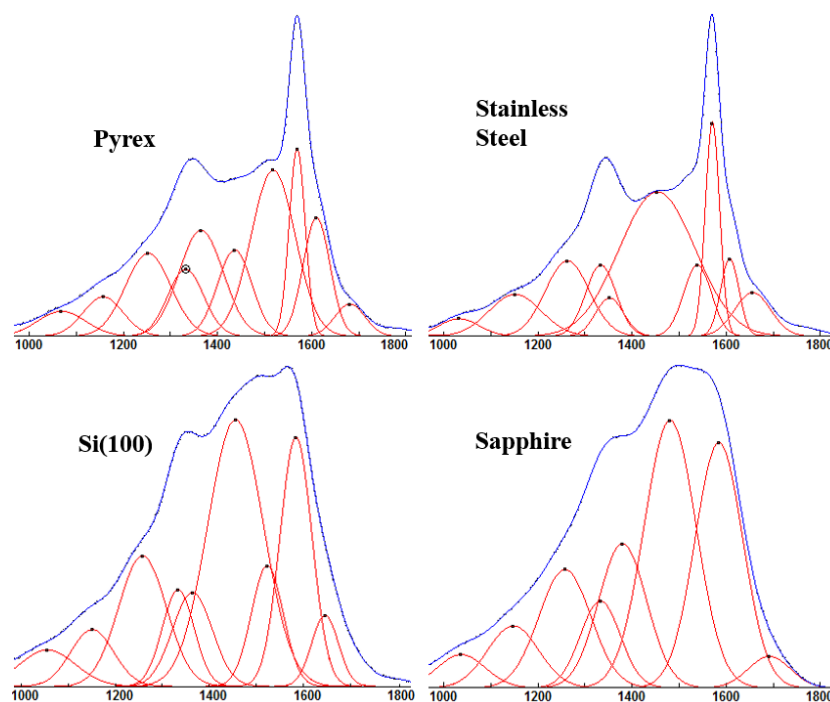


**Figure 5.29: Raman spectra (and their deconvolution) of NCD films on various substrates resulting from the second series - 14.5 kV and 5 Hz.**

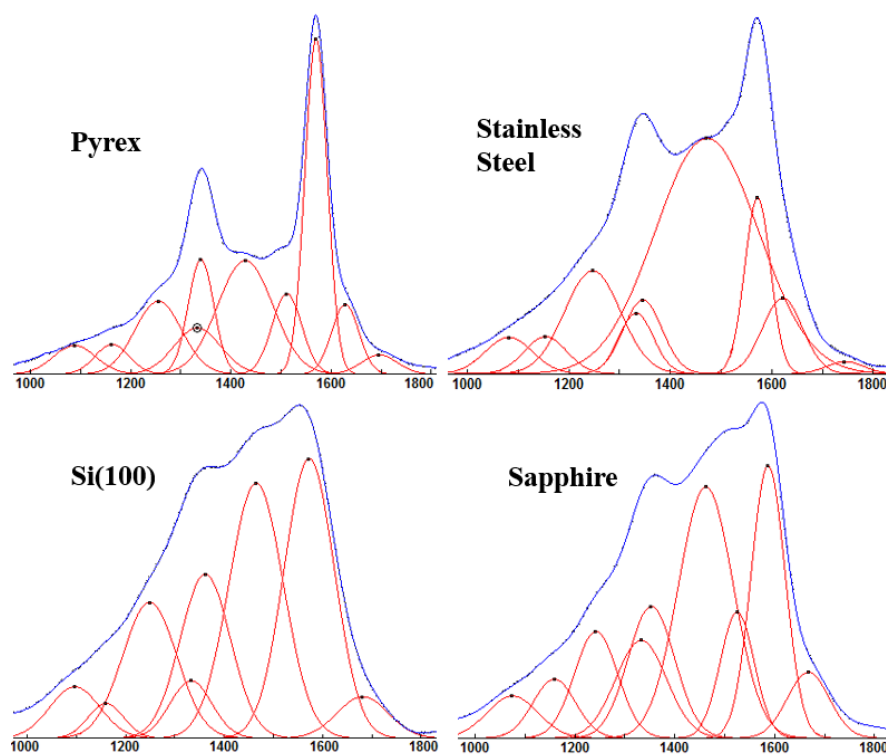


**Figure 5.30: Raman spectra (and their deconvolution) of NCD films on various substrates resulting from the second series - 16 kV and 5 Hz.**

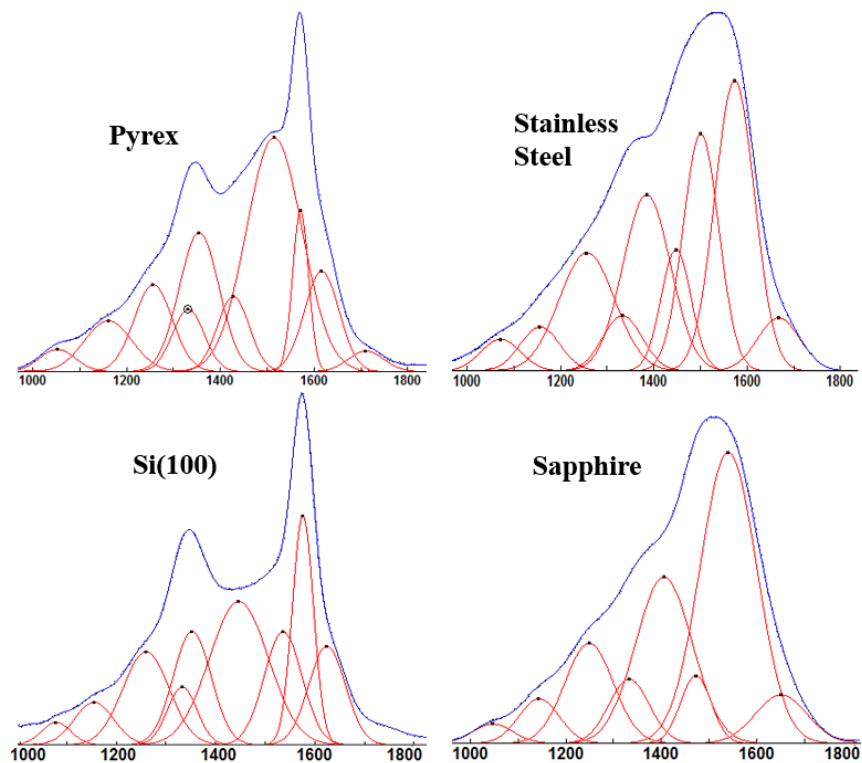


**Figure 5.31: Raman spectra (and their deconvolution) of NCD films on various substrates resulting from the second series - 13 kV and 5 Hz.**

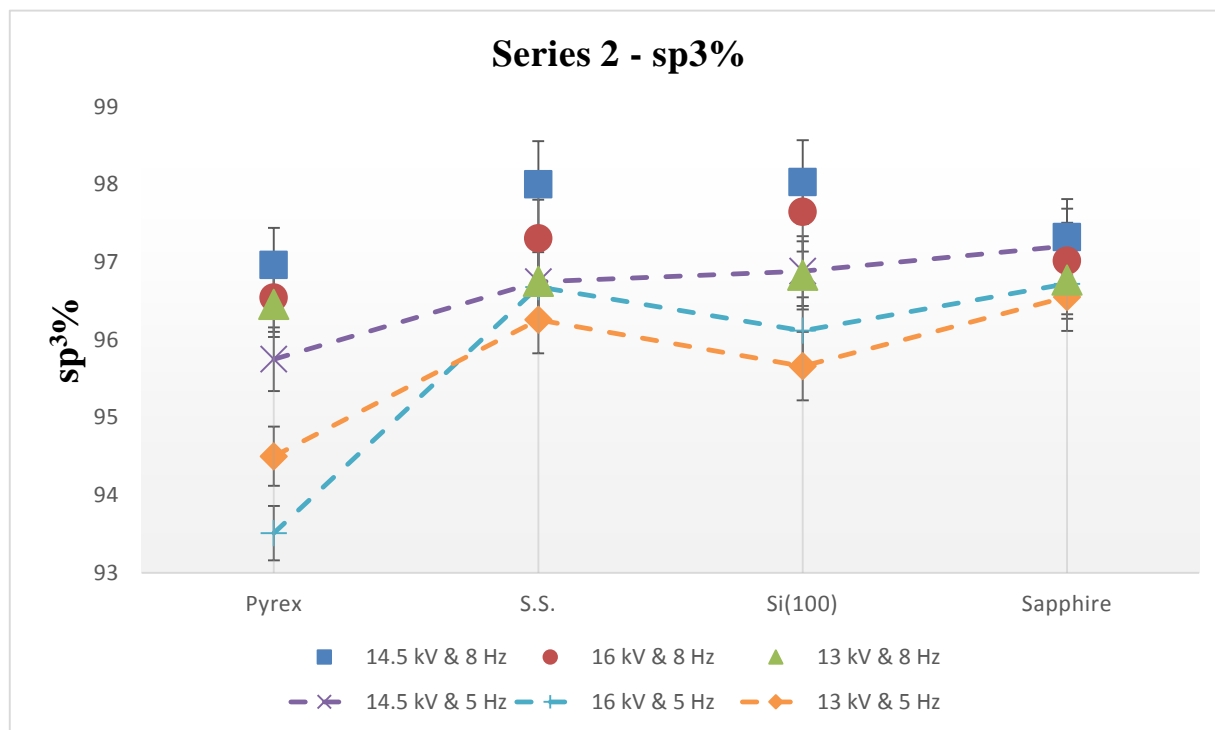


**Figure 5.32:  $sp^3$  percentage in films resulting from the second series**

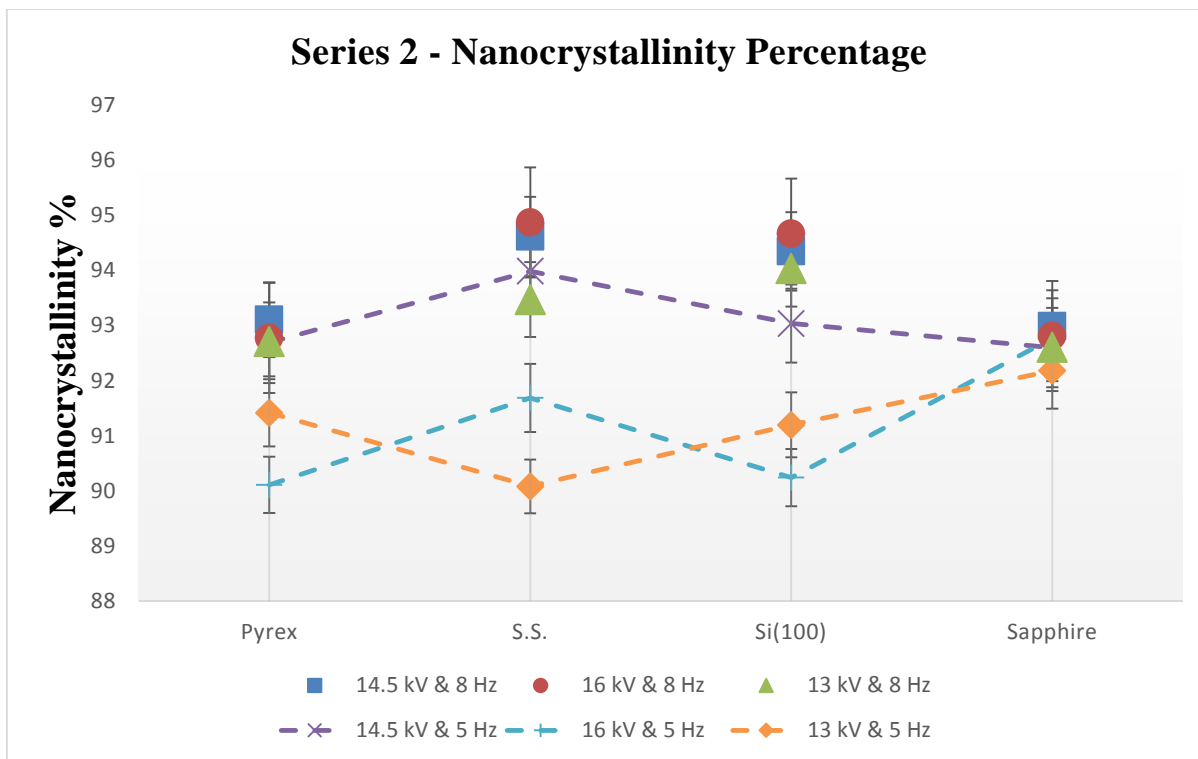


Figure 5.33: Nanocrystallinity percentage in films resulting from the second series.

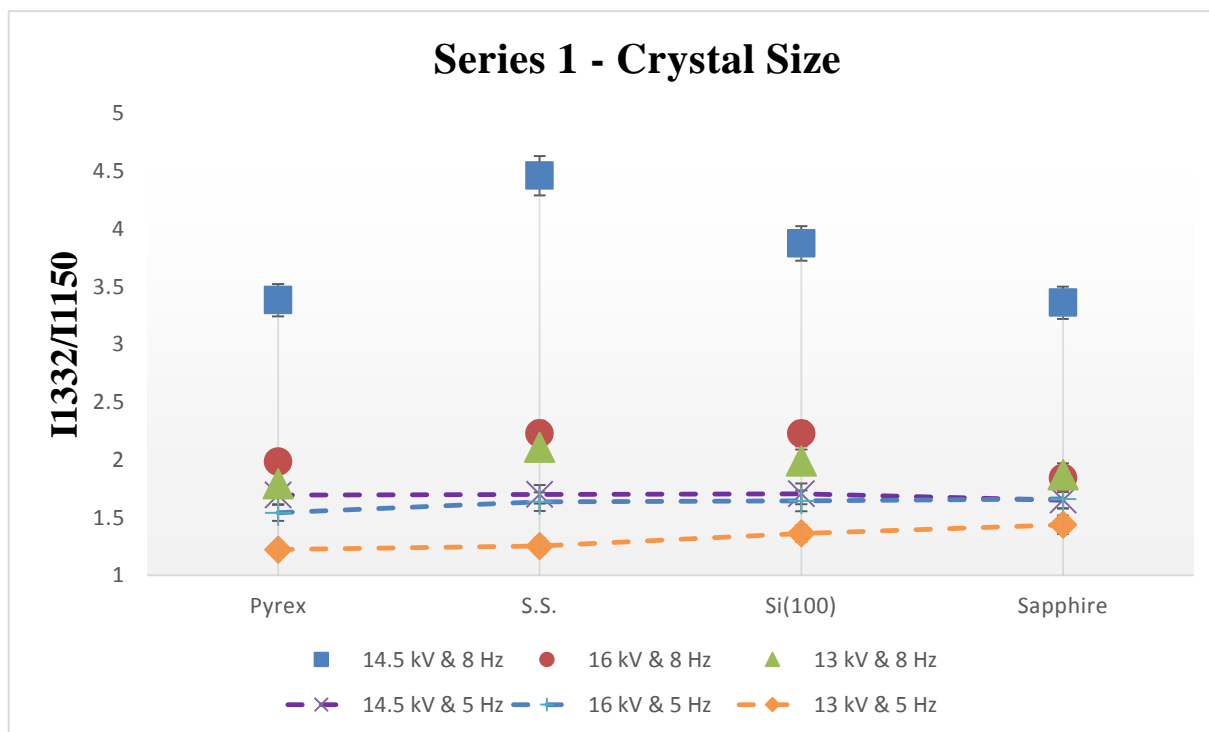
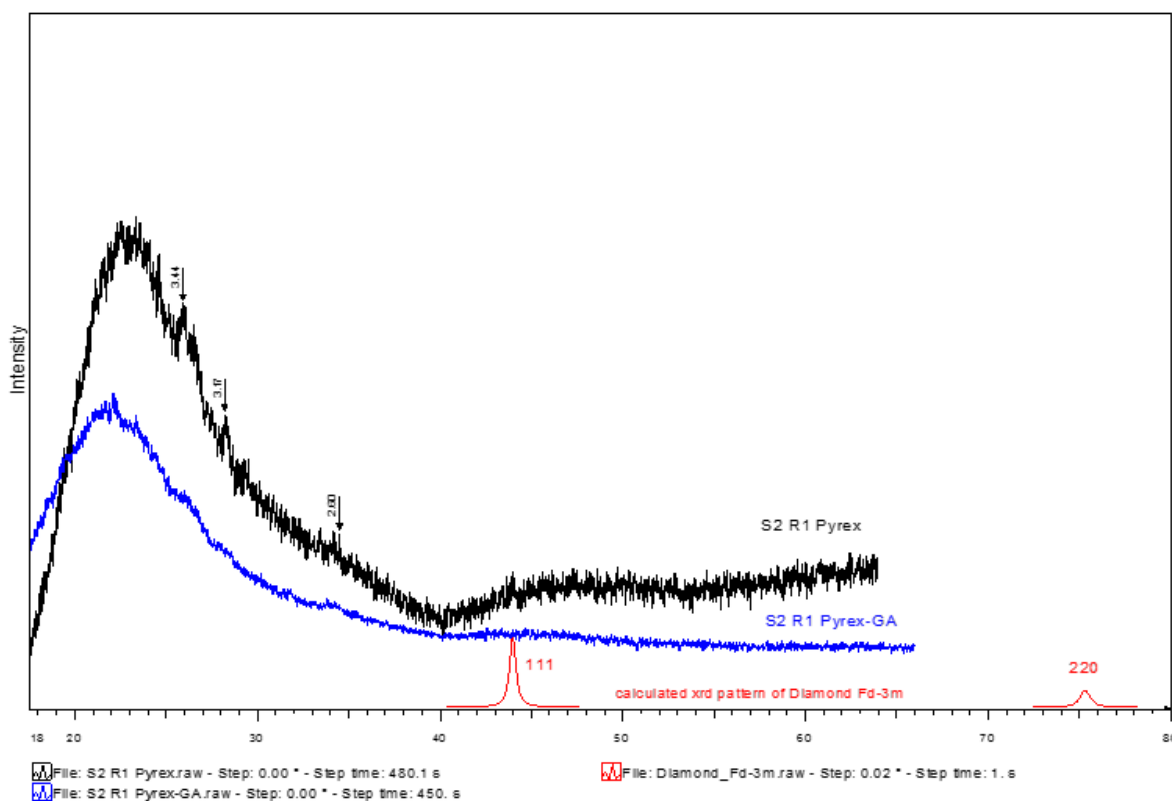


Figure 5.34: Crystal size in films resulting from the second series.

### 5.4.3 XRD Results

Figure 5.35 illustrates the diffraction behavior of the film deposited on pyrex and corresponding to series 2 at 8 Hz and 14.5 kV. On the bottom of each plot the calculated xrd pattern of diamond is recorded in red showing the two diffraction peaks at (111) and (220).

Under both normal and grazing angle ( $2^\circ$ ) modes, there are no clear diffraction peaks that can provide any compositional and/or structural information about the deposited films. This is apparently, because the films are too thin and do not have the necessary volume that can diffract. The x-ray linear mass absorption coefficient of carbon with the structure of diamond is  $12 \text{ g/cm}^{-1}$ , which means that the depth of penetration of x-rays required for approx. 70-80% intensity of diffraction intensity is  $250 - 300 \text{ }\mu\text{m}$ . It is clear that films with thickness in the nano-scale range would not diffract enough for corresponding xrd peaks to be detectable. The applied grazing angle geometry (“GA” as noted in Fig. 5.35) does not provide any visible diffraction as well.



**Figure 5.35: PXRD patterns of NCD on Pyrex resulting from the second series – 8 Hz & 14.5 kV. Normal  $\theta/2\theta$  reflection mode scan (black) and “GA” (blue) – grazing angle geometry applied with  $\theta = 2^\circ$ .**

#### 5.4.4 Film Morphology

The morphology of films resulting from series 2 as revealed by AFM analysis, and depicted in Fig. 5.36-5.41, consists of clusters of crystallites with size in the range of  $\sim 20$  nm – 200 nm.

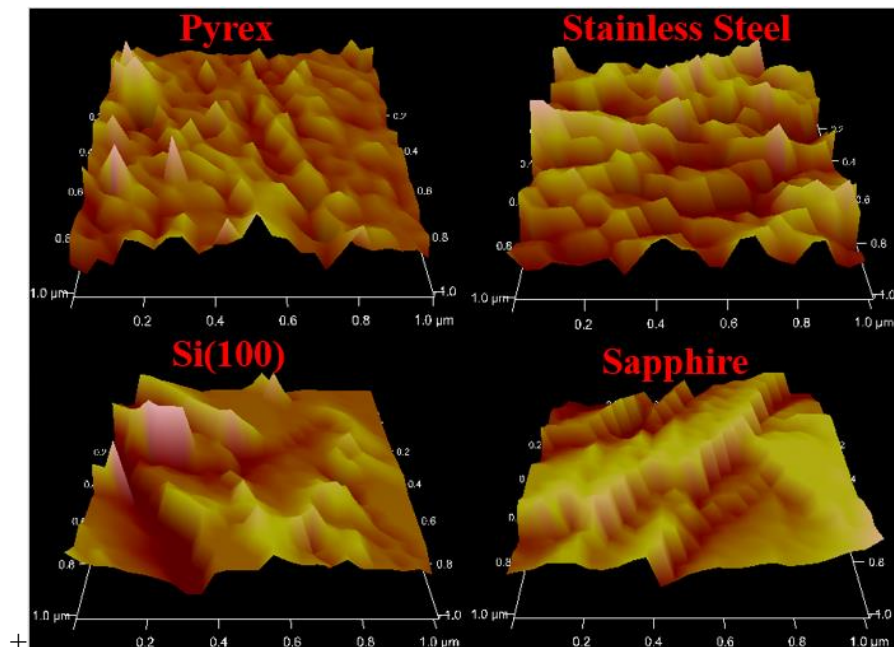


**Figure 5.36:** AFM three-dimensional view of film morphology of NCD films resulting from the second series – 8 Hz & 14.5 kV. Four different substrates are shown.

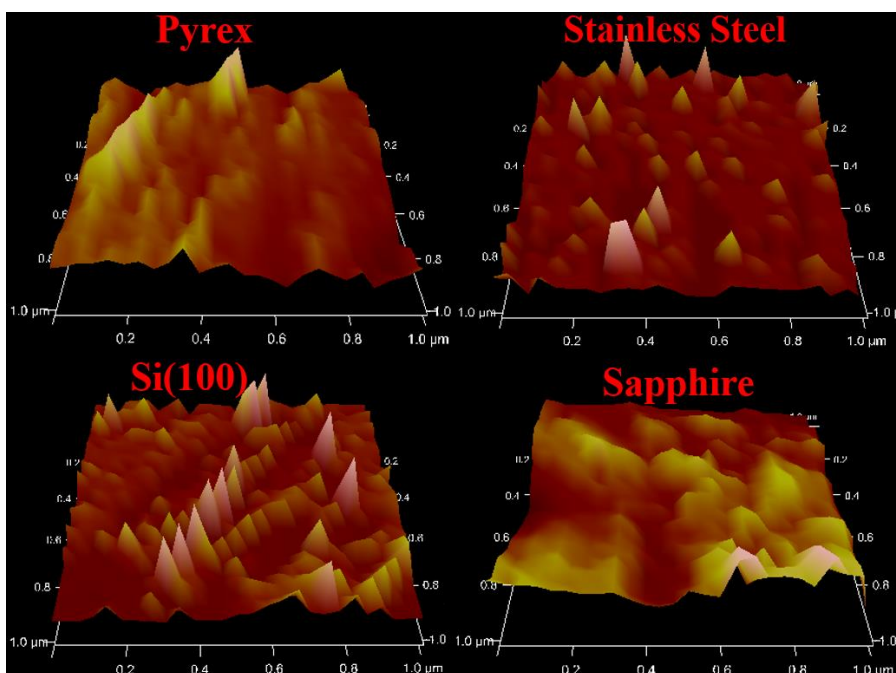


**Figure 5.37:** AFM three-dimensional view of film morphology of NCD films resulting from the second series – 8 Hz & 16 kV. Four different substrates are shown.

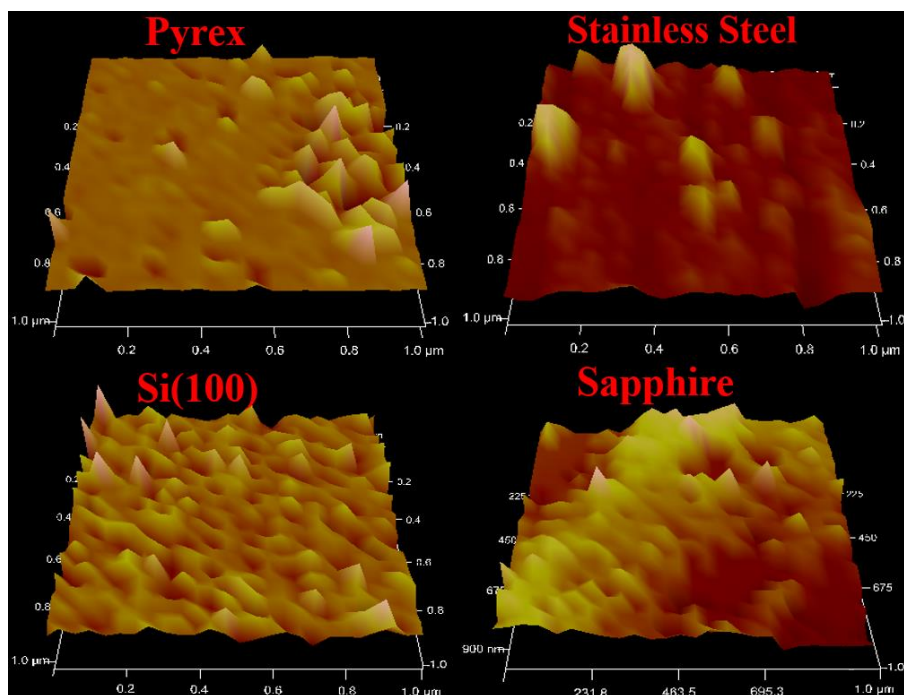


**Figure 5.38:** AFM three-dimensional view of film morphology of NCD films resulting from the second series – 8 Hz & 13 kV. Four different substrates are shown.

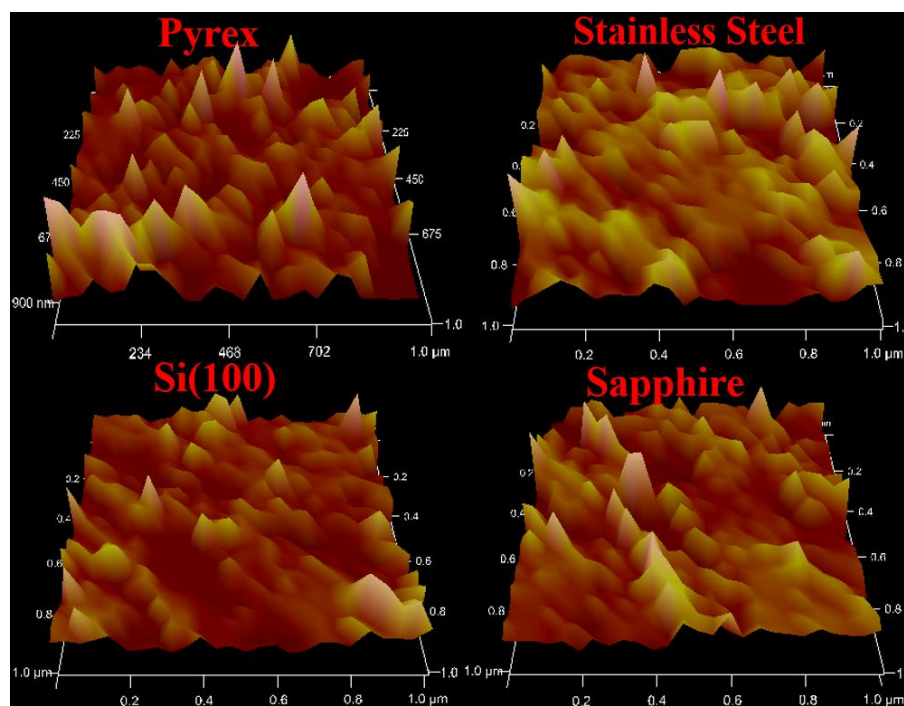


**Figure 5.39:** AFM three-dimensional view of film morphology of NCD films resulting from the second series – 5 Hz & 14.5 kV. Four different substrates are shown.

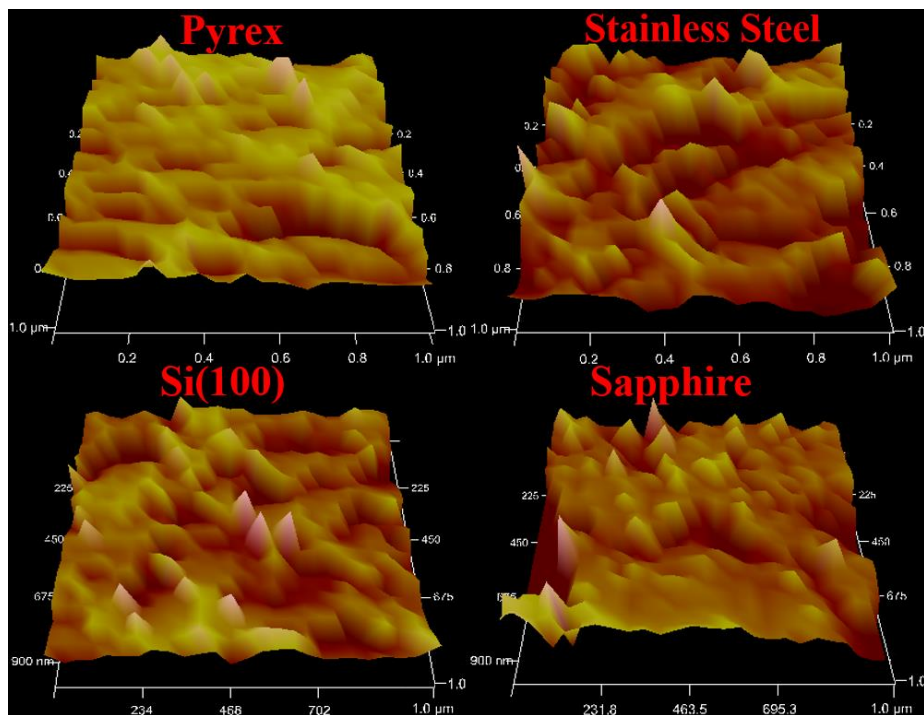


**Figure 5.40:** AFM three-dimensional view of film morphology of NCD films resulting from the second series – 5 Hz & 16 kV. Four different substrates are shown.

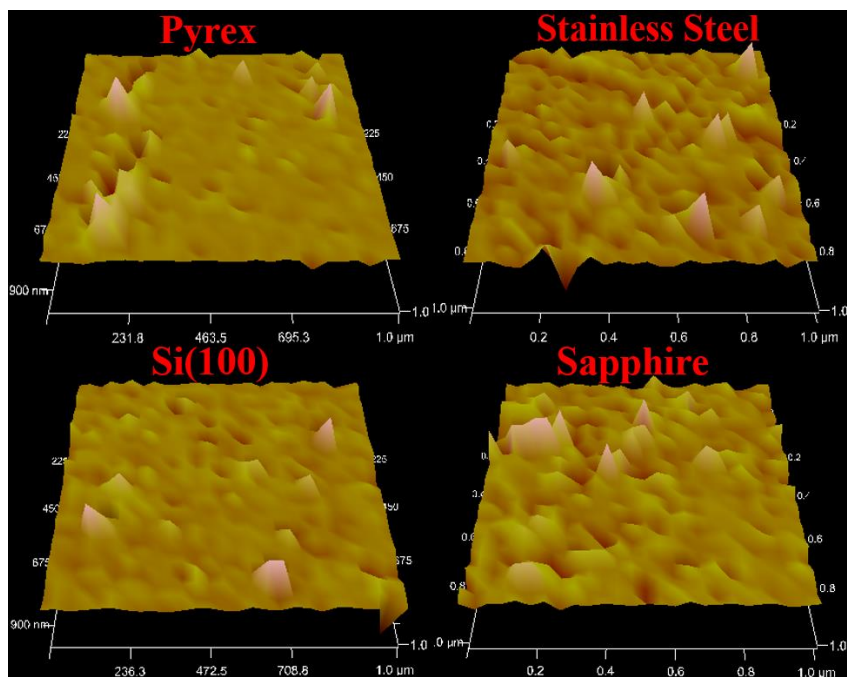


**Figure 5.41:** AFM three-dimensional view of film morphology of NCD films resulting from the second series – 5 Hz & 13 kV. Four different substrates are shown.

Moreover, typical SEM images, as shown in Fig. 5.42, of NCD films on Si(100) reveal variations in the morphology of films deposited in series 2.

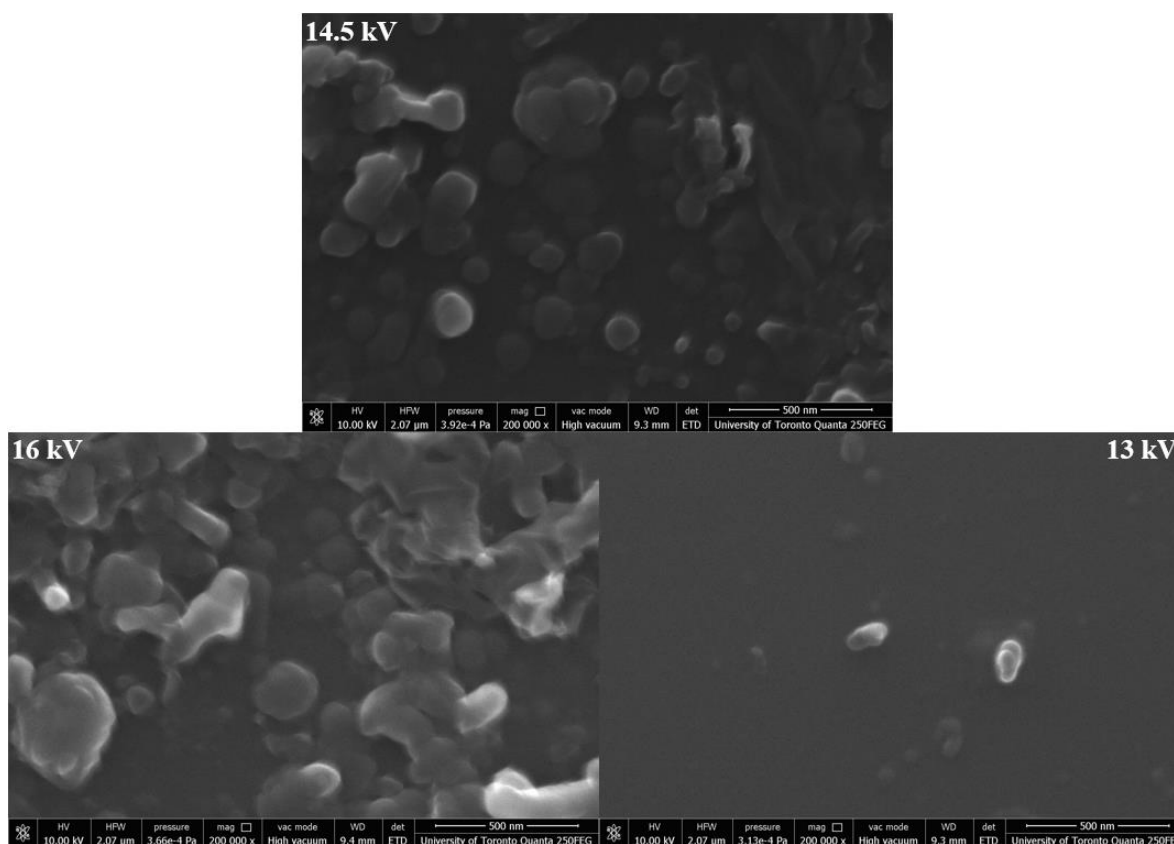


**Figure 5.42: SEM images of Si(100) films resulting from the second series at 5 Hz.**

#### 5.4.5 Film Hardness

Results of film hardness on various substrates (at 5 and 8 Hz, 14.5 and 16 kV) are summarized in Table 5.4. Hardness results of the aforementioned samples have been calculated for various depth of penetration ( $h_{max}$ ) corresponding to their film thickness. These results consist of combined hardness of the whole assembly, i.e., NCD film on substrate. Values of hardness of the bare substrates, namely, Si(100), pyrex, stainless steel, and sapphire are also listed in Table 5.4. As discussed before, Equation (5.2) could be useful in order to eliminate the substrate effect and account only for NCD film hardness (Xu, 2004).

**Table 5.4: Substrate, combined, and film hardness for NCD films resulting from the second series**

Process Conditions	Sample	Film Hardness (MPa)	Combined Hardness (MPa)	Thickness (nm)	Substrate Hardness (Mpa)
8 Hz & 14.5 kV	Pyrex	20551	20512	107	3500
	S.S.	19670	19254	215	2500
	Si(100)	19394	19247	167	8000
8 Hz & 16 kV	Pyrex	20375	20333	122	3500
	S.S.	19522	19100	116	2500
	Si(100)	19335	19182	115	8000
5 Hz & 14.5 kV	Pyrex	19867	19824	73	3500
	S.S.	19004	18595	58	2500
	Si(100)	18627	18421	40	8000
5 Hz & 16 kV	Pyrex	19732	19685	61	3500
	S.S.	18646	18202	55	2500
	Si(100)	18376	18226	37	8000

## 5.5 Discussion of the Results of the Second Series

The resulting films have a thickness in the range of 40 nm – 215 nm, as shown in Fig. 5.25. The recorded Raman spectra of the deposited films are composed of the typical features of NCD, as discussed in section 3.4.2, Chapter 3. The films exhibit  $sp^3$  in the range of 93.5% - 98.0%, as shown in Fig. 5.32. Film nanocrystallinity percentage is in the range between 90.1% and 94.9%, as depicted in Fig. 5.33, and crystal size is in the range of 4.5 – 1.2, as shown in Fig. 5.34. The morphology of the films as revealed by SEM (Fig. 5.42) and AFM (Fig. 5.36 - 5.41) consists of clusters of crystals (grains) with size in the range of ~20 nm to ~200 nm. The hardness of the films is within the range of 18.2 GPa – 20.5 GPa, as listed in Table 5.4, which is consistent with the microhardness of NCD films reported in open literature, see Table 2.1, Chapter 2.

### 5.5.1 Effect of Accelerating Voltage

At the frequency of 8 Hz, the thickness of films deposited at 14.5 kV is largest, followed by films deposited at 16 kV, and by films obtained at 13 kV (thinnest) as shown in Fig. 5.25. In terms of the accelerating voltage, the trend of film thickness of samples resulting at 8 Hz is consistent with the trend of the target heating rate depicted in Fig. 4.2. However, film on pyrex does not follow this trend. Thickness of films deposited on this substrate at 16 kV is largest, followed by films deposited at 14.5 kV, and by films deposited at 13 kV (thinnest). At 5 Hz, there does not seem to be a substantial effect of accelerating voltage on film thickness. At high pulse repetition rate, the time between two pulses is shorter and the target is cooled down (after the pulse is terminated) less deeply than at a low repetition rate. Accordingly, target heating by the next pulse starts at a higher temperature at a high repetition rate. This effect is likely due to an increase in heat accumulation rate in the target as the repetition rate is increased, resulting in a lower ablation threshold (Kim and Feit, 2000; Leme et al., 2012). The enhancement of ablation rate, which is also a function of accelerating voltage (Strikovski and Harshavardhan, 2003), at high pulse repetition rate will eventually result in a higher deposition rate and thicker films. At low repetition rate, the accelerating voltage does not seem to be able to compensate for the lower heat accumulation rate in the target.

The percentage of  $sp^3$  carbon bonded atoms in the films seems to be similar at 14.5 kV and 16 kV at 8 Hz. However, it is lower in the films deposited at 13 kV. At 5 Hz,  $sp^3\%$  in films deposited at 14.5 kV is higher relatively to films deposited at 13 kV and 16 kV, as shown in Fig. 5.32.

The magnitudes of nanocrystalline percentage in the films deposited at 14.5 kV and 16 kV appear to be very similar at 8 Hz. However, it is slightly less in the films deposited at 13 kV. At 5 Hz, the nanocrystalline percentage in films deposited at 14.5 kV is higher relatively to films deposited at 13 kV and 16 kV, as shown in Fig. 5.33.

With respect to crystal size, the latter is larger for the films obtained at 14.5 kV relatively to films obtained at 13 kV and 16 kV, at 8 Hz, as shown in Fig. 5.34. However, at 5 Hz, the crystal size seems to be similar for films deposited at 14.5 kV and 16 kV, and is smaller for films obtained at 13 kV.

The effect of the accelerating voltage on  $sp^3$  content, nanocrystalline percentage, and crystal size may be explained in terms of the dependence of the energy of the particles impinging on the substrate on accelerating voltage. High energy impinging particles have the ability to sustain highly energetic diamond nuclei on the substrate, which may lead to the formation of  $sp^3$  carbon bonded atoms in the films (Robertson et al., 2002). This is in agreement with the predictions of Strikovski's and shock wave model, see Chapter 4.

The typical morphology of the films as revealed by AFM analysis, and depicted through their 3D topography in Fig. 5.36 - 5.41, consists of pyramidal crystallites with a size in the range of ~20 nm to ~200 nm, consistent with the crystal size expected for NCD films. The clusters appear to grow along a preferential direction for all samples.

With respect to the crystal size criterion, the film deposited at 14.5 kV and 8 Hz exhibits the largest crystals. Films obtained at 16 kV show slightly larger crystals than those of films deposited at 13 kV for either repetition rate. The surface of films prepared at 13 kV (irrespective of the repetition rate) is remarkably smoother than the surface of films deposited under other conditions. The roughness of the films obtained 14.5 kV and 16 kV is practically the same irrespective of the repetition rate. The aforementioned AFM results are overall in good agreement with those obtained from Raman analysis and visible reflectance spectroscopy.

SEM images (Fig. 5.42) of NCD films deposited on silicon reveal variations in morphology as a function of accelerating voltage and pulse repetition rate. As can be seen, the crystal size of films prepared at 13 kV is smallest relatively to other films at both repetition rates. The crystal size is comparable for films obtained at 14.5 kV and 16 kV at either repetition rate. The findings are in good agreement with AFM and Raman data.

### 5.5.2 Effect of Pulse Repetition Rate

NCD films deposited at 8 Hz seem generally thicker compared to films deposited at 5 Hz, as shown in Fig. 5.26. Thicker films have been obtained at 8 Hz are due to the effect of heat accumulation, as explained in the previous section, i.e., 5.5.1.

Apparently, the fraction of  $sp^3$  carbon bonded atoms in the films seems to be higher at the pulse repetition rate of 8 Hz (in the range of ~ 96.5% - 98.0%) relatively to 5 Hz (in the range of ~ 93.5% - 97.2%), as shown in Fig. 5.32. Moreover, nanocrystallinity percentage value is overall slightly larger at the higher repetition rate (8 Hz) compared to films deposited at 5 Hz, as shown in Fig. 5.33. Also, the crystal size in NCD films obtained at 8 Hz is remarkably larger compared to films deposited at 5 Hz, as shown in Fig. 5.34. With respect to crystal size, AFM (Fig. 5.36 - 5.41) and SEM (Fig. 5.42) images are consistent with Raman analysis. The effect of the repetition rate on  $sp^3$  content, nanocrystalline percentage, and crystal size may be explained in terms of the ability to sustain highly energetic diamond nuclei on the substrate. At a high repetition rate, the short time interval between successive pulses would mean that active diamond nuclei are quickly replenished and preserve much of their high energy (part of it is released as the pulse dies out).

## 5.6 Results of Third Series

In the third series of deposition experiments, the substrates have been subjected to heat treatment. The substrates have been annealed to two different temperatures, namely, 900 °C and 1100 °C. The effect of substrate annealing temperature on the deposited NCD films has been studied. PEBA operation conditions such as pulse repetition rate, accelerating voltage, substrate temperature, substrate-target distance, and beam-target distance were fixed as 8 Hz, 14.5 kV, RT, 5 cm, 4 mm, respectively, see Chapter 3, section 3.2.2. Only three different substrate materials have been used, namely, sapphire, Si(100), and stainless steel, as the pyrex substrate melted at 900 °C. The corresponding results are given in the next sections.

### 5.6.1 Film Thickness

Figures 5.43 and 5.44 show the reflectance response, obtained from visible spectroscopy of deposited NCD films on Si(100) annealed at 900 °C and 1100 °C. The blue curve is the calculated reflectance response of the film, while the red curve is the measured one. The fit between the two curves is very good (maximum relative error of 3%). The resulting film thicknesses from all runs are plotted in Fig. 5.45.

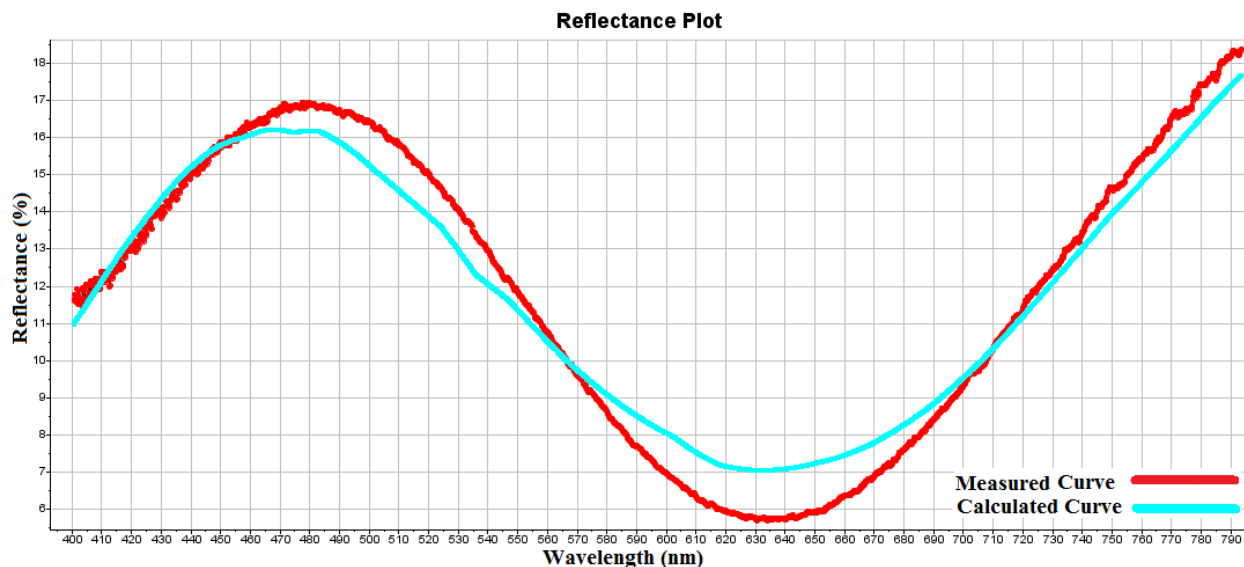


**Figure 5.43:** Visible spectroscopic reflectance of NCD film on Si(100) (annealed at 900 °C) resulting from the third series

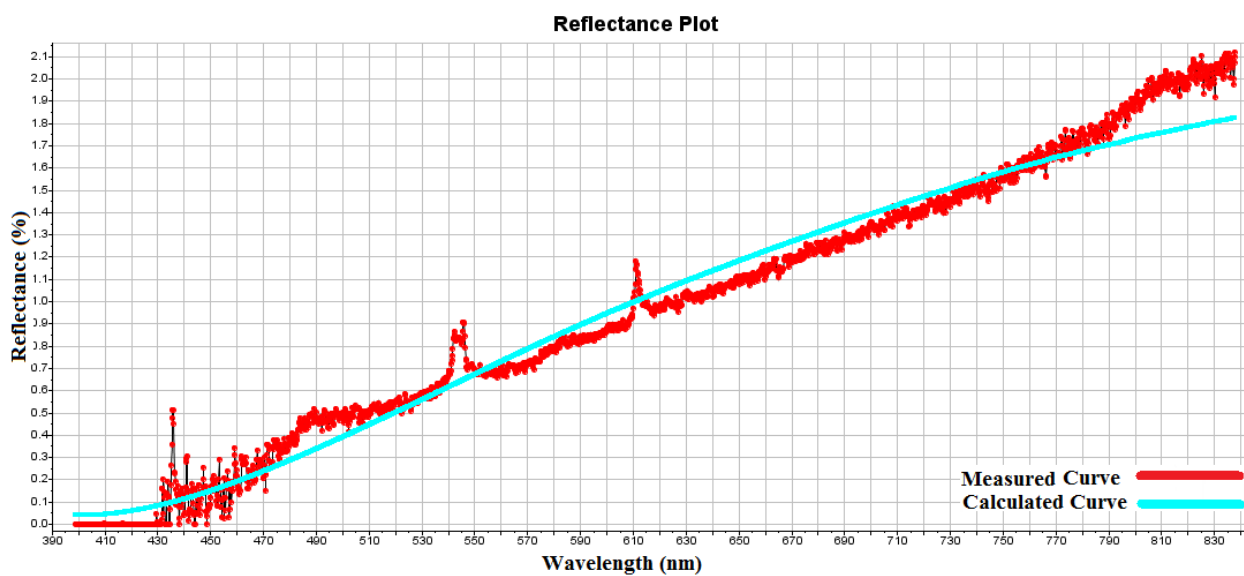


**Figure 5.44:** Visible spectroscopic reflectance of NCD film on Si(100) (annealed at 1100 °C) resulting from the third series

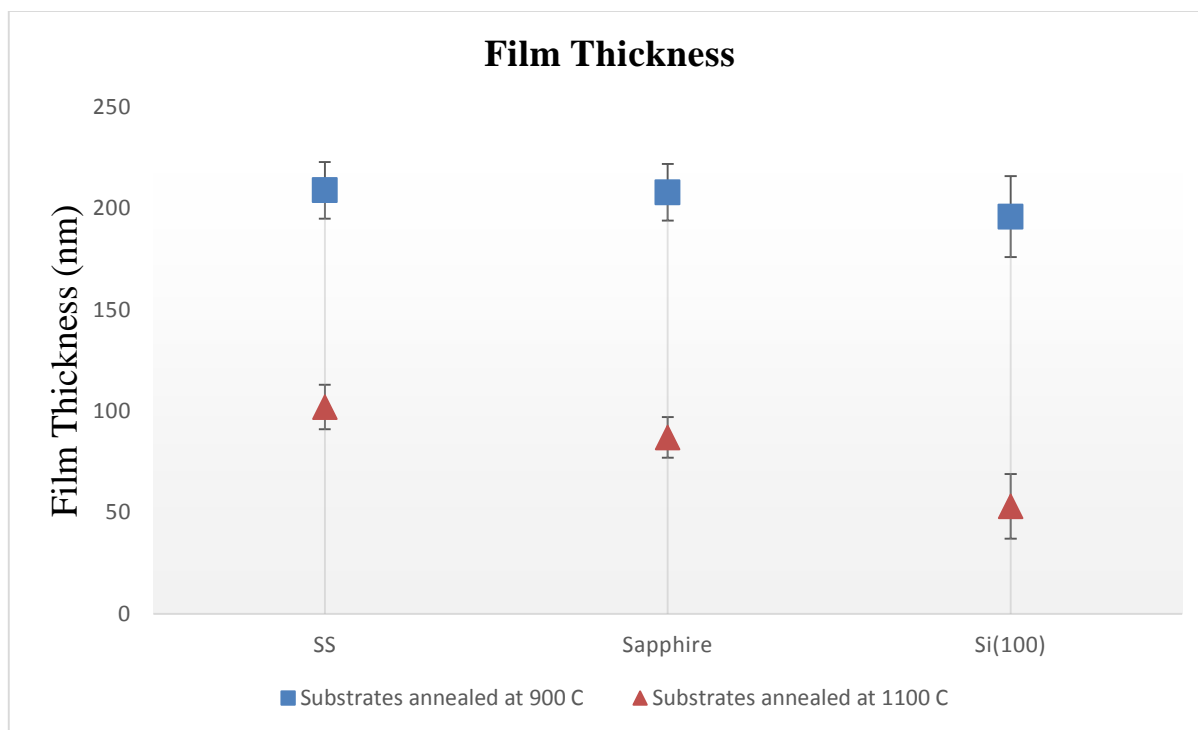


**Figure 5.45: Film thickness of NCD films resulting from the third series**

Roughness values, in terms of arithmetic mean value ( $R_a$ ), of films deposited on un-annealed substrates and on substrates annealed at 900 °C and 1100 °C are listed in Table 5.5. Films deposited on substrates annealed at 1100 °C are roughest, while the roughness values of films deposited on non-annealed substrates are lowest.

**Table 5.5: Roughness of bare substrates annealed at 900 °C and 1100 °C**

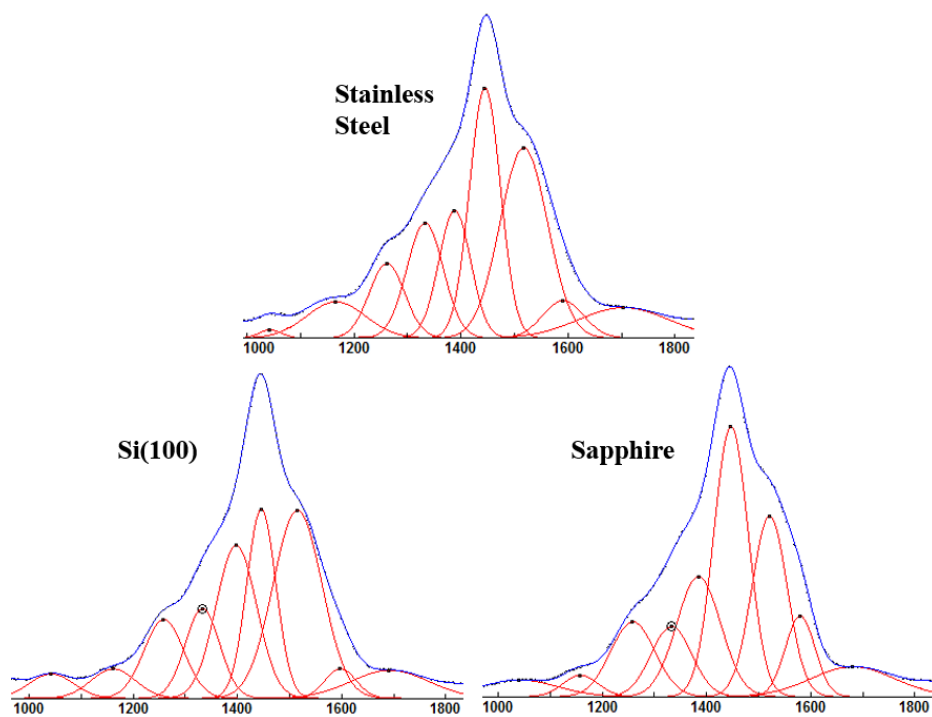
Annealing Temperature (°C)	Substrate	$R_a$ (nm)
900	SS	71.2
900	Sapphire	126.1
900	Si(100)	51.1
1100	SS	89.8
1100	Sapphire	198.1
1100	Si(100)	320

### 5.6.2 Crystal Size, $sp^3$ Content and Nanocrystallinity

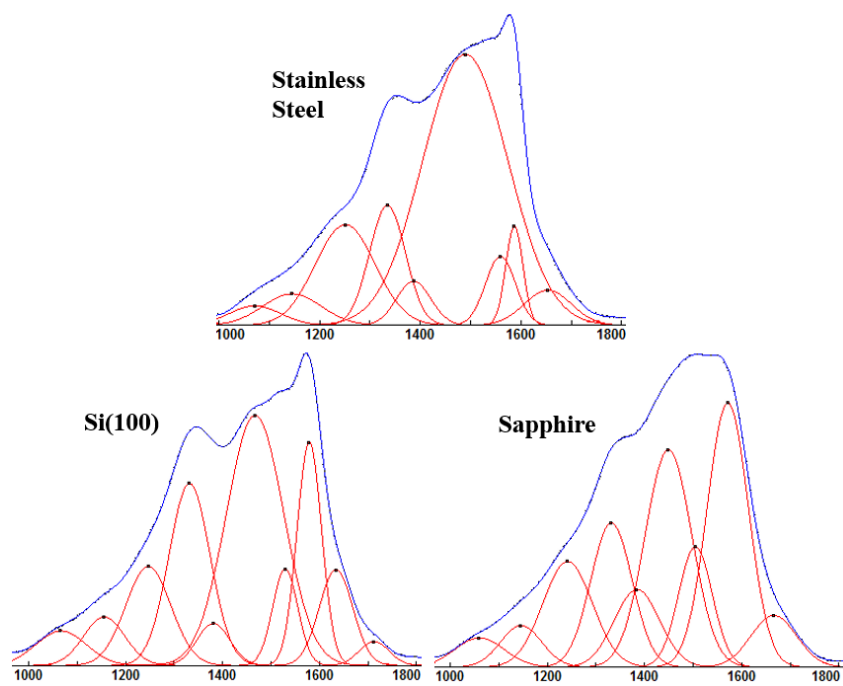
Raman spectra have been collected within the range  $1000 - 2000 \text{ cm}^{-1}$ , for all samples. The recorded Raman spectra of deposited films, as listed in Table 5.6, are composed of the typical features of NCD. These features can be clearly distinguished after the deconvolution (using a mixed Gaussian-Lorentzian function, in this case) of the entire band and extraction of the baseline, as shown in Fig. 5.46, and Fig. 5.47 for all films. The deconvoluted spectrum consists of many signals, as mentioned in section 5.2.2. The fraction of  $sp^3$  carbon bonded atoms in the nanocomposite is calculated using Equation (5.1) (Ballutaud et al., 2008) as before. The nanocrystalline percentage in the films has been inferred by calculating the ratio  $((I_{1332} + I_{1150})/\Sigma(I))$  (Popov et al., 2007), where the sum is over the entire spectrum. The crystal size could be estimated as  $I_{1332}/I_{1150}$  (Klauser et al., 2010). The calculated values of the  $sp^3\%$ , nanocrystalline percentage, and crystal size are shown in Fig. 5.48, Fig. 5.49, and Fig. 5.50, respectively.

**Table 5.6: Results of Raman spectra deconvolution of all NCD films resulting from the third series**

Deposition Conditions	Sample	$I_G$	$I_{G'}$	$I_{1332}$	$I_D$	$I_{1150}$	$I_{1250}$	$I_{1480}$
8 Hz, 14.5 kV, and substrates annealed at 900 °C	S.S.	22438	NA	13450	15055	4360	8786	29440
	Si(100)	16654	NA	7930	13536	2605	6977	16739
	Sapphire	13376	NA	5150	8388	1615	5538	19900
8 Hz, 14.5 kV, and substrates annealed at 1100 °C	S.S.	2049	2951	3572	1311	913	2990	8050
	Si(100)	1153	2677	2190	503	569	1183	2995
	Sapphire	5894	NA	3300	1732	931	2358	5140



**Figures 5.46: Raman spectra (and their deconvolution) of NCD films on various substrates (annealed at 900 °C) resulting from third series**



**Figures 5.47: Raman spectra (and their deconvolution) of NCD films on various substrates (annealed at 1100 °C) resulting from third series**

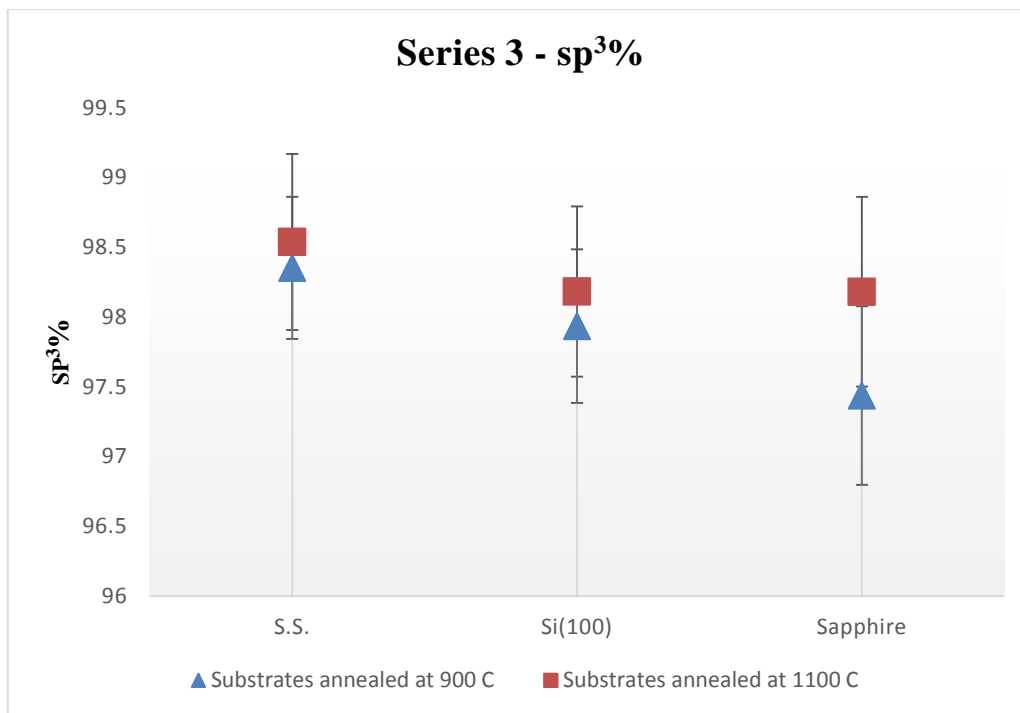


Figure 5.48:  $sp^3$  percentage in films resulting from the third series.

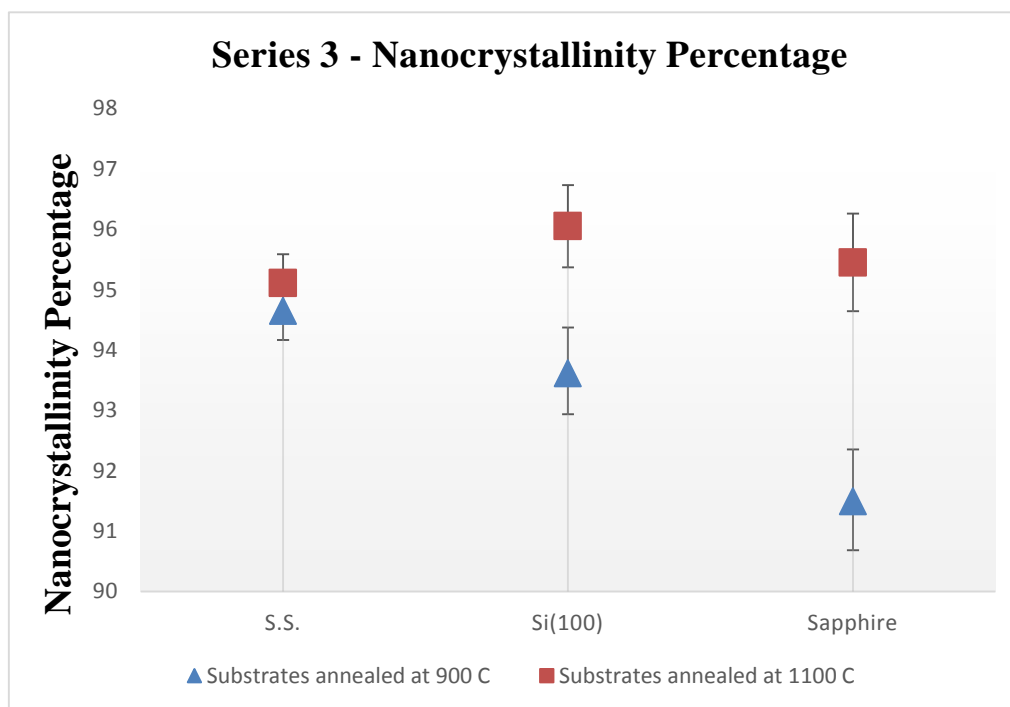
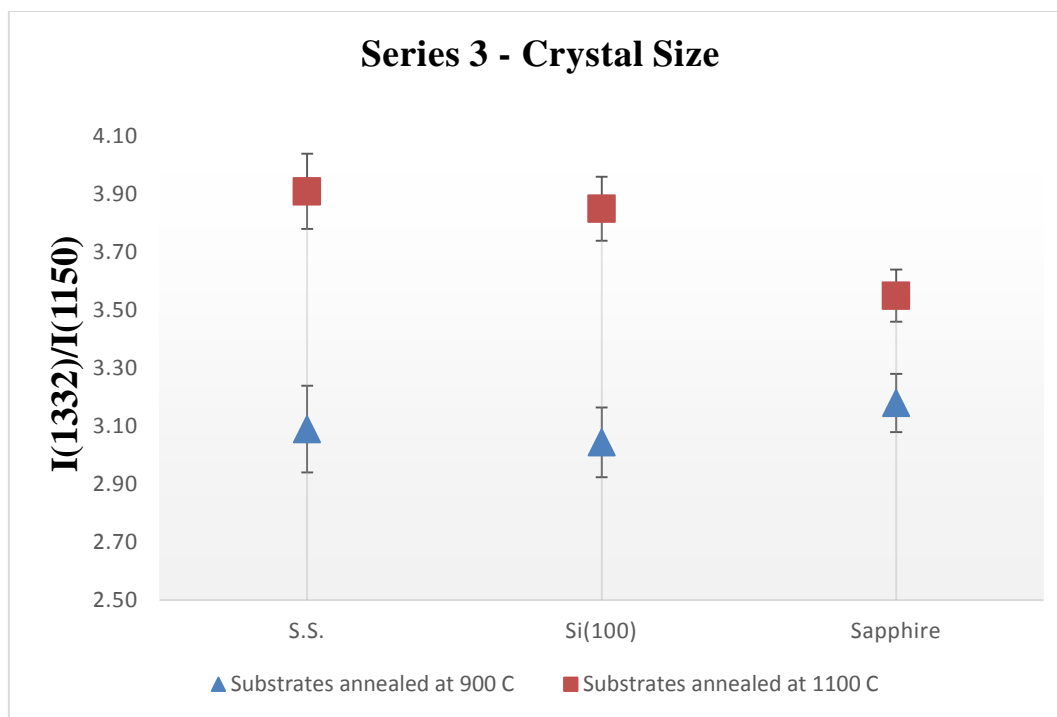


Figure 5.49: Nanocrystallinity percentage in films resulting from the third series



**Figure 5.50: Crystal size in films resulting from the third series**

### 5.6.3 Film Morphology

Figures 5.51 shows the morphology of the bare substrates namely, Si(100), stainless steel, and sapphire before annealing as revealed by AFM analysis. Figures 5.52 and 5.53 show the morphology of annealed bare substrates (same aforementioned substrates) at 900 °C and 1100 °C, respectively. As it can be observed, the surface of bare substrates annealed at 1100 °C exhibits terraces. The morphology of films deposited on annealed substrates are depicted in Fig. 5.54 and Fig. 5.55. As revealed by AFM analysis, the films consist of clusters of crystallites with submicronic size. Typical SEM images of films on Si(100), as shown in Fig. 5.56 and Fig. 5.57, also reveal variations in the morphology of films.

The bare substrates, after being ex-situ annealed at 1100 °C for 1 h, their surfaces exhibit single unit-cell stepped terraces with sharp edges and uniform widths. The atomic terraces in the annealed film surfaces turn out to be distorted and discrete (Wang et al. 2013). This drastic morphology change is depicted in Fig. 5.51, Fig. 5.52, and Fig. 5.53. Moreover, the ex-situ annealing does not only eliminate the oxygen deficiency but, more importantly, significantly improve the epitaxial quality and increased the roughness of the substrate surface, see Table 5.5.

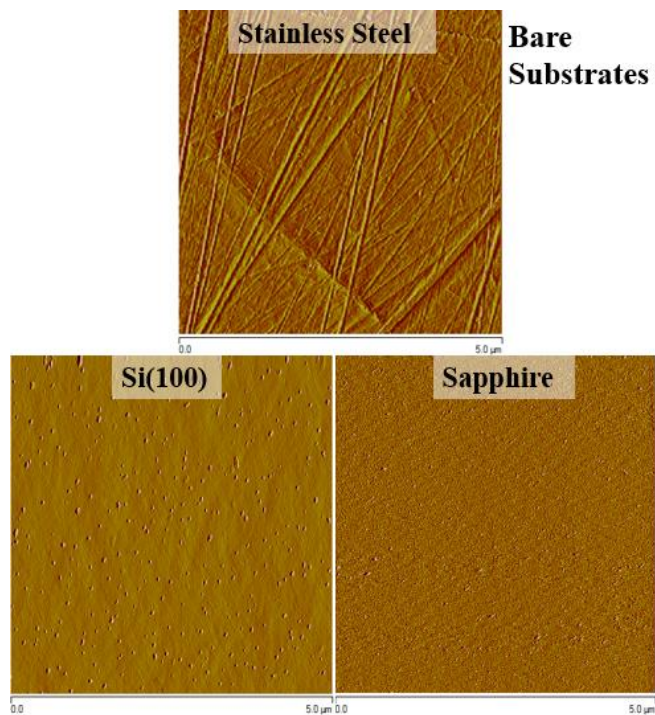


**Figure 5.51: AFM two-dimensional view of surface morphology of three different bare substrates (before annealing).**

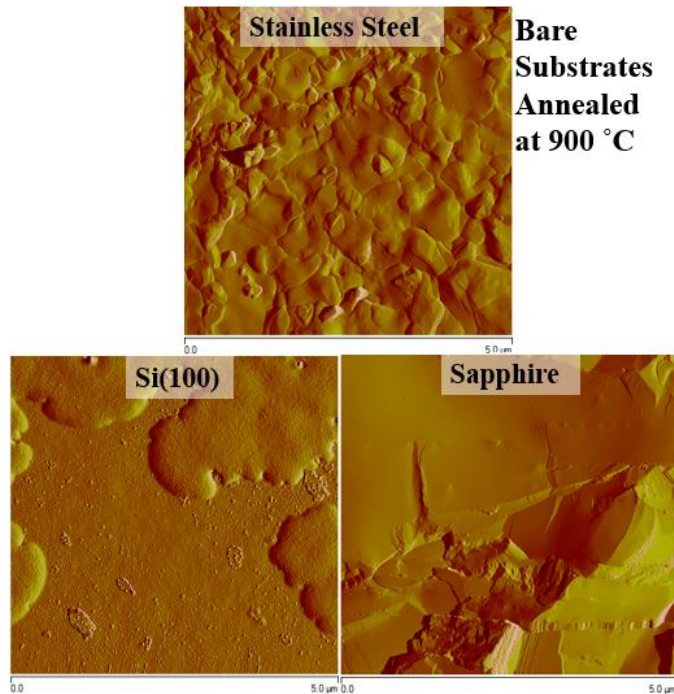


**Figure 5.52: AFM two-dimensional view of surface morphology of three different substrates (annealed at 900 °C).**

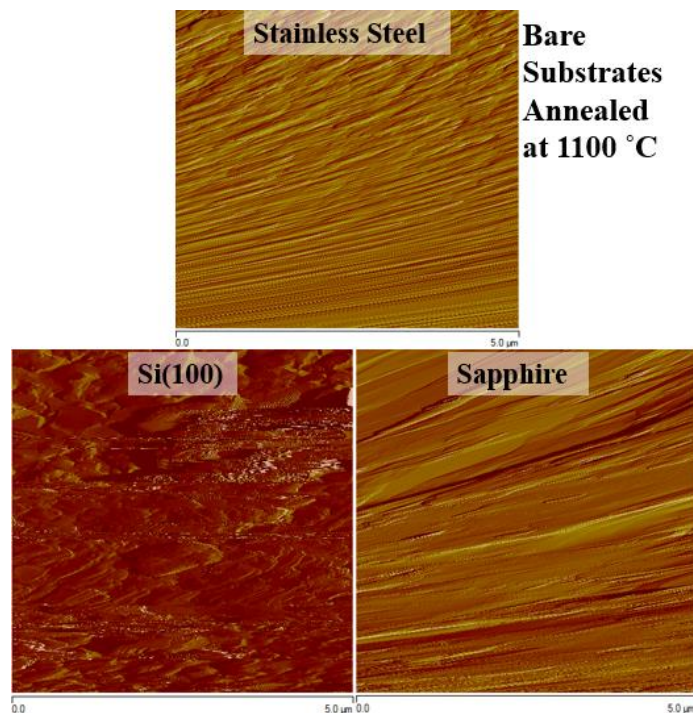


**Figure 5.53: AFM two-dimensional view of surface morphology of three different substrates (annealed at 1100 °C).**

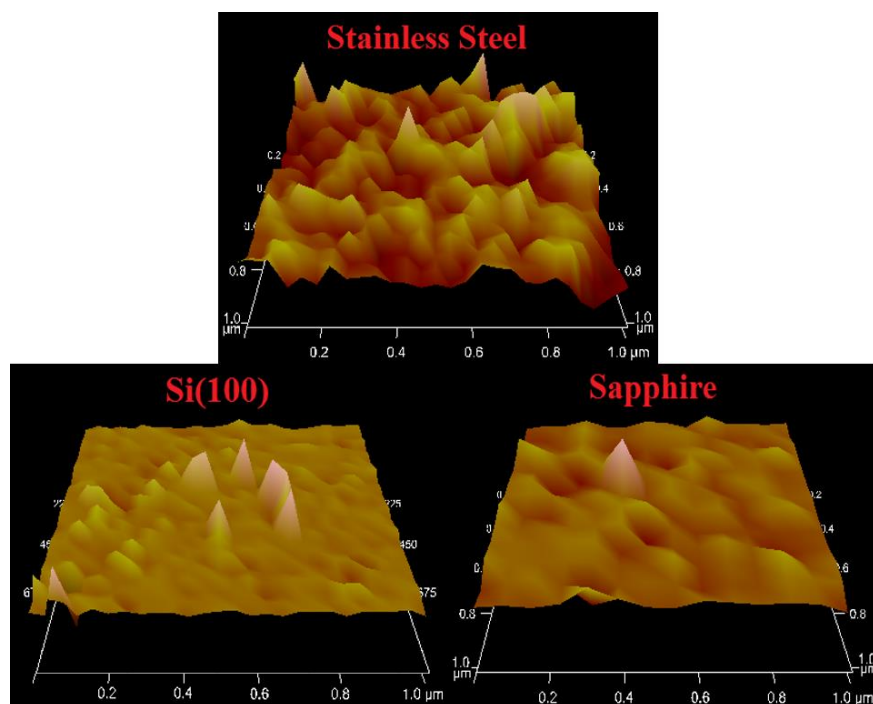


**Figure 5.54: AFM three-dimensional view of film morphology of NCD films on substrates annealed at 900 °C resulting from the third series. Three different substrates are shown.**

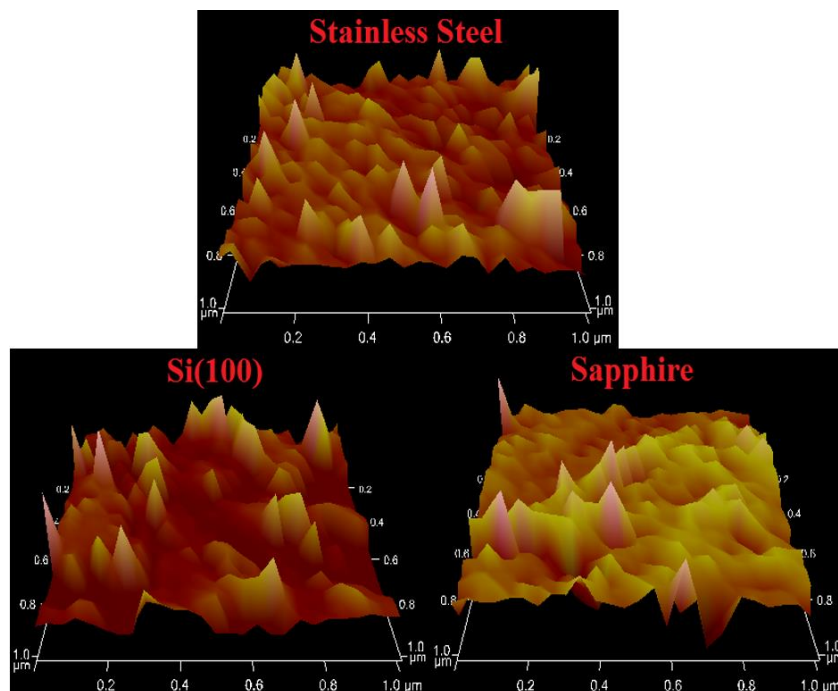


**Figure 5.55: AFM three-dimensional view of film morphology of NCD films on substrates annealed at 1100 °C resulting from the third series. Three different substrates are shown.**

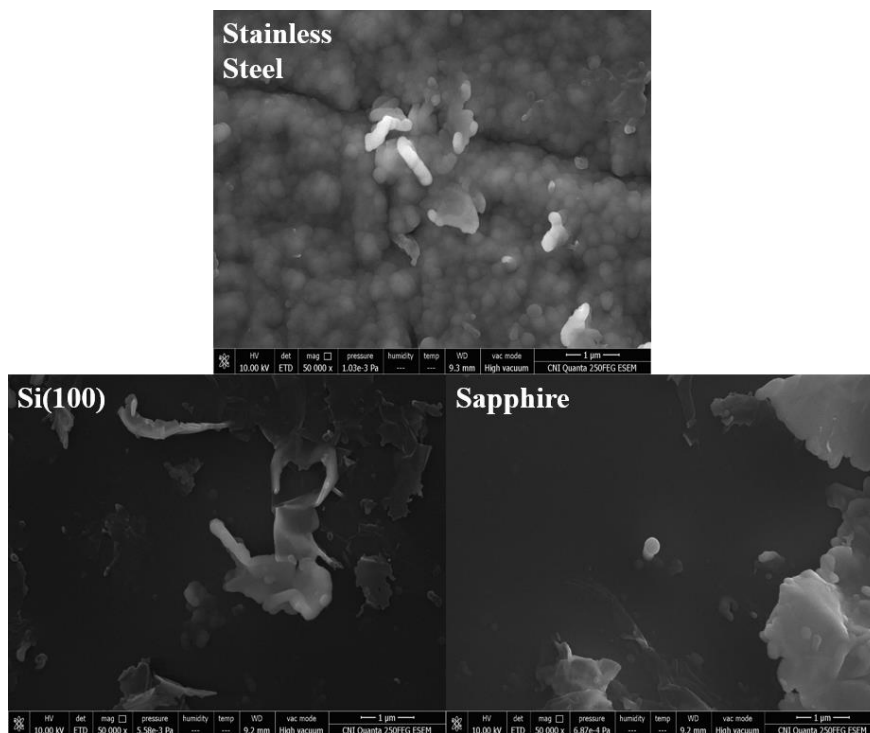


**Figure 5.56: SEM images of NCD films on substrates annealed at 900 °C resulting from the third series. Three different substrates are shown.**

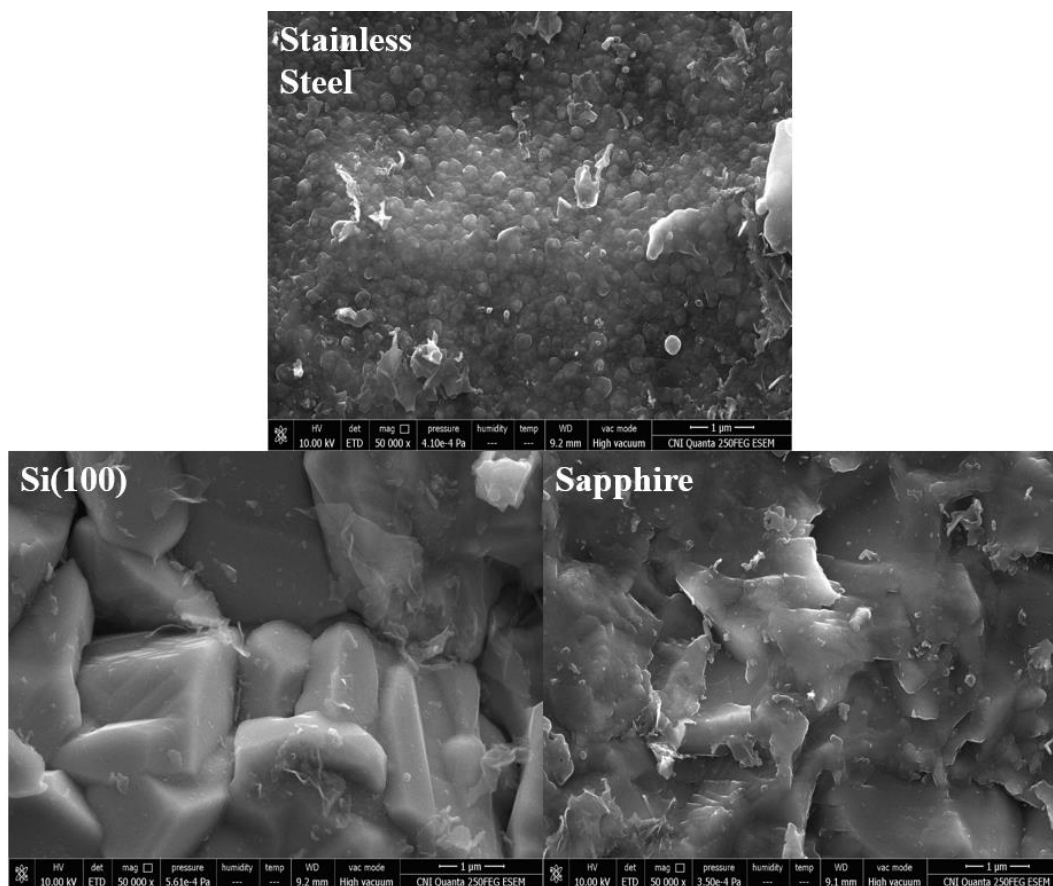


**Figure 5.57: SEM images of NCD films on substrates annealed at 1100 °C resulting from the third series. Three different substrates are shown.**

#### 5.6.4 Film Hardness

Results of films hardness, on various substrates, are summarized in Tables 5.7 and 5.8. Hardness results, of samples resulting from series 3, have been calculated for various penetration depth corresponding to their film thickness. These results consist of combined hardness of the whole assembly, i.e., NCD film on substrate. Values of hardness of the bare substrates annealed at 900 °C are listed in Table 5.7. Values of hardness of bare substrates annealed at 1100 °C are listed in Tables 5.8. Equation (5.2) has been used in order to eliminate the substrate effect and account only for NCD film hardness (Xu, 2004) as before.

**Table 5.7: Substrate, combined, and film hardness for NCD films on substrates annealed at 900 °C resulting from the third series**

<b>Sample</b>	<b>Film Hardness (MPa)</b>	<b>Combined Hardness (MPa)</b>	<b>Thickness (nm)</b>	<b>Substrate Hardness (Mpa)</b>
S.S.	19177	19140	209	2200
Si(100)	19719	19412	196	7000
Sapphire	19856	19727	208	9700

**Table 5.8: Substrate, combined, and film hardness for NCD films on substrates annealed at 1100 °C resulting from the third series**

<b>Sample</b>	<b>Film Hardness (MPa)</b>	<b>Combined Hardness (MPa)</b>	<b>Thickness (nm)</b>	<b>Substrate Hardness (Mpa)</b>
S.S.	20173	20127	102	2000
Si(100)	20722	20242	53	4500
Sapphire	20499	20346	87	9000

## 5.7 Discussion of the Results of the Third Series

The resulting films have a thickness in the range of 53 nm – 209 nm, as shown in Fig. 5.45. Films deposited on substrates annealed at 900 °C have a remarkably higher thickness (196 nm - 209 nm) compared to the ones deposited on substrates annealed at 1100 °C (53 nm – 102 nm), as shown in Fig. 5.45. Differences in film thickness between NCD films deposited on substrates annealed at 900 °C and films deposited on substrates annealed at 1100 °C seem to be due to the increase in surface roughness in substrates annealed at 1100 °C, see Table 5.5. An increase of roughness is

related to the crystallographic rearrangements such as the development of terraces and trenches on heat treated substrates (Park et al., 1999). Such changes make the annealed substrates remarkably rougher as reported in Table 5.5 and depicted in Figure 5.52 for the substrates annealed at 900 °C and Figure 5.53 for the substrates annealed at 1100 °C relatively to the non-annealed substrates (Figure 5.51). A rough surface has a higher deposition area relatively to a smooth surface, resulting in thinner films as illustrated in Fig. 5.58 (Chalermkiti et al., 2013). Hence, the differences in film thickness between films deposited on substrates annealed at 900 °C and at 1100 °C would result. The other factor that may affect the difference in thickness of films deposited at 900 °C and 1100 °C is the crystal size. As the crystal size decreases the crystal boundary increases and the film surface energy increases (Henkel and Pense 2002). As a result, more ions and atoms will adsorb on the surface to reduce its energy. This is what is observed in our case, namely, the crystal size of films deposited on substrates annealed at 900 °C is smaller than the crystal size of films deposited on substrates annealed at 1100 °C, as shown in Fig. 5.50.

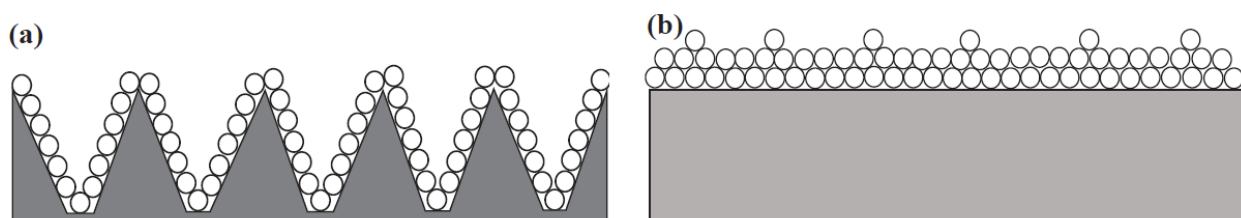


**Figure 5.58: Roughness effect on film thickness: (a) heat treated substrate and (b) non-heat treated substrate** (Chalermkiti et al., 2013).

The recorded Raman spectra of deposited films are composed of the typical features of NCD, as discussed in section 3.4.2, Chapter 3. Films exhibit  $sp^3$  in the range of 97.4% - 98.5%, as shown in Fig. 5.48. The nanocrystallinity percentage of films ranges between 91.5% and 96.1%, as shown in Fig. 5.49, and a crystal size in the range of 3.1 – 3.9, as shown in Fig. 5.50. Films deposited on substrates annealed at 1100 °C and 900 °C have similar  $sp^3$  and nanocrystallinity percentages, as shown in Fig. 5.48 and Fig. 5.49. The crystal size of films (3.9 - 4.3 non-annealed, 3.1 - 3.2 annealed at 900 °C, 3.6 - 3.9 annealed at 1100 °C) does not seem to be clearly affected by the heat treatment, as shown in Fig. 5.34 and Fig. 5.50. The morphology of the films as revealed by AFM (Fig. 5.54 and Fig. 5.55) and SEM (Fig. 5.56 and Fig. 5.57) analysis consists of clusters of crystals (grains) with submicronic size. With respect to the crystal size, AFM and SEM results are

consistent with Raman analysis. It is worth mentioning that characteristics of the films obtained in the third series, namely,  $sp^3$  and nanocrystallinity percentages, are similar in magnitude to those of films obtained in the second series, at 8 Hz and 14.5 kV.

The hardness of the films is within the range of 19.2 GPa – 20.5 GPa, as reported in Tables 5.7 and 5.8, which is consistent with the microhardness of NCD films reported in the open literature, see Table 2.1, Chapter 2.

## **Chapter 6: Conclusion and Future Work**

## 6.1 Conclusion

The present thesis work is a feasibility study towards the deposition of nanocrystalline diamond films via pulsed electron beam ablation. The main goal is to assess the potential of PEBA as an alternative thin film deposition technique for the preparation of nanocrystalline diamond material. To this end, different operation conditions, such as accelerating voltage, pulse rate deposition, substrate temperature and material have been investigated in three series. The most important findings obtained throughout this work are summarized hereafter.

I have attempted to identify the optimum process conditions that would likely result in producing diamond films based on two theoretical models and the carbon phase diagram. My calculations have shown that the substrate-target distance is a critical parameter, and diamond is likely to be produced under short distances. A value of 5 cm could be used under the limitations imposed by PEBA chamber geometry. The background gas pressure is equally important as it affects the energy of ions upon impact on the substrate. Lower values of the pressure are recommended and a value of ~5 mTorr has been chosen. Other process parameters, namely, the accelerating voltage was not critically important for diamond deposition. Voltage values of 13 kV, 14.5 kV and 16 kV, and frequencies of 5 Hz and 8 Hz have been used to assess their respective effect on film quality. Two and 5 Hz (for frequency) have been also attempted.

In the first series of experimental runs, NCD thin films have been prepared via the ablation of HOPG target on various substrates at 5 Hz and 14.5 kV and at two different substrate temperatures. NCD films deposited on corning and Si(111) are slightly thinner compared to the films deposited on Si(100), pyrex, sapphire, stainless steel, and cBN, which exhibit similar film thickness. This would indicate that substrate material does not seem to influence the thickness of overlaying films. Moreover, the substrate material does not substantially affect  $sp^3\%$ , nanocrystallinity percentage, and crystal size in the films. Raising the deposition temperature would result in lower  $sp^3\%$ , nanocrystallinity percentage, and crystal size in films relatively to films deposited at room temperature. The deposition temperature does not seem to have any effect on the magnitude of thickness of the resulting films. A larger number of pulses (5500) produces remarkably thicker films with larger crystals compared to films produced at a lower number of pulses (3500). However, all films deposited using 5500 pulses exhibit slightly higher  $sp^3$  and nanocrystallinity percentages relatively to films deposited using a lower number of pulses (3500).

In the second series of experimental runs, the films have been prepared at different values of the accelerating voltage and pulse repetition rate. At 8 Hz, NCD films deposited at 14.5 kV are thickest followed by films obtained at 16 kV. NCD films obtained at 13 kV are thinnest. However, at 5 Hz, the accelerating voltage does not have an influence on film thickness. At 8 Hz, the magnitudes of  $sp^3$  and nanocrystalline percentages in the films seem to be similar at 14.5 kV and 16 kV. However, the magnitudes of  $sp^3$  and nanocrystalline percentages in the films deposited at 14.5 kV and 16 kV are slightly higher relatively to films deposited at 13 kV. With respect to the crystal size, the latter is larger for the films obtained at 14.5 kV relatively to films produced at 13 kV and 16 kV. At 5 Hz, the magnitudes of  $sp^3$  and nanocrystalline percentages in films deposited at 14.5 kV are higher relatively to the films deposited at 13 kV and 16 kV. The crystal size seems to be similar for the films deposited at 14.5 kV and 16 kV, and smaller for films obtained at 13 kV. In terms of pulse repetition rate, the fraction of  $sp^3$  carbon bonded atoms in the films seems to be higher at the pulse repetition rate of 8 Hz relatively to 5 Hz. Moreover, nanocrystallinity percentage value is overall slightly larger at the higher repetition rate (8 Hz) compared to films deposited at 5 Hz. The crystal size in films deposited at 8 Hz is remarkably larger compared to films deposited at 5 Hz.

In the third series, annealing the substrates at 1100 °C would reduce film thickness compared to films on non-annealed substrates or on substrates annealed at 900 °C due to changes in roughness and energetics of the heat treated substrates. Apparently,  $sp^3$  and nanocrystallinity percentages in NCD films deposited on annealed substrates are similar in values compared to films deposited on non-annealed substrates, under same conditions, namely, 14.5 kV and 8 Hz. Films deposited on substrates annealed at 1100 °C and 900 °C have similar  $sp^3$  and nanocrystallinity percentages.

Hardness of all films have been measured using nanoindentation for various penetration depths corresponding to their film thickness. The hardness values have been calculated for NCD films after elimination of substrate effect. Hardness of the films produced in this work is within the range of 18.2 – 20.5 GPa, which is consistent with the microhardness data of NCD films reported in the open literature.

## 6.2 Future Work

Based on the finding of the present work, a few suggestions are warranted that can either help with the further fine tuning of process parameters or impart new properties in the deposited films.

- First, a Faraday probe, which is a plasma diagnostic tool, could be used to further tune the resulting PEBA plasma. A good estimate/measurement of electron temperature and plasma potential can be obtained in order to produce good quality NCD by imparting the optimum amount of energy per bombarding ion.
- Second, different carbon targets could be used in order to investigate the effect of target structure and density on the quality of resulting NCD films. Suggested targets are: pure isostatically pressed graphite (Mednikarov et al., 2005), pure graphite target (Pearce et al., 2004), vitreous carbon target (Kundu et al. 1996). The aforementioned targets are cheaper compared to HOPG. However, in terms of physical and chemical properties, HOPG seems to exhibit a better structure integrity with fewer defects and larger density.
- Third, different background gases, such as hydrogen and nitrogen, could be used instead of argon used in this work. Because graphite is thermodynamically more stable than diamond, the growth of metastable diamond may require the presence of atomic hydrogen, which has been thought to stabilize the diamond lattice and to remove graphitic nuclei when they do form because of the preferential etching of graphite over diamond (Gruen, 1999; Liu et al., 2004; Angus and Hayman, 1988). However, high hydrogen concentration may break up the C-C  $sp^3$  network, negatively affecting the tribological properties of the films (Donnet and Erdemir, 2007). Using  $N_2$  gas during the deposition of NCD would result in nitrogen-doped NCD, an n-type material. In this case, NCD would be suitable for the carbon-based electronics. It may also be used in future downscaled complementary metal-oxide semiconductor technology. Nitrogen incorporation leads to an increase of the amount of  $sp^2$ -bonded carbon in the intergrain phase, though (Williams et al., 2004; Zimmerman et al., 2005).

## References

Achatz, P., Garrido, J.A., Stutzmann, M., Williams, O.A., Gruen, D.M., Kromka, A. and Steinmüller, D. 2006, Optical properties of nanocrystalline diamond thin films, *J. Appl. Phys. Lett.* vol.88, pp.101908.

Aga, R.S., Cox, C., Ueda, A., Jackson, E., Collins, W.E., and Mu, R. 2006, Influence of background gas pressure charging potential and target distance on the spot size ablated by single pulsed electron beam, *J. Vacuum Science & Technology A*, vol. 24, no. 6, pp.L11-L14.

Aisenberg, S. & Chabot, R. 1973, "Physics of ion plating and ion beam deposition", *Journal of vacuum science technology*, vol. 10, no. 1, pp. 104-7.

Alexandrou, I.; Scheibe, H.-J.; Kiely, C.J.; Papworth, A.J.; Amaratunga, G.A.J.; Schultrich, B. 1999, Carbon films with an sp<sup>2</sup> network structure, *J. Phys. Rev. B*, vol.60, issue 15, pp.10903–10907.

Alskehli, O., and Henda, R. 2013, Nanocrystalline Diamond Films Prepared by Pulsed Electron Deposition on Different Substrates, accepted in Proc. 4th int. conf. nanotech., 12-14, pp. 6.

Anders, A. 2008, Cathodic arcs: from fractal spots to energetic condensation, Springer, New York.

Anderson et al. 2004, "Chapter 4: Host Reactions to Biomaterials and Their Evaluation" in Biomaterials Science: An Introduction to Materials in Medicine, eds. Ratner, B.D., Hoffman, A.S., and Schoen, F.J., Elsevier Academic Press, San Diego, California, pp. 293–353.

Angus, J.C., and Hayman, C.C. 1988, "Low pressure, metastable growth of diamond and 'diamondlike' phase" *J. Science*, vol. 241, pp.913-923.

Anisimov, S.I.; Luk'yanchuk, B.S.; and Luches, A. 1996, "An analytical model for three-dimensional laser plume expansion into vacuum in hydrodynamic regime", *J. Applied Surface Science*, vol.96-98, pp. 24-32.

Aoki, K.; Suzuki, K.; Ishii, K.; Takanashi, K.; Komukai, T.; Oura, K. and Hirao, T. 2005, Formation of Nanoscale Diamond Particles without Substrate Heating by Cathodic Arc Deposition, *Japanese Journal of Applied Physics*, Vol.44, No.23, pp. L746-L748.

Asmussen, J.; and Reinhard, D.K., *Diamond Films Handbook*, CRC Press, New York, 2002.

Bakowicz, K.; and Mitura, S. Bioactivity of Diamond Proc. IEEE-EMBS Spec. Top. Conf. Mol. Cell. Tiss. Eng. 2002 pp.79-80.

Bakowicz, K.; and Mitura, S., 2002, Biocompatibility of NCD, *J. Wide Bandgap Material*, vol.9, pp.261-272.

Balachandran, S. 2009, Nanocrystalline Diamond for RF MEMS Applications, Doctoral Thesis, University of South Florida.

Ballutaud, D.; Jomard, F.; Theys, B.; Kociniewski, T.; Rzepka, E.; Girard, H.; Saada, S.; 2008,  $sp^3/sp^2$  character of the carbon and hydrogen configuration in micro- and nanocrystalline diamond, *J. Diamond Related Material*, vol.17, issue 4-5, pp.451-456.

Barnard, A.S.; and Sternberg, M., 2005, Substitutional Nitrogen in Nanodiamond and Bucky-Diamond Particles, *J. Phys. Chem. B*, vol.109, pp.17107.

Berman, R. 1994 in "Properties and Growth of Diamond", by Davis, G., Short Run Press, England.

Bao, T. 2000, Characterization and Optimization of Microhardness of Diamondlike Carbon Films Deposited from RF Inductively Coupled Plasmas, Case Western Reserve University.

Bhattacharyya, S., 2004, Mechanism of high n-type conduction in nitrogen-doped nanocrystalline diamond, *J. Physical Review B*, vol. 70, pp.125412.

Balon, F.; Stolojan, V.; Silva, S.R.P.; Michalka, M. & Kromka, A. 2005, "Diamond-like carbon thin films for high-temperature applications prepared by filtered pulsed laser deposition", *J. Vacuum*, vol. 80, no. 1, pp. 163-167.

Booth, L.; Catledge, S.; Nolen, D.; Thompson, R.; and Vohra, Y. 2011, Synthesis and Characterization of Multilayered Diamond Coatings for Biomedical Implants, *J. Materials*, vol.4, pp.857-868.

Bowen, W.R.; and Hilal, N. 2009, Atomic Force Microscopy in Process Engineering: An Introduction to AFM for Improved Processes and Products, Elsevier Ltd., Oxford, UK.

Bozorg-Grayeli, E.; Sood, A.; Asheghi, M.; Gambin, V.; Sandhu, R.; Feygelson, T.; Pate, B.; Hobart, K.; and Goodson, K. 2013, Thermal conduction inhomogeneity of nanocrystalline diamond films by dual-side thermoreflectance, *J. Applied Physics Letter*, vol.102, pp.111907-1-14.

Bragg's Law and Diffraction: How waves reveal the atomic structure of crystals 2013, Suny Stony Brook [Mineral Physics Institute], [online]. Available: <http://www.eserc.stonybrook.edu/ProjectJava/Bragg/> [30 April 2013].

Brookes, C.A.; and Brookes, E.J., 1991, Diamond in perspective: a review of mechanical properties of natural diamond, *J. Diamond and Related Materials*, Vol. 1, Issue 1, pp. 13–17.

Brown, I. 1998, "Cathodic arc deposition of films", *Annual review of materials science*, vol. 28, pp. 243-269.

Bundy, F.P.; Hall, H.; Strong, H.; Jr. Wentorf, R. 1955, *J. Nat.*, vol.176, pp. 51–55.

Bundy, F.P., 1980, "The P, T Phase and Reaction Diagram for Elemental Carbon", *Journal of Geophysical Research*, vol. 85, No. B12, pp.6930-6936.

Casari, C.S.; Bassi, A.L.; Baserga, A.; Ravagnan, L.; Piseri, P.; Lenardi, C.; Tommasini, M.; Milani, A.; Fazzi, D.; Bottani, C.E.; Milani, P. 2008, Low-frequency modes in the Raman spectrum of sp-sp<sup>2</sup> nanostructured carbon, *J. Phys. Rev. B*, vol.77, pp.195444.

Catledge, S.A.; Borham, J.; Vohra, Y.K.; Lacefield, W.R.; Lemons, J.E. 2002, Nanoindentation hardness and adhesion investigations of vapor deposited nanostructured diamond films, *J. Applied Physics*, vol. 91, no.8, pp.5347-5352.

Cazes, J., and Ewing, G.W. 2005, *Ewing's Analytical Instrumentation Handbook*, CRC Press, New York.

Chalermkiti, T.; Panapoy, M.; Chaiyut, N.; and Ksapabutr, B. 2013, Fabrication of samarium doped ceria electrolyte on rough glass substrate with high electrical conductivity by electrostatic spray deposition for intermediate temperature solid oxide fuel cells, *J. Energy Procedia*, vol. 34, pp. 471–478.

Chang, Y.R.; Lee, H.Y.; Chen, K.; Chang, C.C.; Tsai, D.S.; Fu, C.C.; Lim, T.S.; Tzeng, Y.K.; Fang, C.Y.; Han, C.C.; Chang, H.C.; and Fann, W. 2008, Single defect centres in diamond: A review, *J. Nat. Nanotechnol.*, vol.3, pp.284.

Chen, Y.; Lee, D.; and Chiu, I. 2011, "Nanocrystalline Diamond Films: Applications and Advances in Nanomedicine" in *Biomaterials Applications for Nanomedicine*, ed. Pignatello, R., InTech, Chapters, New York, 2011.

Christen, H.M.; Lee, D.F.; List, F.A.; Cook, S.W.; Leonard, K.J.; Heatherly, L.; Martin, P.M.; Paranthaman, M.; Goyal, A.; and Rouleau, C.M., 2005, Pulsed electron deposition of fluorine-based precursors for YBa<sub>2</sub>Cu<sub>3</sub>O<sub>7-x</sub>-coated conductors, *J. Supercond. Sci. Technol.*, vol.18, pp.1168.

Christiansen, J.; and Schultheiss, C. 1979, Production of high current particle beams by low pressure spark discharges, *J. Z. Phys. A*, vol.290, pp.35–41.

Christiansen, S.; Albrecht, M.; Strunk, H.P.; Mtucke, F.; Stark, R.; Frank, K.; and Christiansen, J., 1996, "Hydrogen-free deposition of diamond-like coatings from a graphite source", *J. Diamond and Related Materials*, vol.5, pp.1433-1439.

Chu, P.K.; Li, L. 2006, Characterization of amorphous and nanocrystalline carbon films, *J. Materials Chemistry and Physics*, vol.96, pp.253–277.

Cote, M.; Grossman, J.C.; Cohen, M.L.; and Louie, S.G. 1998, Theoretical study of a three-dimensional all-sp<sup>2</sup> structure, *J. Physical Review B*, vol.58, no.2, pp.664-668.

Davis, J.R., 1992, *Asm Materials Engineering Dictionary*, Technology & Engineering, New York, USA.

Deryagin, B.; and Fedoseev, D. 1975, The Synthesis of Diamond at Low Pressure, *J. Sci. Am.*, vol.233, issue 5, pp. 102-109.

Diamond Crystallography 2013, Synthetic CVD Diamond [Homepage of elementsix], [online]. Available:<http://www.e6cvd.com/cvd/page.jsp?pageid=361> [22 April 2013].

Dischler, B.; Wild, C.; Muller-Sebert W.; Koidl, P. 1993, Hydrogen in polycrystalline diamond: An infrared analysis, *J. Physica B: Cond. Matter*, vol.185, pp.217.

Doggett, B.; and Lunny, J. 2011, Expansion dynamics of laser produced plasma, *J. Applied Physics*, vol.109, pp.093304.

Donnet, C.; and Erdemir, A., *Tribology of Diamond-like Carbon Films: Fundamentals And Applications*. Springer, New York, 2007.

Dow Corning Corporation 2012, Chemical Vapor Deposition [Homepage of Dow Corning], [online]. Available:[http://www.dowcorning.com/content/etronics/etronicschem/etronics\\_newcvd\\_tutorial3.asp?DCWS=Electronics&DCWSS=Chemical%20Vapor%20Deposition](http://www.dowcorning.com/content/etronics/etronicschem/etronics_newcvd_tutorial3.asp?DCWS=Electronics&DCWSS=Chemical%20Vapor%20Deposition) [23 April 2012].

Drabold, D.A.; Fedders, P.A.; Stumm, P. 1994, Theory of diamondlike amorphous carbon, *J. Phys. Rev. B*, vol.49, pp.16415.

Eaton, P.; and West, P. 2010, *Atomic Force Microscopy*, Oxford University Press Inc., New York, USA.

ElSay K. 2011, Nanodiamond as a drug delivery system: Applications and prospective, *J. of Applied Pharmaceutical Science* vol.1, issue 6, pp. 29-39.

Erdemir, A.; Fenske, G.R.; Krauss, A.R.; Gruen, D.M.; McCauley, T.; and Csencsits, R.T. 1999, Tribological properties of nanocrystalline diamond films, *J. Surface and Coatings Technology*, vol. 120–121, 1999, pp.565–572.

Erdemir, A.; & Donnet, C. 2006, "Tribology of diamond-like carbon films: Recent progress and future prospects", *Journal of physics. D, Applied physics*, vol. 39, no. 18, pp. R311-R327.

Eversole, W.; and Angus, Synthesis of Diamond, U.S. Patent, 3,030,187, 1962a.

Fernsler, R.F.; Hubbard, R.F.; Lampe, M. 1994, Pinched Propagation of High-Power, Pulsed Electron Beams for Welding and Materials Processing Applications, Naval Research Lab Washington DC, pp.1-59.

Ferrari, A.C., and Robertson, J. 2001, Is there a "Nanocrystalline Diamond" Raman Peak in Nanocrystalline Diamond, *J. Nanostructured Carbon for Advanced Applications*, vol. 24, pp 177-184.

Ferrari, A.C.; and Robertson, J. 2001, Origin of the 1150  $\text{cm}^{-1}$  Raman mode in nanocrystalline diamond, *J. Physical Review B*, vol 63, pp. 121405.

Ferrari, A.C.; and Robertson, J. 2004, Raman spectroscopy of amorphous, nanostructured, diamond-like carbon, and nanodiamond, *J. The Royal Society*, vol.362, pp. 2477-2512.

Ferro, S., 2001, Electrochemical Reactions at Conductive Diamond Electrodes, PhD Thesis, University of Ferrar.

Fischer-Cripps, A.C. 2000, A review of analysis methods for sub-micron indentation testing, *J. Vacuum*, vol.58, pp.569-585.

Fischer-Cripps, A.C., 2004, Nanoindentation, Springer, New York, USA, pp.21-33.

Fotsa-Ngaffo, F. 2008, Reactive pulsed laser ablation deposition of indium tin oxide, titanium dioxide thin films and gold nanoparticles for dye sensitised solar cells applications, PhD Thesis, University of the Witwatersrand.

Fox, M. A.; and Whitesell, J.K. 2004, Organic Chemistry, Jones & Bartlett Publishers, MA, USA.

Francis, A.J. and Salvador, P.A. 2012, Effect of surface treatment on chiral and achiral SrTiO<sub>3</sub> surface morphology and metal thin film growth, *J. Surfaces, Interfaces, and the Science of Ceramic Joining*, vol. 158, pp.1-11.

Frontini, P.; and Fasce, L.A. 2011, Instrumented Indentation to Characterize Mechanical Behavior of Materials, Asociacion Argentina de Ensayos.

Fyta, M.G.; Hadjisavvas, G.C.; Kelires, P.C. 2007, Probing the  $sp^2$  dependence of elastic moduli in ultrahard diamond films, *J. Diamond Relat. Mater.*, vol.16, pp.1643.

Gajewski, W.; Achatz, P.; Williams, O.A.; Haenen, K.; Bustarret, E.; Stutzmann, M.; and Garrido, J.A. 2009, Electronic and optical properties of boron-doped nanocrystalline diamond films, *J. Phys. Rev., B* 79, pp.045206.

Gardos, M.N.; and Ravi, K.V. 1994, Surface-chemistry-controlled friction and wear behavior of Si(100) vs. textured polycrystalline diamond film tribocontacts, *J. Diamond Films Technology*, vol.4, pp.139.

Gardos, M.N., 1996, Surface chemistry-controlled tribological behavior of silicon and diamond, *J. Tribology Letters*, Vol.2, pp.173-187.

Gilgenbach, R.; Kovaleski, S.D.; Lash, J.S.; Ang, L.K.; and Lau, Y.T. 1999, Science and Applications of Energy Beam Ablation, *J. IEEE Trans. Plasma Sci.*, vol.27, pp.150.

Gopalakrishnan, B.; and Subramanyam, S.V. 2002, "Many phases of Carbon", *Journal of Resonance*, vol. 7, no. 12, pp. 10-19.

Graphite 2013, Wikimedia Commons [Homepage of Wikimedia], [online]. <http://commons.wikimedia.org/wiki/File:Graphite-tn19a.jpg> [22 April 2013].

Greentree, A.D.; Aharonovich, I.; Castelletto, S.; Doherty, M.W.; McGuinness, L.P.; and Simpson, D.A., 2010, 21st-Century Applications of Nanodiamonds, *J. Opt. Photonics News*, vol.21, pp.20.

Gruen, D.M., 1999, Nanocrystalline Diamond Films, *J. Annual Review of Materials Science*, vol.29, pp. 211-259.

Haenni, W; Rychen, P.; Fryda, M.; and Comninellis, C. 2004, "Chapter 5 Industrial Applications of Diamond Electrodes", in *Thin-Film Diamond II: part of the Semiconductors and Semimetals*

Series, eds. Nebel, C.; and Ristein, J., Elsevier, CA, USA.

Hall, H.T.; Bundy, F.P.; Strong, H.M.; Wentorf, R.H. 1955, *J. Nature*, vol.176, pp.51.

Hall, H.T. 1961, The Synthesis of Diamond, *J. Chemical Education*, vol.38, pp. 484.

Hanson, J., 1977, Investigation of a High Voltage Hollow Cathode Electron Beam Source, Riso National Laboratory, Riso Report No. 359, Denmark.

Harshavardhan, K.S.; & Strikovski, M. 2005, "Chapter 8: Pulsed Electron-Beam Deposition of High Temperature Superconducting Films for Coated Conductor Applications" in *Second Generation HTS Conductors*, ed. A. Goyal, Springer, Berlin, pp. 109-133.

Hershey, J.W. 1929, *Trans. Kansas Acad. Sci.*, vol. 32, pp. 52–54.

Henda, R.; and Alshekhli, O. 2012, Pulsed Electron Beam Deposition of Nanocrystalline Diamond, *MRS Online Proceedings Library, Mater. Res. Soc.*, Boston, USA, 1505, Fall Meeting Nov. 25-30, pp. 6-10.

Henda, R.; Wilson, G.; Gray-Munro, J.; Alshekhli, O.; and McDonald, A.M. 2012, Preparation of polytetrafluoroethylene by pulsed electron ablation: Deposition and wettability aspects, *J. Thin Solid Films*, vol.520, pp.1885-1889.

Henkel, D.P.; and Pense, A.W. 2002, *Structure and Properties of Engineering Materials*, McGrawHill, Boston, pp.98-105.

Hind, A.R.; and Chomette, L., 2011, The determination of thin film thickness using reflectance spectroscopy, *J. Agilent Technology*, SI-A-1205.

Hobel, M.; Greek, J.; Linker, G.; and Schultheiss, C. 1990, "Deposition of superconducting YBaCuO thin films by pseudospark ablation", *J. Applied Physics Letters*, vol. 56, no. 10, pp. 973-975.

Holt, K.B., 2007, Diamond at the nanoscale: applications of diamond nanoparticles from cellular biomarkers to quantum computing, *J. Philos. Trans. R. Soc., A*, vol.365, pp.2845.

Hongyan, P.; Jiajing, S.; and Guilong, Y. 2000, Study of Nanocrystalline Diamond Film Deposited Rapidly by 500 W Excimer Laser, *Chinese Journal of Lasers*, vol. B9, no. 3, pp.201-205.

Jabeen, A. H. 2009, Deformation Behaviour of Diamond-like Carbon Coatings on Silicon Substrates, University of New South Wales.

Jackson, B.D. 1997, Pulsed-Laser Deposition of Silicon Dioxide Thin-Films Using the Molecular Fluorine Laser, University of Toronto.

Jackson, M.; and Ahmed, W. 2007, Surface Engineered Surgical Tools and Medical Devices, Springer, New York, pp.242.

Jelezko, F.; and Wrachtrup, J., 2006, Single defect centres in diamond: A review, *J. Phys. Status Solid A*, vol.203, pp.3207.

Kitabatake, M.; and Wasa, K. 1985, Growth of diamond at room temperature by an ion-beam sputter deposition under hydrogen-ion bombardment, *J. Appl. Phys.*, vol.58, pp.1693.

Klauser, F.; Steinmuller-Nethl, D.; Kaindl, R., Bertel; E., and Memmel, N., 2010, Raman Studies of Nano- and Ultra-nanocrystalline Diamond Films Grown by Hot-Filament CVD, *J. Chemical Vaporization Deposition*, vol.16, issue 4-6, pp.127–135.

Kovalenko, I.; Bucknall, D.G.; and Yushin, G., 2010, Detonation Nanodiamond and Onion-Like Carbon-Embedded Polyaniline for Supercapacitors, *J. Adv. Funct. Mater.*, vol.20, pp.3979.

Krueger, A., 2008, The structure and reactivity of nanoscale diamond, *J. Materials Chemistry*, vol.18, pp.1485-1492.

Krueger, A., 2011, Beyond the shine: recent progress in applications of nanodiamond, *J. Mater. Chem.*, vol.21, pp.12571-12578.

Kumar, N.; Dash, S.; Tyagi, A.; and Raj, B. 2010, Dynamics of plasma expansion in the pulsed laser material interaction, *J. Indian Academy of Sciences*, Vol. 35, Part 4, pp. 493–511.

Kumar, N.; Panda, K.; Dash, S.; Popov, C.; Reithmaier, J.; Panigrahi, B.; Tyagi, A.; and Raj, B. 2012, Tribological properties of nanocrystalline diamond films deposited by hot filament chemical vapor deposition, *J. AIP Advances*, vol.2, no. 3, pp.032164-1-14.

Kundu, S.N.; Basu, M.; Maity, A.B.; Chaudhuri, S.; Pal, A.K. 1997, Nanocrystalline diamond films deposited by high pressure sputtering of vitreous carbon, *J. Materials Letters*, vol.31, pp.303-309.

Lacerda, R.G.; and Marques, F.C. 1998, Hard hydrogenated carbon films with low stress, *J. Appl. Phys. Lett.*, vol.73, issue 5, pp.617–619.

Lam, R.; Chen, M.; Pierstorff, E.; Huang, H.; Osawa, E.; and Ho, D., 2008, Nanodiamond-Embedded Microfilm Devices for Localized Chemotherapeutic Elution, *J. ACS Nano*, vol.2, pp.2095.

Lee, S.T.; Lau, W.M.; Huang, L.J.; Ren, Z.; and Qin, F. 1995, Diamond growth by carbon ion implantation of diamond, *J. Diamond and Related Materials*, vol.4, pp.1353-1359.

Lewis, I. R.; and Edwards, H G. M. 2001, Handbook of Raman Spectroscopy: From the Research Laboratory to the Process Line, CRC Press, New York.

Liander, H. 1980, *Ind. Diamond Rev.*, vol.40, pp. 412–415.

Liander, H. 1955, *ASEA Journal*, vol.28, pp.97.

Lieberman, M.A.; and Lichtenberg, A.J., Principles of Plasma Discharges and Materials Processing. Wiley, NewYork, 1994.

Lifshitz, Y.; Lempert, G.D.; Grossman, E.; Avigal, I.; Uzan-Saguy, C.; Kalish, R.; Kulik, J.; Marton, D.; & Rabalais, J.W. 1995, "Growth mechanisms of DLC films from C<sup>+</sup> ions: experimental studies", *J. Diamond and Related Materials*, vol. 4, no. 4, pp. 318-323.

Lifshitz, Y. 1999, "Diamond-like carbon - present status", *Diamond and related materials*, vol. 8, no. 8, pp. 1659-1676.

Li, A.J.; Zhu, Y.; Li, W.; Zhang, X.; Peng, Y.; and Huang, Q., 2010, Nanodiamonds as intracellular transporters of chemotherapeutic drug, *J. Biomaterials*, vol.31, pp.8410.

Liu, A.Y.; and Cohen, M.L. 1991, Structural properties of a three-dimensional all-sp<sup>2</sup> phase of carbon, *J. Phys. Rev. B*, vol. 43, pp.6742–6745.

Liu, Y.; Liu, C.; Chen, Y.; Tzeng, Y.; Tso, P.; and Lin, I. 2004, "Effects of hydrogen additive on microwave plasma CVD of nanocrystalline diamond in mixtures of argon and methane", *J. Diamond and Related Materials*, vol.13, pp.671–678.

Liu, K.K.; Zheng, W.W.; Wang, C.C.; Chiu, Y.C.; Cheng, C.L.; Lo, Y.S.; Chen, C.; and Chao, J.I. 2010, Covalent linkage of nanodiamond-paclitaxel for drug delivery and cancer therapy, *J. Nanotechnology*, vol.21, pp.315106.

Lopez-Rios, T.; Sandre, E.; Leclerq, S.; & Sauvain, E. 1996, Polyacetylene in Diamond Films Evidenced by Surface Enhanced Raman Scattering, *J. Phys. Rev. Lett.*, vol.76, pp.4935.

Lyman , C. 1990, Scanning Electron Microscopy, X-Ray Microanalysis, and Analytical Electron Microscopy: A Laboratory Workbook, Sringer, Berlin, pp. 43, 12.

Mantell, C.L., Carbon and graphite handbook, Interscience Publishers, New York, 1968.

Matacotta, F.C., and Ottaviani, G. 1995, Science and technology of thin films, World Scientific, NewYork.

Matzinger, K. 2006, Evolution of Metal Catalyst During CVD Synthesis of Carbon Nanotubes, PhD Thesis, Universität Freiburg.

May, P.W.; Smith, J.A.; and Mankelevich, Y.A. 2006, Deposition of NCD films using hot filament CVD and Ar/CH<sub>4</sub>/H<sub>2</sub> gas mixtures, *J. Diamond & Related Materials*, vol.15, pp.345 – 352.

Mednikarov, B.; Spasov, G.; Babeva, Tz.; Pirov, J.; Sahatchieva, M., Popov, C.; Kulisch, W. 2005, Optical Properties of Diamond-Like Carbon and Nanocrystalline Diamond Films, *J. Optoelectronics and Advanced Materials* vol. 7, no. 3, pp. 1407-1413.

McKenzie, D.R.; Muller, D.; Pailthorpe, B.A.; Wang, Z.H.; Kravtchinskaia, E.; Segal, D.; Lukins, P.B.; Swift, P.D.; Martin, P.J.; Amaratunga, G.; Gaskell, P.H. & Saeed, A. 1991, "Properties of tetrahedral amorphous carbon prepared by vacuum arc deposition", *J. Diamond and related materials*, vol. 1, no. 1, pp. 51-59.

Michaelson, Sh.; Ternyak, O.; Hoffman, A. and Lifshitz, Y. 2007, Correlation between diamond grain size and hydrogen retention in diamond films studied by scanning electron microscopy and secondary ion mass spectroscopy, *J. Appl. Phys. Lett.*, vol.90, pp.031914.

Miller, F.P.; Vandome, A.F.; and McBrewster, J., Carbon: Allotropes of Carbon. Alphascript Publishing, Germany, 2009.

Moore, Z., 2008, Application of X-ray Diffraction Methods and Molecular Mechanics Simulations to Structure Determination and Cotton Fiber Analysis, PhD Thesis, University of New Orleans.

Muller, G.; Konijnenberg, M.; Kraft, G. & Schultheiss, C. 1995, "Thin fiim deposition by means of pulsed electron beam ablation" in Science and Technology of Thin Films, eds. F.C. Maticotta & G. and Ottaviani, World Scientific, Singapore, pp. 89.

Myers, M.C.; Fernsler, R.F.; Meger, R.A.; Antoniadis, J.A.; Murphy, D.P.; and Hubbard, R.F., 1996, "Emittance tailoring of electron beams for propagation in dense gas". *J. Appl. Phys.*, vol.80, pp.4258.

Narayan, R.; Wei, W.; Jin, C.; Andara, M.; Agarwal, A.; Gerhardt, R.; Shih, C.; Shih, C.; Lin, S.; Su, Y.; Ramamurti, R.; and Singh, R. 2006, Microstructural and biological properties of nanocrystalline diamond coatings, *J. Diamond & Related Materials*, vol.15, pp.1935–1940.

Navalon, S.; de Miguel, M.; Martin, R.; Alvaro, M. and Garcia, H., 2011, Enhancement of the Catalytic Activity of Supported Gold Nanoparticles for the Fenton Reaction by Light, *J. Am. Chem. Soc.*, vol.133, pp.2218.

Nazare, M.H.; Neves, A.J.; 2001, Properties, Growth and Applications of Diamond, Institution of Engineering and Technology, Bristol, UK.

Nazarov, M.; and Noh, D.Y. 2011, New Generation of Europium and Terbium Activated Phosphors: From Syntheses to Applications, CRC Press, London, UK, pp.76-80.

Nemanich, R. J.; Glass, J. T.; Lucovsky, G. & Shroder, R. E. 1988, Raman Scattering Characterization of Carbon Bonding in Diamond and Diamondlike Thin Film, *J. Vac. Sci. Technol.*, vol.A6, pp.1783.

Neocera Inc. 2011, PED Technology [Homepage of Neocera Inc.], [Online]. Available: [http://www.neocera.com/Thin\\_Film/ped\\_at\\_neocera.html](http://www.neocera.com/Thin_Film/ped_at_neocera.html) [2011, 2011, 06/07].

Nesladek, M.; Stals, L.M.; Stesmans, A.; Iakoubovskij, K.; Adriaenssens, G.J.; Rosa, J.; and Vanecek, M., 1998, *J. Appl. Phys. Lett.*, vol.72, pp.3306.

Nistor, M.; Gherendi, F.; and Mandache, N.B. 2011, Fast Imaging of Ablation Plasma Produced by a Pulsed Electron Beam, *J. Transactions on Plasma Science*, vol.39, no.11, pp.2800-2801.

Ohring, M., 2002, The materials science of thin films: deposition and structure, 2<sup>nd</sup> ed. Academic Press, New York.

Okada, K. 2007, Plasma-enhanced chemical vapor deposition of nanocrystalline diamond, *J. Sci. Technol. Adv. Mater.*, vol.8, pp.624.

Opel M.; Venturini F., 2002, Raman Scattering in Solids, *J. European Pharmaceutical Review*, vol. 5, pp. 76-82.

Ou, Y.; Guo, J.; and Yan, X. 2003, Growth of Nanocrystalline Diamond Films by Pulsed Laser Deposition in Oxygen Atmosphere, *Natural Science Journal of Xiangtan University*, vol.25, no.2, pp.30-33.

Ozur, G.; Popov, S.; Fedushchak, V. & Saushkin, A. 2006, "Generation of high-intensity pulsed low-energy electron beams in a channel spark system", *Technical Physics Letters*, vol. 32, no. 11, pp. 928-931.

Panwar, O.S.; Tripathi, I.R.; Srivastava, A.K.; Kumar, M.; Kumar, S.; 2012, Effect of substrate bias in hydrogenated amorphous carbon films having embedded nanocrystallites deposited by cathodic jet carbon arc technique, *J. Diamond and Related Materials*, Vol.25, pp.63–72.

Park, J.; Kang, D.; and Yoon, K. 1999, Effects of Substrate Pre-Annealing on the Preferred Orientation of Lead Magnesium Niobium Titanate Thin Films by Chemical Solution Deposition, *J. Ferroelectrics*, Vol. 225, pp. 253-260.

Pattini, F. 1999, Growth of oxide thin films for energy devices by Pulsed Electron Deposition, Università degli Studi di Parma.

Pearce, S.R.J.; Henley, S.J.; Claeysens, F.; May, P.W.; Hallam, K.R.; Smith, J.A.; Rosser, K.N. 2004, Production of nanocrystalline diamond by laser ablation at the solid-liquid interface, *J. Diamond and Related Materials*, vol.13, pp.661–665.

Peiponen, K.; Myllyla, R.; and Priezhev, A.V., 2009, *Optical Measurement Techniques: Innovations for Industry and the Life Sciences*, Springer, Berlin.

Penney, C.M.; Morey, W.W.; Peters, R.L.; Silverstein, S.D.; Lapp, M.; and White, D.R. 1973, *Study of Resonance Light Scattering for Remote Optical Probing*, NASA Langley Research Center, Virginia.

Philip, J.; Hess, P.; Feygelson, T.; Butler, J.E.; Chattopadhyay, S.; Chen, K.H.; and Chen, L.C. 2003, Elastic, mechanical, and thermal properties of nanocrystalline diamond films, *J. Applied Physics*, vol.93, no.4, pp.2164-2171.

Pierson, H., *Handbook of Carbon, Graphite, Diamond and Fullerenes Properties, Processing and Applications*, Noyes Publications, New Mexico, 1993.

Piscanec, S.; Mauri, F.; Ferrari, A.C.; Lazzeri, M.; Robertson J. 2005, Ab initio resonant Raman spectra of diamond-like carbons, *J. Diamond and Related Materials*, vol.14, pp.1078-1083.

Pochon, S.; and Pearson, D. 2009, *Ion Beam Deposition*, Oxford Instruments Plasma Technology, UK.

Popov, C.; Bliznakov, S.; and Kulisch, W., 2007, Influence of the substrate nature on the properties of nanocrystalline diamond films, *J. Diamond Related Material*, vol.16, issue 4-7, pp.740–743.

Prawer, S.; Nugent, K.W.; Jamieson, D.N.; Orwa, J.O.; Bursill, L.A.; and Peng, J.L. 2000. The Raman spectrum of nanocrystalline diamond, *J. Chem. Phys. Lett.*, vol.332, pp.93.

Scanning Electron Microscope 2012, Radiological and Environmental Management [Homepage of Purdue University], [Online]. Available: <http://www.purdue.edu/rem/rs/sem.htm> [2012, 2012, 08/07].

Rakha, S.A.; Guojun, Y.; and Jianqing, C. 2010, Correlation between diamond grain size and hydrogen incorporation in nanocrystalline diamond thin films, *J. Experimental Nanoscience*, vol. 7, no. 4, pp. 378–389.

Ramamurti, R., 2006, Synthesis of Diamond Thin Films for Application in High Temperature Electronics, Doctoral Thesis, University of Cincinnati.

Ravi, S.; Silva, P.; Xu, S.; Tay, B.X.; Tan, H.S.; and Milne, W.I. 1996, Nanocrystallites in tetrahedral amorphous carbon films, *J. Appl. Phys. Lett.*, vol.69, pp.491.

Redel, T.; Eberlein, J.; Tkotz, R.; Hartmann, W.; Stetter, M.; Stark, R.; Frank, K.; and Christiansen, J., 1992, Schilieren diagnostics of pulsed electron beam ablation of polymethyl-methacrylate, *J. Appl. Phys. A*, vol.54, pp.520–522.

Rittner, D.; and Bailey, R.A. 2005, Encyclopedia Of Chemistry, Facts On File Inc., NY, USA.

Robertson, J. 1986, Amorphous carbon, *J. Adv. Phys.*, vol.35, pp. 317.

Robertson, J., and O'Reilly, E.P. 1987, Electronic and atomic structure of amorphous carbon, *J. Physical Review B*, vol.35, No. 6, pp.2946-2957.

Robertson, J. 2002, “Diamond-like amorphous carbon”, *J. Materials Science and Engineering: R: Reports*, vol. 37, no. 4-6, pp. 129-281.

Robertson, J. 2008, “Comparison of diamond-like carbon to diamond for applications”, *J. Physical Status solid, A, Applications and Materials Science*, vol. 205, no. 9, pp. 2233-2244.

Salis, S.R.; Gardiner, D.J.; Bowden, M.; Savage, J.; Rodway, D. 1996, Monitoring the quality of diamond films using Raman spectra excited at 514.5 nm and 633 nm. *J. Diam Relat Mater.*, vol.5, pp.589.

Saravanan, R.; and Rani, M.P. 2012, Metal and Alloy Bonding: An Experimental Analysis ; Charge Density in Metals and Alloys, Springer, London, UK, pp. 31-62.

Semiconsoft, Inc. (2012) TFCCompanion: Thin films analysis software, USER GUIDE, Version 4.0. Southborough, Massachusetts, USA.

SERS Diagnostic Biosensor 2012, Texas A&M University [Homepage of Optical Bio-Sensing Laboratory], [online]. Available: [http://biomed.tamu.edu/obs/BSL/Research%20Projects/SERS\\_biosensor.htm](http://biomed.tamu.edu/obs/BSL/Research%20Projects/SERS_biosensor.htm) [25 July 2012].

Sharda, T.; Umeno, M.; Soga, T.; and Jimbo, T. 2000, Growth of nanocrystalline diamond films by biased enhanced microwave plasma chemical vapor deposition: A different regime of growth, *J. Applied Physics Letters*, vol.77, no.26, pp.4304-4306.

Sharda, T.; Rahaman, M.M.; Nukaya, Y.; Soga, T.; Jimbo, T.; and Umeno, M. 2001, Structural and optical properties of diamond and nano-diamond films grown by microwave plasma chemical vapor deposition, *J. Diamond Relat. Mater.*, vol.10, pp.561.

Sharda, T.; Soga, T.; and Jimbo, T. 2003, Optical properties of nanocrystalline diamond films by prism coupling technique, *J. Applied Physics*, vol.93, no.1, pp.101-105.

Shroder, R. E.; Nemanich, R. J.; & Glass, J. T. 1990, Analysis of the composite structures in diamond thin films by Raman spectroscopy, *J. Phys. Rev. vol. B41*, pp.3738.

Sibiya, P.S., 2007, Nanostructured Diamond-Like Carbon by Dual Pulsed Laser Ablation-Pulsed Gas Feeding, Master Thesis, University of Zululand.

Singha, A.; Ghosh, A.; Ray, N.R.; Roy, A. 2006, Quantitative Analysis of Hydrogenated DLC Films by Visible Raman Spectroscopy, *J. Appl. Phys.*, Vol.100, pp.044910.

Spitsyn, B.V.; Denisov, S.A.; Skorik, N.A.; Chopurova, A.G.; Parkaeva, S.A.; Belyakova, L.D.; and Larionov, O.G., 2010, The physical–chemical study of detonation nanodiamond application in adsorption and chromatography, *J. Diamond Relat. Mater.*, vol.19, pp.123.

S-RS Raman Spectrometer 2012, [Homepage of Standa], [online]. Available: [http://www.standa.lt/products/catalog/spectroscopic\\_instruments?item=267&prod=raman\\_spectrometer](http://www.standa.lt/products/catalog/spectroscopic_instruments?item=267&prod=raman_spectrometer) [25 July 2012]

Strikovski, M.; and Miller, J.H., 1998, Pulsed laser deposition of oxides: Why the optimum rate is about 1 Å per pulse, *J. Applied Physics Letter*, 73, pp.1733-1735.

Strikovski, M.; and Harshavardhan, K.S., 2003, Parameters that control pulsed electron beam ablation of materials and film deposition processes, *J. Appl. Phys. Lett.*, vol.82, pp.853.

Strikovski, M.; Kim, J.; & Kolagani, S. 2010, "Plasma Energetics in Pulsed Laser and Pulsed Electron Deposition" in Springer Handbook of Crystal Growth, eds. G. Dhanaraj, K. Byrappa, V. Prasad & M. and Dudley, Springer-Verlag, Berlin Heidelberg, pp. 1193-1211.

Sun, X.S.; Wang, N.; Zhang, W.J.; Woo, H.K.; Han, X.D.; Bello, I.; Lee, C.S.; and Lee, S.T. 1999, Synthesis of nanocrystalline diamond by the direct ion beam deposition method, *J. Materials Research*, vol.14, no.8, pp. 3204-3207.

Tang, Y. 2010, Plasma and Ion Beam Enhanced Chemical Vapour Deposition of Diamond and Diamond-Like Carbon, University of Saskatchewan.

Toftmann, B.; Schou, J.; and Lunney, J.G., 2003, Dynamics of the plume produced by nanosecond ultraviolet laser ablation of metals, *J. Phys. Rev. B*, vol.67, pp.104101.

Tse, J.S.; Klug, D.D.; Gao, F. 2006, Hardness of nanocrystalline diamonds, *J. Physical Review B*, vol.73, pp.140102.

Turova, O.V.; Starodubtseva, E.V.; Vinogradov, M.G.; Sokolov, V.I.; Abramova, N.V.; Ya.Vul', A.; and Alexenskiy, A.E. 2011, Palladium supported on detonation nanodiamond as a highly effective catalyst of the C=C and C≡C bond hydrogenation, *J. Catal. Commun.*, vol.12, pp.577.

Venkatesan, T.; Harshavardhan, K.S.; Strikovski, M.; and Kim, J. 2005, "Recent advances in the deposition of multi-component oxide films by pulsed energy deposition" in *Thin Films and Heterostructures for Oxide Electronics*, eds. Ogale, S.B., Springer, Berlin Heidelberg, pp.385-413.

Voevodin, A.A.; & Donley, M.S. 1996, "Preparation of amorphous diamond-like carbon by pulsed laser deposition: a critical review", *J. Surface and Coatings Technology*, vol. 82, no. 3, pp. 199-213.

Wada, N.; Gaczi, P.J.; & Solin, A. 1980 Diamond-like 3-fold coordinated amorphous carbon, *J. Non-Cryst. Solids*, vol. 543, pp. 35–36.

Wadhwa, A. S.; and Dhaliwal, E. H. S., 2008, *A Textbook of Engineering Material and Metallurgy*, University Science Press, New Delhi, India, pp.152-165.

Wang, Q.; Allred, D.D.; González-Hernández, J. 1993, Low-frequency feature in the first-order Raman spectrum of amorphous carbon, *J. Phys. Rev. B*, vol.47, pp.6119.

Wang, L.; Huang, J.; Tang, K. and Xia, Y. 2010, "Nano-crystalline Diamond Films for X-ray Lithography Mask" in *Lithography*, eds. M. Wang, InTech, China, pp. 227-240.

Wang, L.F.; Tan, X.L.; Chen, P.F.; Zhi, B.W.; Chen, B.B.; Huang, Z.; Gao, G.Y.; and Wua, W.B. 2013, "Annealing assisted substrate coherency and high-temperature antiferromagnetic insulating transition in epitaxial  $\text{La}_{0.67}\text{Ca}_{0.33}\text{MnO}_3/\text{NdGaO}_3(001)$  films", *J. AIP Advances* vol.3, pp.052106-052121.

Wei, Q.; & Narayan, J. 2000, "Superhard diamondlike carbon: preparation, theory, and properties", *International materials reviews*, vol. 45, no. 4, pp. 133-64.

Williams, O.A.; Curat, S.; Gerbi, J.E.; Gruen, D.M.; and Jackman, R.B. 2004, "n-type conductivity in ultrananocrystalline diamond films", *J. Appl. Phys. Lett.* vol. 85, pp.1680-1692.

Williams, O.A.; Nesladek, M.; Daenen, M.; Michaelson, S.; Hoffman, A.; Osawa, E.; Haenen, K.; and Jackman, R.B., 2008, Growth, electronic properties and applications of nanodiamond, *J. Diamond Relat. Mater.*, vol.17, pp.1080.

Williams, O.A.; Nesladek, M.; Mares, J.J.; and Hubik, P. 2008, "Growth and Properties of Nanocrystalline Diamond Films" in *Physics and Applications of CVD Diamond*, eds. Koizumi, S., Nebel, C., Nesladek, M., Technology & Engineering, Weinheim, Germany.

Williams, O.A., 2011, Nanocrystalline diamond, *J. Diamond and Materials*, vol. 20, pp. 621-640.

Winfrey, A.L., 2007, Nanocrystalline Diamond Deposition for Friction Applications, Master Thesis, North Carolina State University.

Wiora, M.; Sadrifar, N.; Brühne, K.; Gluche, P.; Fecht, H. 2011, Correlation of Microstructure and Tribological Properties of Dry Sliding Nanocrystalline Diamond Coatings, *Proceedings of 3rd European Conference on Tribology*, vol. 1 , pp. 293-298.

Xie, W.G.; Chen, J.; Ming, W.W.; Chen, J.; Zhou, J.; Deng, S.Z.; and Xu, N.S. 2008, Preparation and field emission property of nanodiamond-cluster-embedded diamondlike carbon film, *J. Vac. Sci. Technol. B*, vol.26, pp.1321.

Xu, Z. 2004, Mechanical Characterisation of Coatings and Composites-Depth-Sensing Indentation and Finite Element Modelling, PhD Thesis, Royal Institute of Technology, Sweden.

Yang, W.; Lu, F.; Cao, Z., 2002, Growth of nanocrystalline diamond protective coatings on quartz glass, *J. Applied Physics*, vol.91, issue 12, pp.10068-10073.

Yoshitake, T.; Hara, T.; Fukugawa, T.; Zhu, L.Y.; Itakura, M.; Kuwano, N.; Tomokiyo, Y.; and Nagayama, K. 2004, Low-Temperature Growth of Nanocrystalline Diamond by Reactive Pulsed Laser Deposition under a Hydrogen Atmosphere, *Japanese Journal of Applied Physics*, vol. 43, no. 2B, pp. 1240- 1242.

Zapol, P.; Sternberg, M.; Curtiss, L.A.; Frauenheim, T.; Gruen, D.M. 2001, Tight-binding molecular-dynamics simulation of impurities in ultrananocrystalline diamond grain boundaries, *J. Phys. Rev. B*, vol.65, pp.045403.

Zazula, J M 1997, On Graphite Transformations at High Temperature and Pressure Induced By Absorption of the LHC Beam, *J. CERN Accelerating science*, vol. 78, pp. 1-15.

Zhang, J.; Su, D.S.; Blume, R.; Schloegl, R.; Wang, R.; Yang, X.; and Gajovic, A. 2010, Surface Chemistry and Catalytic Reactivity of a Nanodiamond in the Steam-Free Dehydrogenation of Ethylbenzene, *J. Angew. Chem., Int. Ed.*, vol.49, pp.8640.

Zhao, Y.Q.; Lau, K.T.; Kim, J.K.; Xu, C.L.; Zhao, D.D.; and Li, H.L., 2010, Nanodiamond/poly (lactic acid) nanocomposites: Effect of nanodiamond on structure and properties of poly (lactic acid), *J. Composites, Part B*, vol.41, pp.646.

Zimmerman, T.; Kubovich, M.; Denisenko, A.; Janioschovsky, K.; Williams, O.A.; Gruen, D.M.; and Kohn, E. 2005, "Ultra-nano-crystalline/single crystal diamond heterostructure diode", *J. Diamond Relat. Mater.*, vol.14, pp.416-426.